A compact spatial map in V2 visual cortex

Xiaoyang Long[1*], Bin Deng[1*], Jing Cai[1], Zhe Sage Chen[2] & Sheng-Jia Zhang[1#]

1. Department of Neurosurgery, Xinqiao Hospital, Army Medical University, Chongqing 400037, China

2. Department of Psychiatry, Department of Neuroscience & Physiology, Neuroscience Institute, New York University School of Medicine, New York, NY 10016, USA

*These authors contributed equally to this work.

[#]To whom correspondence should be addressed.

Correspondence and requests for materials should be addressed to:

sheng-jia.zhang@outlook.com or sheng-jia.zhang@tmmu.edu.cn

ORCID: 0000-0002-6483-6056 (Z.S. Chen)

Summary

Vision plays a critical role in guiding spatial navigation. A traditional view of the visual cortex is to compute a world-centered map of visual space, and visual neurons exhibit diverse tunings to simple or complex visual features. The neural representation of spatio-visual map in the visual cortex is thought to be transformed from spatial modulation signals at the hippocampal-entorhinal system. Although visual thalamic and cortical neurons have been shown to be modulated by spatial signals during navigation, the exact source of spatially modulated neurons within the visual circuit has never been identified, and the neural correlate underpinning a visuospatial or spatio-visual map remains elusive. To search for direct visuospatial and visuodirectional signals, here we record *in vivo* extracellular spiking activity in the secondary visual cortex (V2) from freely foraging rats in a naturalistic environment. We identify that V2 neurons forms a complete spatio-visual map with a wide range of spatial tunings, which resembles the classical spatial map that includes the place, head-direction, border, grid and conjunctive cells reported in the hippocampal-entorhinal network. These spatially tuned V2 neurons display stable responses to external visual cues, and are robust with respect to non-spatial environmental changes. Spatially and directionally tuned V2 neuronal firing persists in darkness, suggesting that this spatio-visual map is not completely dependent on visual inputs. Identification of functionally distinct spatial cell types in visual cortex expands its classical role of information coding beyond a retinotopic map of the eye-centered world.

Introduction

Vision supports the brain's allocentric spatial navigation, such as guiding navigation with distal visual cues (Morris, 1981). During navigation, spatial context modulates neuronal responses in the visual cortex (Flossmann and Rochefort, 2020; Nau et al., 2018; Saleem, 2020) and visual thalamus (Hok et al., 2018). Head movement, orientation, direction and locomotion signals were detected in the rodent V1(Bouvier et al., 2020; Guitchounts et al., 2020a; Guitchounts et al., 2020b; Meyer et al., 2018; Saleem et al., 2013; Velez-Fort et al., 2018). Additionally, coherent coding of spatial signals was found in the rodent primary visual cortex (V1) and hippocampal CA1 subfield (Fournier et al., 2020; Haggerty and Ji, 2015; Ji and Wilson, 2007). Vision and movement are known to jointly contribute to hippocampal place code (Chen et al., 2013). Visual cues strongly influence spatial modulation in the hippocampus (Acharya et al., 2016). Place cells, head-direction cells, border cells and grid cells are also all strongly modulated with rotated visual cues (Chen et al., 2019; Hafting et al., 2005; Jeffery and O'Keefe, 1999; Lever et al., 2009; Muller and Kubie, 1987; Solstad et al., 2008; Taube et al., 1990). Meanwhile, all physical location-based spatial cell types have their corresponding visual analogues, which include spatial view cells, saccade direction cells, visual grid and border cells that have been reported in the monkey and human hippocampal-entorhinal network (Doeller et al., 2010; Julian et al., 2018; Killian et al., 2012; Killian et al., 2015; Nau et al., 2018; Rolls and O'Mara, 1995). Spatial tuning has been established in the dorsal lateral geniculate nucleus (dLGN), V1 and other visual cortical areas along the visual pathway from head-fixed as well as freely foraging animals during spatial navigation tasks (Diamanti et al., 2021; Fiser et al., 2016; Fournier et al., 2020; Hok et al., 2018; Jankowski and O'Mara, 2015; Leinweber et al., 2017; Pakan et al., 2018; Saleem et al., 2013; Saleem et al., 2018; Siegle et al., 2021; Taube, 1995; Vantomme et al., 2020). Recent experimental findings have shown that similar hippocampal-entorhinal network mechanisms supporting navigation also mediate a world-centered representation of visual space (Nau et al., 2018). However, a complete function of visual cortical neurons from freely foraging animals in a naturalistic environment remains elusive. We hypothesize that the source of spatio-visual signals is generated from higher-order visual areas in a top-down manner, instead of inheriting directly from the visual thalamus in a bottom-up manner. To test this, we therefore target our recording on V2 instead of the widely studied V1 (Flossmann and Rochefort, 2020; Haggerty and Ji, 2015; Ji and Wilson, 2007). To physiologically characterize the visuospatial responses of visual cortical cells, we performed *in vivo* single-unit recordings in V2, the downstream higher-order structure of V1, while rats freely foraged in a two-dimensional chamber (**Fig. 1a,** Supplementary **Fig. S1**). Among a total of recorded 1364 well-isolated units, subsets of V2 units

showed significant spatial tunings that resemble the place cell, head-direction cell, border cell, grid cell and conjunctive cell in the traditional hippocampal-entorhinal spatial navigation network. The discovery of diverse and compact spatial tunings of V2 neurons provides a more complete spatio-visual map in the visual cortex, suggesting a neural basis of visual spatial coding for spatial navigation.

Results

We first implanted movable micro-drives connected with four tetrodes into six male Long-Evans adult rats. Recording electrodes were targeted to the higher-order secondary visual cortex. We then recorded spiking activity while rats foraged for randomly scattered ground biscuits in an open two-dimensional square or cylinder enclosure. A total of 1364 well-isolated single units were recorded mainly from deep layers IV to VI (starting around 600 μm below the dura) of V2 across 278 recording sessions. The quality of multiple well-separated clusters and spikes (waveforms) was assessed with two well-established criteria (Supplementary **Fig. S2**). Postmortem histological reconstruction verified that recording electrode positions of all implanted animals were located in V2, with a narrow region approximately 4.5 mm posterior to bregma and 2.5 mm lateral to midline (**Fig. 1a**, Supplementary **Fig. S1**). The distribution of distinct spatially tuned cell types between V2 cortical layers showed a tendency for place cells, head-direction cells and border cells to cluster in layer-V/VI, while grid cells appeared to distribute evenly in deep layers (Supplementary **Fig. S3**). The number of each functionally distinct V2 spatially tuned cells from individually implanted rats was summarized in Supplementary **Fig. S4**.

Place cells in V2

A large number of well-isolated V2 units displayed spatially selective firing patterns with respect to the rat's location in the open field, which was termed as the cell's "firing field" (O'Keefe and Dostrovsky, 1971). We used a strict criterion to define spatially tuned units. If the statistical criterion was relaxed, a higher percentage of V2 units would meet the threshold criterion. V2 place cells were classified if their spatial information (SI) scores were above a stringent 99th percentile of shuffled rate maps. We identified 165/1364 (12.1%) significant spatially modulated V2 units as "place cells" based on their SI scores (**Fig. 1b, c,** Supplementary **Fig. S7**) using population shuffling, which is more stringent than within-cell shuffling (Supplementary **Fig. S6**). This percentage was significantly higher than expected by random selection from the entire shuffled population (**Fig. 1c**; $Z = 41.19$, $P < 0.001$; binomial test with expected P_0 of 0.01 among large samples). Furthermore, we validated spatial tuning of V2 place cells using a maximum-likelihood approach (Supplementary **Fig. S8**). Together, these V2 place receptive fields uniformly covered the environment (**Fig. 1d**, Friedman-Rafsky's MST test, $P =$

0.34, two-tailed *z*-test) (Smith and Jain, 1984). The statistics of peak-to-trough spike width and peak-to-peak amplitude of V2 place cells were shown in Supplementary **Fig. S5a**. A large percentage (143/165, 86.67%) of V2 place cells had a single place field (**Fig. 1e**), where the remaining (26/165, 14.33%) V2 place cells displayed multiple fields (**Fig. 1e**). V2 place cells had 2.17 ± 0.04 bits per spike (all data are shown as mean ± s.e.m. unless specified otherwise) in SI score (**Fig. 1f**). The mean and peak firing rates of V2 place cells were (0.73 ± 0.04 Hz) and (9.68 ± 0.36 Hz), respectively (**Fig. 1g**). The SI score was significantly greater during running than inactive mobility (**Fig. 1h,** Supplementary **S9a,** n = 165, P = 0.000, two-tailed paired *t*-test). The average receptive field size of V2 place cells was 31.98% about the size of the open field (1022.40 ± 39.08 cm^2, **Fig. 1i**). Additionally, V2 place cells had an average spatial coherence of 0.75 ± 0.02 (**Fig. 1j**), and an average spatial sparsity of 0.12 ± 0.01 (**Fig. 1k**).

Between the first and the second halves of single intra-session recordings, V2 place cells displayed a high degree of spatial correlation (**Fig. 1l**, Supplementary **Figs. S10a-c**). There was no significant difference between the "in-field" and "out-field" running speed (14.66 ± 0.18 cm/s vs 14.65 ± 0.16 cm/s, n = 165, P = 0.68, two-tailed paired *t*-test, **Fig. 1m**). Notably, V2 place fields remained stable during three consecutive 60-min light (L)-dark (D)-light (L') recording sessions (each session for 20 min) (**Fig. 1n** and Supplementary **S11**). There were no significant changes in SI (**Fig. 1o**, n = 32, two-sided Wilcoxon signed rank test, L-D: P = 0.08, D-L': P = 0.97 and L-L': P = 0.11), mean firing rate (**Fig. 1p**, same test, L-D: P = 0.60, D-L': P = 0.47 and L-L': P = 0.45) and spatial correlation coefficient (**Fig. 1q**, L-D: P = 0.50, D-L': P =0.14 and L-L': P =0.90), suggesting that V2 spatial firing had little dependence on the purely visual input. Notably, simultaneously recorded place cells, border cells, grid cells and head-direction cells preserved their spatial firing properties in total darkness (Supplementary **Fig. S12**). In remapping experiments of square (S)-circle (C)-square (S'), we found that V2 place cells remapped with the changed SI (**Fig. 1s** and Supplementary **Fig. S15**, n = 45, two-sided Wilcoxon signed rank test, S-C: P = 0.000, C-S': P = 0.000 and S-S': P = 0.74**)**, mean firing rate (**Fig. 1t**, same test, S-C: P = 0.000, C-S': P = 0.000 and S-S': P = 0.30) and spatial correlation coefficient (**Fig. 1u**, S-C: P = 0.000, C-S': P = 0.000 and S-S': P = 0.39), suggesting that the environmental shape influenced the firing properties of V2 place cells. Furthermore, V2 place cells rotated and remained stable during baseline (B)-rotation (R)-baseline (B') when visual cues were rotated by 90° in orientation (**Fig. 1v** and Supplementary **Fig. S13**), as measured by the angle and length of the coordinate vector of the firing field relative to the center of the arena (n = 27, Rayleigh test: for B-R, P = 0.000, r = 0.98, median shift = 92.83°; for R-B', P = 0.000, r = 0.97, median shift = 97.83°; two-

sided Wilcoxon signed rank test, P = 0.000 and 0.000 for B-R and R-B', respectively; see the second and third columns in **Fig. 1w** and **Fig. 1x**). However, for those place cells that did not follow the cue rotation, there were very small angular shifts (n = 24, Rayleigh test: for B-R, P = 0.000, r = 0.99, median shift = 5.22°; for R-B', P = 0.000, r = 0.98, median shift = 5.37°; two-sided Wilcoxon signed rank test, P = 0.95 and 0.42 for B-R and R-B', respectively; see the third and fourth columns in **Fig. 1w**). There was no significant difference in mean firing rate (**Fig. 1y**, n = 27, P = 0.92, 0.51 and 0.73 for R-B', B-R and R-B', respectively) or spatial information (**Fig. 1z**, P = 0.26, 0.97 and 0.21, respectively) from baseline to cue card rotation and then back to baseline. Together with V2 place cells, simultaneously recorded V2 head-direction cells, V2 border cells and V2 grid cells rotated concurrently with the cue card (Supplementary **Fig. S13**). Additionally, simultaneously recorded place cells, border cells, grid cells and head-direction cells on the same microdrive rotated coherently to the visual landmark (Supplementary **Fig. S14**).Therefore, place cells in V2 shared similar spatially selective firing features as the classical hippocampal place cells (O'Keefe and Dostrovsky, 1971).

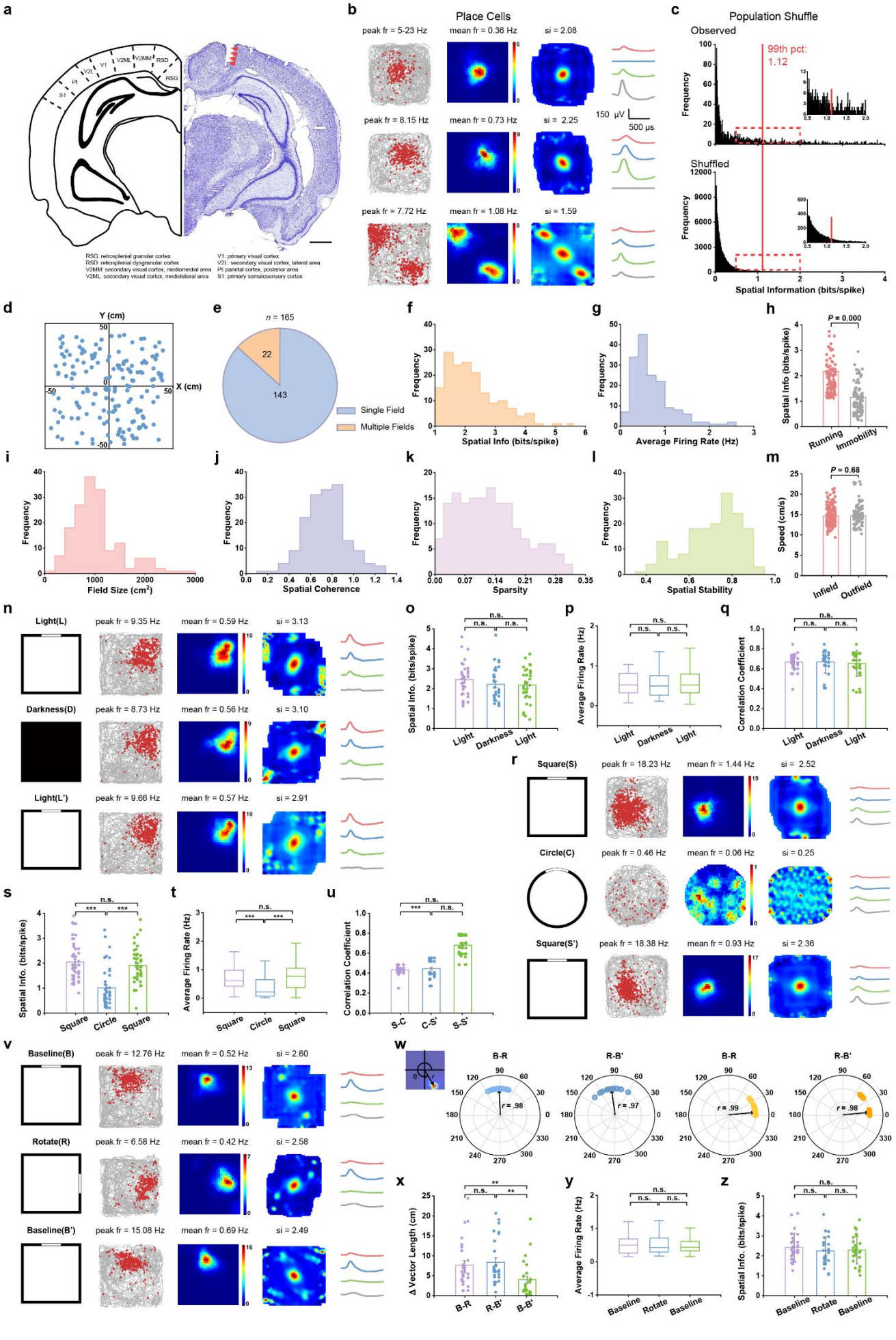

Fig. 1. Place cells in the visual cortex. a, Photograph of a coronal brain section (right) stained with cresyl violet illustrating the track (arrowheads) of the recording electrodes passing through the rat secondary visual cortex (V2). Schematic diagram (left) around V2. Scale bar, 1 mm. **b**, Three representative V2 place cells. First column: rat's run trajectory (grey line) with superimposed spike locations (red dots). Second column: spatial firing rate maps. Firing rate is color-coded with dark blue (red) indicating minimal (maximum) firing rate. The two numbers in the middle panel represent the peak and mean firing rates, respectively. Spatial information (SI) score is labeled at the top of firing rate map. Third column: autocorrelation diagrams. The scale of the autocorrelation maps is twice that of the spatial firing rate maps. Fourth column: average spike waveforms on four electrodes of the same tetrode are shown on the right column. **c**, Distribution of SI for observed data (top panel) and shuffled data (bottom panel). Red line indicates the 99th percentile for the SI score derived from the shuffled data. The inset shows the zoomed-in of the red dashed box. **d**, Distribution of the center of firing fields from all recorded V2 place cells showed uniformly distributed patterns (n = 165, Friedman-Rafsky's MST test, P = 0.34, two-tailed z-test). **e**, Venn diagram showing the number of V2 place cells with one or more firing fields. **f-g**, Distribution of mean firing rate and SI derived from all V2 place cells. **h**, SI was significantly higher during running than during slow movement or immobility. **i**, Distribution of place field sizes. **j-l**, Distribution of spatial coherence, sparsity and intra-trial spatial stability between the first and second halves of all identified V2 place cells (n = 165). **m**, No change in running speed between the within- and outside-firing fields (n = 165, two-tailed paired t-test, P = 0.68). **n**, Firing properties of one representative V2 place cell in the light condition and total darkness. First column: schematic of the experimental paradigms; responses of the place cell across light (upper panel), darkness (middle panel) and back to light condition (lower panel). **o-p**, Both SI score (L-D: P = 0.08, D-L': P = 0.97 and L-L': P = 0.11) and mean firing rate (n = 32, two-sided Wilcoxon signed rank test, L-D: P = 0.60, D-L': P = 0.47 and L-L': P = 0.45) remained stable in the light condition, in total darkness and back to light condition. **q**, Place cells exhibited stable tuning between the switch from light (L) to darkness (D) and then light (L') conditions (n = 32, two-sided Wilcoxon signed rank test, L-D: P = 0.50, D-L': 0.14 and L-L': 0.90). **r**, Responses of one representative V2 place cell in square enclosure and circle. First column: schematic of the experimental paradigms; firing patterns of the place cell in the square enclosure (upper panels), circle (middle panels) and back to the square enclosure (lower panels). **s-t**, Quantification of SI in the remapping experiment (n = 45, two-sided Wilcoxon signed rank test, S-C: P = 0.000, C-S': P = 0.000 and S-S': P = 0.74) and mean firing rate (S-C: P = 0.000, C-S': P = 0.000 and S-S': P = 0.30). **u**, Spatial correlation showed significant remapping in different environmental shapes (S-C: P = 0.000, C-S': P = 0.000 and S-S': P = 0.39). **v**, Responses of one representative V2 place cell under visual cue manipulation. First column: schematic of the experimental paradigms; firing properties of the place cell in the baseline condition (upper panels), counterclockwise 90° cue-rotation manipulation (middle panels) and back to the original baseline condition (lower panels). **w**, Firing properties of place cells following cue card rotation. Upper left panel: the angle and length of the coordinate vector of the field center relative to the center of the box. First and second columns: polar plots showing angular shifts in the direction of the coordinates of the firing field center relative to the box center (n = 27, B-R, Rayleigh test, P = 0.000, r = 0.98, median shift = 92.83°; R-B', Rayleigh test, P = 0.000, r = 0.97, median shift = 97.83°; two-sided Wilcoxon signed rank test, P = 0.000 and 0.000 for B-R and R-B', respectively). Third and fourth columns: similar to the first and second columns, except for place cells not following the cue card manipulation. Polar plot showing angular shifts in direction of the coordinates of the firing field center relative to the box center (n = 24, B-R, Rayleigh test, P = 0.000, r = 0.99, median shift = 5.22°; R-B', Rayleigh test, P = 0.000, r = 0.98, median shift = 5.37°; two-sided Wilcoxon signed rank test, P = 0.95 and 0.42 for B-R and R-B', respectively). **x**, The difference in vector length was smaller between two baseline conditions (n = 27, two-sided Wilcoxon signed rank test, P = 0.18, 0.002 and 0.008, respectively). **y-z**, Among baseline, cue card

rotation and baseline, neither mean firing rates (n = 27, two-sided Wilcoxon signed rank test, P = 0.92, 0.51 and 0.73, respectively) nor SI scores (n = 27, two-sided Wilcoxon signed rank test, P = 0.26, 0.97 and 0.21, respectively) were significantly different.

Border cells in V2

Border cells fire specifically whenever an animal forages close to one or multiple physically-defined local boundaries of an open field (Lever et al., 2009; Solstad et al., 2008). Next, we examined whether traditional border cells existed in the V2. We assigned a V2 unit as a border cell if its border score (BS) was larger than the 99th percentile of shuffled distribution (**Fig. 2b**). The histograms of peak-to-trough spike width and peak-to-peak amplitude were shown in Supplementary **Fig. S5b**. Overall, 85/1364 (6.23%) recorded V2 units were categorized as border cells (**Fig. 2a** and Supplementary **Fig. S16**), and this percentage was significantly higher than expected by random selection from the entire shuffled population (**Fig. 2b**; Z = 19.41, P < 0.001; binomial test with expected P_0 of 0.01 among large samples). The BS was higher during animal's running (> 2.5 cm/s) than immobility (2.5 cm/s) (**Fig. 2d** and Supplementary **Fig. S9b**, n = 85, P = 0.000, two-tailed paired t-test). V2 border cell had a mean firing rate of 1.51 ± 0.21 Hz (**Fig. 2e**) and an average BS of 0.69 ± 0.01 (**Fig. 2f**). Similar to the classical border cells reported in the medial entorhinal cortex (mEC) and subiculum (Solstad et al., 2008), V2 border cells fired along a single border (n = 39/85, 45.88%) while others discharged actively along with two (n = 15/85, 17.65%), three (n = 3/85, 3.53%) or even four (n = 28/85, 32.94%) borders within the open arena (**Fig. 3c** and Supplementary **Fig. S16**).

During consecutive 60-min light-dark-light sessions (**Fig. 2g** and Supplementary **Fig. S17**), there was no statistically significant difference in BS (**Fig. 2h**, n = 15, two-sided Wilcoxon signed rank test, L-D: P = 0.53, D-L': P = 0.69 and L-L': P = 0.73**)** and mean firing rate (**Fig. 2i**, L-D: P = 0.12, D-L': P = 0.31 and L-L': P = 0.59), indicating that border tuning in V2 is independent on the visual input. Introduction of a new wall into the square arena produced a new border field on the distal side of the new wall for one-sided border cells (**Fig. 2j**) while the newly inserted wall evoked new border fields on both proximal and distal sides of the wall insert for four-sided border cells (**Figs. 2k-m** and Supplementary **Fig. S20**, n = 15) (Solstad et al., 2008)**.** For the same V2 border cell, there was no significant change in mean firing rate (n = 12, two-sided Wilcoxon signed rank test, S-C: P = 0.31, C-S': P = 0.54 and S-S': P = 0.81) and BS (S-C: P = 0.94, C-S': P = 0.64 and S-S': P = 0.72) while navigating between circular and square environments (**Figs. 2n-p** and Supplementary **Fig. S18**). Additionally, removal of four outer walls from the enclosure on the elevated platform preserved similar V2 border fields (**Fig. 2q** and Supplementary **Fig. S19**), suggesting that V2 border cells anchored only

to geometric boundaries instead of physical edges. No significant change in mean firing rate was observed between the standard walled enclosure and the elevated wall-free platform (**Fig. 2s**, $n = 9$, two-sided Wilcoxon signed rank test, B-E: $P = 0.52$, E-B': $P = 0.21$ and B-B': $P = 0.52$), yet there was a decrease in BS on the elevated platform (**Fig. 2r**, B-E: $P = 0.02$, E-B': $P = 0.05$ and B-B': $P = 0.86$). Therefore, V2 border cells resembled those classical border cells reported in the rat mEC and subiculum (Lever et al., 2009; Solstad et al., 2008).

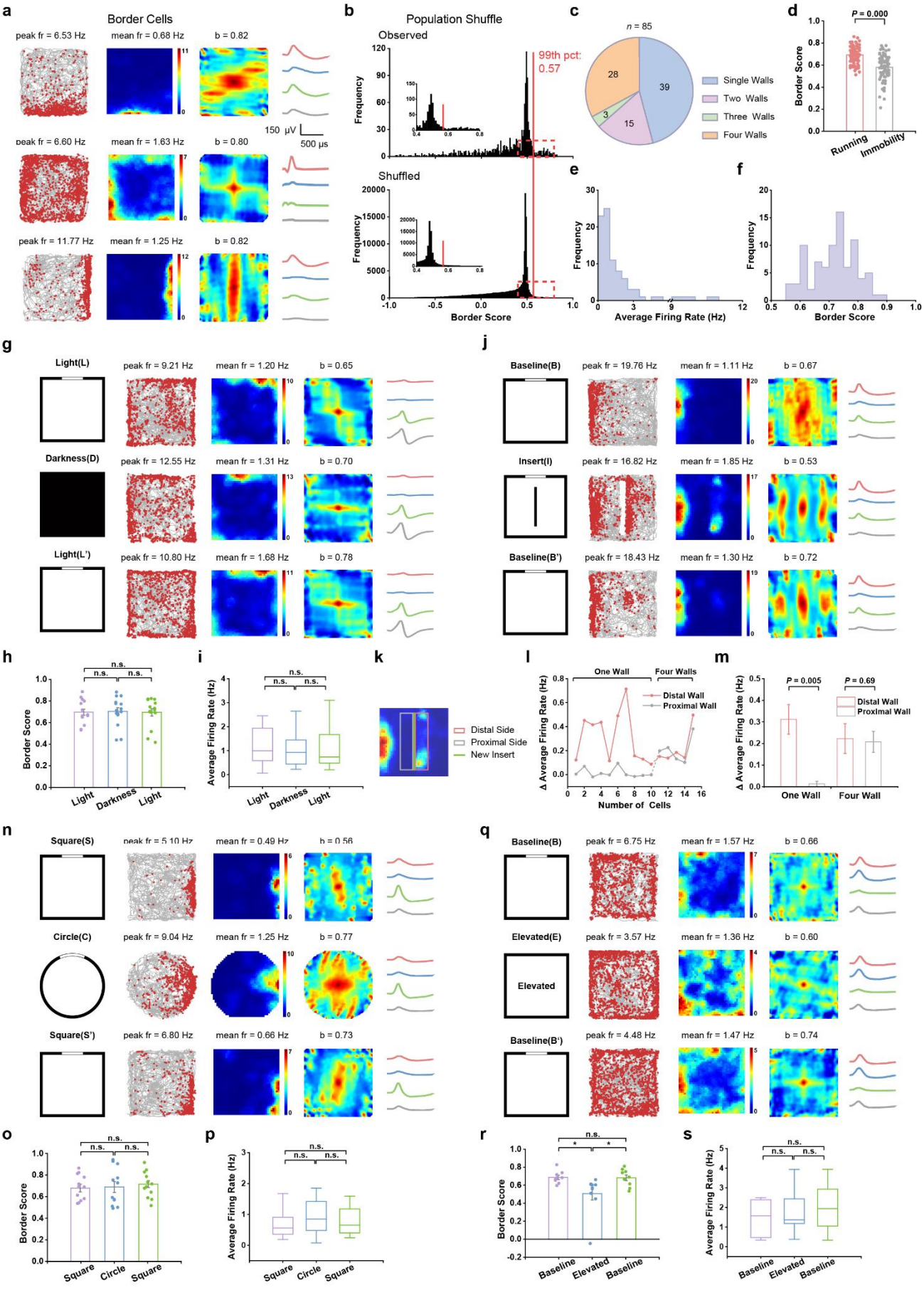

Fig. 2. Border cells in the visual cortex. a, Three representative border cells identified from the secondary visual cortex. Notations and symbols are the same as those in Fig. 1a. Border score (BS) for each border cell is labelled at the top of firing rate map. **b**, Distribution of BS for observed data (top panel) and shuffled data (bottom panel). Red line indicates the 99th percentile for BS derived from the shuffled data. The inset shows the zoomed-in view of the red dashed box. **c**, Venn diagram showing the number of border cells having firing fields along one, two, three and four walls, respectively. **d**, BS was statistically higher during running than slow movement or immobility (n = 85, two-tailed paired t-test, P = 0.000). **e-f**, Distribution of mean firing rate and BS derived from all identified border cells. **g**, Firing properties of one representative border cell in the light condition and total darkness. Notations and symbols are the same as those in **Fig. 1n**. **h-i**, Quantification of BS in the L-D-L' conditions (n = 15, two-sided Wilcoxon signed rank test, L-D: P = 0.53, D-L': P = 0.69 and L-L': P = 0.73, respectively) and mean firing rate (n = 15, two-sided Wilcoxon signed rank test, L-D: P = 0.12, D-L': P = 0.31 and L-L': P = 0.59). **j**, Responses of one representative border cell before and after insertion of a new wall. First column: Schematic of the experimental paradigms. Third column: Responses of the border cell from baseline (upper panels), wall insertion (middle panels) and baseline conditions (lower panels). **k**, Schematic showing the method of estimating responses to the insertion of a discrete wall (green line). Firing rates were calculated in both 15-cm-wide distal side (red box) and proximal side (gray box) of the new insert. Proximal and distal sides were determined by the location relative to that of the original border firing field. **l**, Difference in mean firing rate between (distal and proximal) wall insertion and baseline. Data from ten V2 units with firing fields along a single wall and five V2 units with firing fields along four walls. **m**, The distal side had a higher mean firing rate than the proximal side for border cells with firing field along a single wall (n = 10, two-sided Wilcoxon signed rank test, P = 0.005). For border cells firing along four walls, distal and proximal sides had similar mean firing rates (n = 5, two-sided Wilcoxon signed rank test, P = 0.67). **n**, Responses of one representative V2 border cell in square enclosure and circle. Notations and symbols are the same as those in Fig. 1r. **o-p**, Quantification of BS (n = 12, two-sided Wilcoxon signed rank test, S-C: P = 0.94, C-S': P = 0.64 and S-S': P = 0.72) and mean firing rate (S-C: P = 0.31, C-S': P = 0.54 and S-S': P = 0.81) in the square enclosure (top panels), circle (middle panels) and back to the square enclosure (bottom panels). **q**, Responses of one representative V2 border cell in baseline (top panels), elevated platform without walls (middle panels) and baseline condition (bottom panels). First column: schematic of the experimental paradigms. **r-s**, Quantification of mean firing rate (n = 9, two-sided Wilcoxon signed rank test, S-C: P = 0.52, C-S': P = 0.21 and S-S': P = 0.52) and BS during baseline, elevated platform without walls and back to baseline sessions (n = 9, two-sided Wilcoxon signed rank test, B-E: P = 0.02, E-B': P = 0.05 and B-B': P = 0.86).

Grid cells in V2

Hexagonal firing patterns of classical grid cells have been reported in the rat mEC (Hafting et al., 2005). To identify potential grid cells in V2 (**Fig. 3a** and Supplementary **Fig. S21**), we calculated the gridness score (GS, a metric measuring the degree and symmetry of spatial periodicity of hexagonal firing patterns) based on rotated spatial autocorrelation of the firing rate maps. We classified a V2 unit as a grid cell if its GS was higher than the 99th percentile value of the shuffled data. A small percentage (70/1364 or 5.13%) V2 units met this significance criterion (**Fig. 3b**). This percentage was significantly higher than expected by random selection from the entire shuffled population (**Fig. 3b**; Z = 15.34, P <

0.001; binomial test with expected P_0 of 0.01 among large samples). V2 grid cells had a mean firing rate of 3.75 ± 0.72 Hz (**Fig. 3c**) and an average GS of 0.75 ± 0.04 (**Fig. 3d**). We further quantified the properties of V2 grid cells (average grid spacing: 67.44 ± 1.28 cm, **Fig. 3e**; median grid orientation: 30.00°, **Fig. 3f**). Additionally, the fluctuation in V2 grid spacing was not a result of interindividual differences between rats (Supplementary **Fig. S4c**).

Furthermore, we found that V2 grid cells showed higher GSs during running (> 2.5 cm/s) than slow mobility (< 2.5 cm/s) (**Fig. 3g** and Supplementary **Fig. S9c**, n = 70, P = 0.000, two-tailed paired t-test). Additionally, V2 grid cells maintained hexagonal firing patterns in total darkness (**Fig. 3h** and Supplementary **Fig. S22**), and there was no significant change in mean firing rate (**Fig. 3i**, n = 16, two-sided Wilcoxon signed rank test, L-D: P = 0.50, D-L': P = 1.00 and L-L': P = 0.80) and GS (**Fig. 3j**, L-D: P = 0.57, D-L': P = 0.80 and L-L': P = 0.28) during consecutive light-dark-light sessions, suggesting that visual inputs are not essential for maintaining visual grid firing patterns. Discharging patterns of V2 grid cells in a larger environment (1.5 × 1.5 m^2 box) preserved multiple regular triangular structures and high GS similar to those in a smaller (1 × 1 m^2 box) enclosure (Supplementary **Figs. S23**, mean firing rate, n = 13, two-sided Wilcoxon signed rank test, S-L: P = 0.97, L-S': P = 0.92 and S-S': P = 0.97; GS, S-L: P = 0.023, L-S': P = 0.023 and S-S': P = 0.86), rejecting the false positive discovery due to triangular node structures (**Figs. 3k-m** and Supplementary **Fig. S23**). The decrease of GS in large environments are consistent with the idea that grid cells anchor locally (Stensola et al., 2015). Overall, V2 grid cells exhibited similar features as those identified in the rat mEC (Hafting et al., 2005).

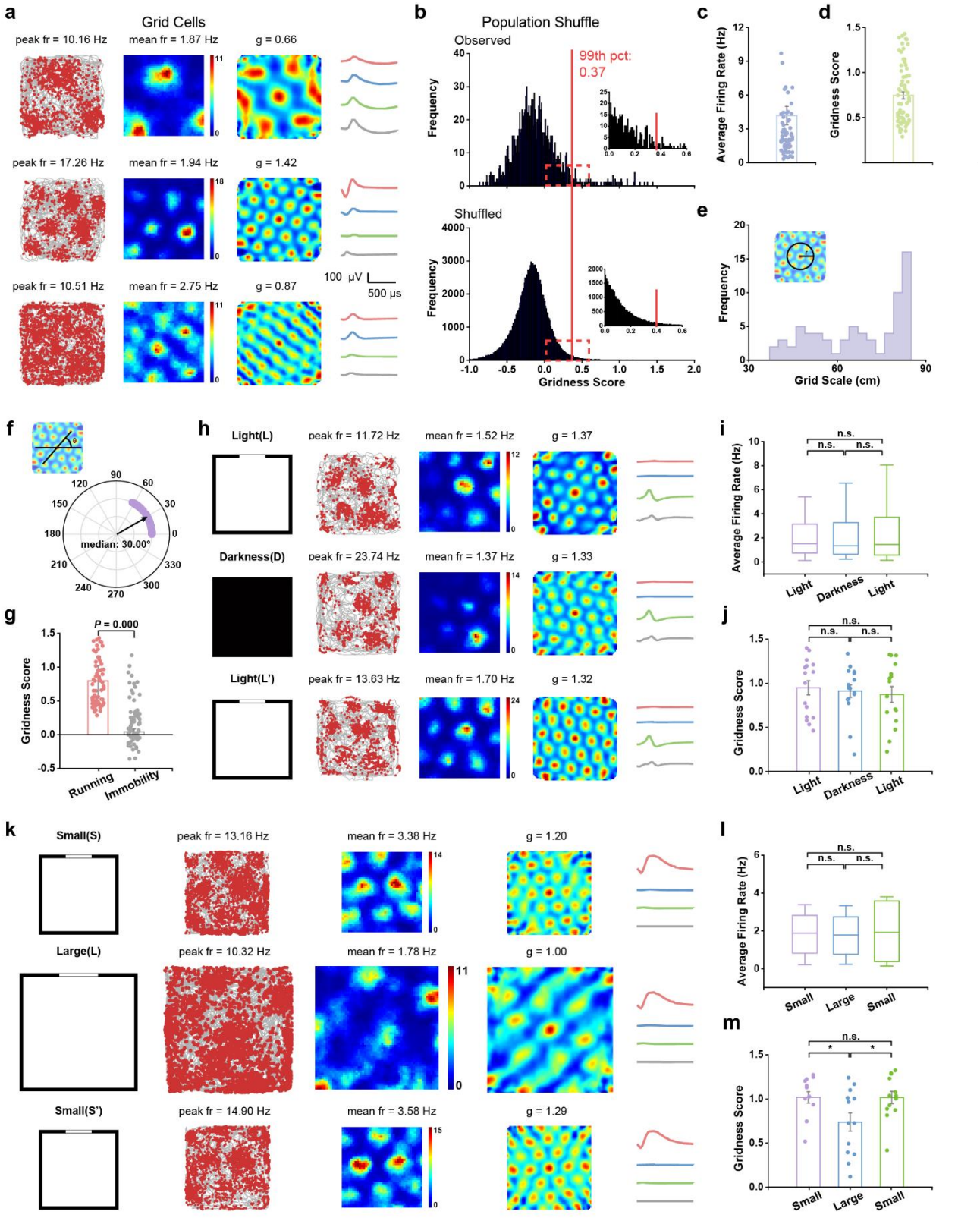

Fig. 3. Grid cells in the visual cortex. **a**, Three representative grid cells recorded from the visual cortex. Similar symbol and notations as Fig. 1a. Gridness score (GS) for each grid cell is labelled at the top of firing rate map. **b**, Distribution of GS for observed data (top panel) and shuffled data (bottom panel). Red line indicates the 99th percentile for GS in the

shuffled data. The inset shows the zoomed-in view of the red dashed box. **c-d**, Mean firing rate and GS statistics for all identified V2 grid cells. **e-f**, Distribution of gridness scales and grid orientations derived from all identified V2 grid cells. **g**, Grid firing patterns were more pronounced during running than immobility (n = 70, two-tailed paired t-test, P = 0.000). **h**, Firing properties of one representative V2 gird cell in the light condition and total darkness. **i-j**, Quantification of mean firing rate (n = 16, two-sided Wilcoxon signed rank test, L-D: P = 0.50, D-L': P = 1.00 and L-L': P = 0.80, respectively) and GS in the L-D-L' conditions (n = 16, two-sided Wilcoxon signed rank test, L-D: P = 0.57, D-L': P = 0.80 and L-L': P = 0.28, respectively). **k**, Firing properties of one representative V2 gird cell in an enclosure of different size. **l-m**, Quantification of mean firing rate (n = 13, two-sided Wilcoxon signed rank test, S-L: P = 0.97, L-S': P = 0.92 and S-S': P = 0.97, respectively) and GS in varying sizes of running boxes: 1 × 1 m^2 (S), 1.5 ×1.5 m^2 (L) and 1 × 1 m^2 (S') (n = 13, two-sided Wilcoxon signed rank test, S-L: P = 0.023, L-S': P = 0.023 and S-S': P = 0.86). The GS decrease in a larger environment was consistent with the notion that grid cells anchor locally.

Head-direction and conjunctive cells in V2

Head-direction (HD) cells discharge rapidly only when the animal's head points towards a particular azimuth (direction) in the horizontal plane (Taube et al., 1990). We next investigated whether classical head-direction cells are present in the visual cortex. To categorize the preferred firing direction of V2 units, we used the mean vector length (MVL) to calculate the head directional tuning across 360°. A V2 unit was classified as a HD cell if its MVL exceeded the 99th percentile of shuffled data (**Fig. 4b**). About 8.65% (92/1364) recorded V2 units met the significant criterion and had strong modulation to the animal's heading direction (**Fig. 4a** and Supplementary **Fig. 25**). This percentage was significantly higher than expected by random selection from the entire shuffled population (**Fig. 4b**; Z = 28.40, P < 0.001; binomial test with expected P_0 of 0.01 among large samples). We applied a maximum-likelihood correction procedure to alleviate the influence of spatial selectivity on biased HD sampling. Upon correction, about 77.97% (92/118) HD cells remained unchanged in their directional firing rate histograms (Supplementary **Fig. S24**), yet with 4.06% decrease in directional information; this was consistent with HD cells in the rat presubiculum and postsubiculum (Burgess et al., 2005). We further analyzed the remaining 92 V2 HD cells that passed the stringent 99th percentile significance threshold, and these V2 cells had a mean firing rate of 2.09 ± 0.22 Hz (**Fig. 4c**) and an average MVL of 0.58 ± 0.06 (**Fig. 4d**). The preferred firing direction was stronger during running (> 2.5 cm/s) than immobility (< 2.5 cm/s) (**Fig. 4e** and Supplementary **Fig. S9d**, n = 92, P = 0.000, two-tailed paired t-test), yet the angular velocity between "preferred firing directions" and "non-preferred firing direction" was not significantly different (**Fig. 4f**, n = 92, P = 0.58, two-tailed paired t-test). The preferred firing direction of HD cell population uniformly distributed across 360^o (**Fig. 4g**, n = 92, Rayleigh test for uniformity, r = 0.074, P = 0.61). The intra-trial directional selectivity remained stable between the first and second

halves of individual recording sessions (**Fig. 4h** and Supplementary **Figs. S10d-f**). The full tuning width at half maximum (FWHM) of recorded V2 HD cells was 79.38º ± 8.27º, which was slightly greater than the statistic of presubicular HD cells but similar to the statistic in the lateral mammillary nuclei (**Fig. 4i** and Supplementary **Fig. S26**). Similar to those conjunctive cells reported in the rat mEC (Sargolini et al., 2006), we also found conjunctive place × HD cells (5/165 place cells), conjunctive border × HD cells (5/85 border cells) and conjunctive grid × HD cells (6/70 grid cells) in V2 (**Figs. 4j, k**).

We further tested the effect of visual landmarks on V2 HD cells during consecutive light-dark-light sessions (**Fig. 4l**). V2 head-direction cells maintained their preferred firing directions in the darkness (n = 28, Rayleigh test, for L-D: r = 0.97, median shift = 3.49°; for D-L': r = 0.96, median shift = 7.44°; two-sided Wilcoxon signed rank test, P = 0.44 and 0.96 for D-L and L-D', respectively, **Fig. 4m**). There was no significant change in angular correlation (n = 28, two-sided Wilcoxon signed rank test, P = 0.67 between D-L and L-D', **Fig. 4n**), MVL (P = 0.52, 0.47 and 0.36, respectively, **Fig. 4o**) or mean firing rate (P = 0.21, 0.67 and 0.41, respectively, **Fig. 4p**), indicating that V2 HD tuning is not totally dependent upon visual inputs. About half (15/29) of V2 HD cells (**Fig. 4q** and Supplementary **Fig. S27**) produced a nearly equal shift in preferred firing direction (n = 15, Rayleigh test: for B-R, r = 0.96, median shift = 92.23°; for R-B', r = 0.96, median shift = 89.63°; two-sided Wilcoxon signed rank test, P = 0.006 and 0.002 for B-R and R-B', respectively, **Fig. 4r**). V2 HD cells also anchored to salient visual cues with no significant change in MVL (n = 15, two-sided Wilcoxon signed rank test, P = 0.10, 0.53 and 0.38, respectively, **Fig. 4t**) or mean firing rate (P = 0.78, 0.46 and 0.26, respectively, **Fig. 4u**). However, about half (14/29) of V2 HD cells did not follow the rotated cue card (n = 14, Rayleigh test: for B-R, r = 0.96, median shift = 10.41°; for R-B', r = 0.96, median shift = 7.43°; two-sided Wilcoxon signed rank test, P = 0.48 and 0.06 for B-R and R-B', respectively, **Fig. 4s**). Put together, V2 HD cells shared similar characteristics of other HD cells in the hippocampal-entorhinal network and the presubiculum (Taube, 2007).

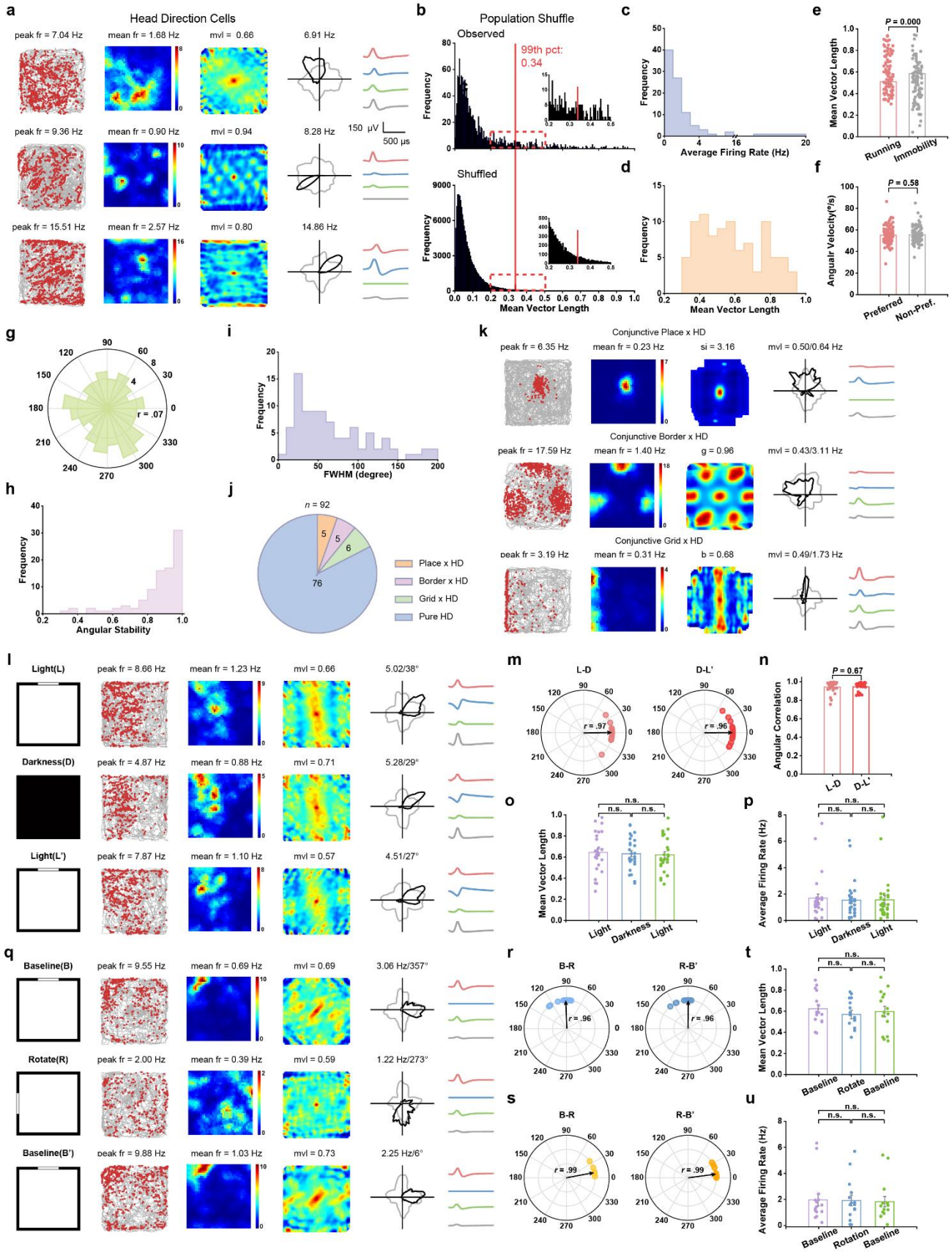

335

336 **Fig. 4. Head-direction (HD) and conjunctive cells in the visual cortex. a**, Three representative V2 HD cells. Similar
337 symbol and notations as Fig. 1a. Mean vector length (MVL) for each HD cell is labelled at the top of firing rate map. Fourth

column: HD tuning curves (black) plotted against dwell-time polar plot (grey). The directional plots show strong head directional tuning. **b**, Distribution of MVL in observed data (top panel) and shuffled data (bottom panel). Red line indicates the 99th percentile for MVL derived from the shuffled data. The inset shows the zoomed-in of red dashed box. **c-d**, Distribution of mean firing rate and MVL for all V2 HD cells. **e**, HD tuning was stronger during running than slow movement or immobility (n = 92, two-tailed paired t-test, P = 0.000). **f**, Angular velocity was similar between the preferred and non-preferred firing directions for all V2 HD cells (n = 92, two-tailed paired t-test, P = 0.58). **g**, Polar plot showing the distribution of preferred direction for all HD cells (n = 92, Rayleigh test for uniformity: r = 0.074, P = 0.61). **h**, Distribution of intra-trial angular stability between the first and second halves derived from all HD cells (n = 92). **i**, Distribution of tuning widths defined as full width at half maximum (FWHM) of directional tuning curves derived from all HD cells (n = 92). **j**, Venn diagram showing the composition of conjunctive HD cells and pure HD cells. **k**, Representative conjunctive Place × HD, Border × HD and Grid × HD cells. **l**, Firing properties of one representative V2 HD cell in the light condition and darkness. **m**, Polar plot showing angular shifts in the preferred firing direction for all HD cells in the L-D-L' conditions. V2 HD cells maintained their preferred firing directions in darkness (n = 28, L-D, Rayleigh test, r = 0.97, median shift = 3.49°; D-L', Rayleigh test, r = 0.96, median shift = 7.44°; two-sided Wilcoxon signed rank test, P = 0.44 and 0.96 for D-L and L-D', respectively). **n**, V2 HD cells showed high angular correlation in the L-D-L' conditions (n = 28, two-sided Wilcoxon signed rank test, P = 0.67 between D-L and L-D'). **o**, MVL was not significantly different in the L-D-L' conditions (n = 28, two-sided Wilcoxon signed rank test, P = 0.52, 0.47 and 0.36, respectively). **p**, Mean firing rates remained stable in the L-D-L' conditions (n = 28, two-sided Wilcoxon signed rank test, P = 0.21, 0.67 and 0.41, respectively). **q**, Responses of one representative V2 HD cell under visual cue manipulation. Schematic of the experimental paradigms (left column); firing properties of V2 HD cells in baseline (upper panels), counterclockwise 90° cue-rotation manipulation (middle panels) and back to baseline (lower panels). **r**, Firing properties of V2 HD cells following cue card rotation. Polar plot showing angular shifts in the preferred firing direction from light condition to total darkness (B-R, left) and from total darkness back to light condition (R-B', right) for HD cells. V2 HD cells maintained their preferred firing directions in darkness (n = 15, B-R, Rayleigh test, r = 0.96, median shift = 92.23°; R-B', Rayleigh test, r = 0.96, median shift = 89.63°; two-sided Wilcoxon signed rank test, P = 0.006 and 0.020 for B-R and R-B', respectively). **s**, Same as panel **r** except for V2 HD cells that did not follow the cue card manipulation (n = 14, B-R, Rayleigh test, r = 0.96, median shift = 10.41°; R-B', Rayleigh test, r = 0.96, median shift = 7.43°; two-sided Wilcoxon signed rank test, P = 0.48 and 0.06 for B-R and R-B', respectively). **t**, MVL did not change by cue card manipulation (n = 15, two-sided Wilcoxon signed rank test, P = 0.10, 0.53 and 0.38, respectively). **u**, Mean firing rates were not significantly different between consecutive baseline, cue card rotation and baseline conditions (n = 15, two-sided Wilcoxon signed rank test, P = 0.78, 0.46 and 0.26, respectively).

Discussion

The brain is responsible for transforming and integrating multimodal sensory information in the environment into neural representations that can be used for perception and action. The classical hippocampal-entorhinal network is fundamental to guide spatial navigation, displaying distinct spatially tuned cells in rodents, bats and nonhuman primates (Buzsaki and Moser, 2013). Sensory input and movement are coupled in real world, and it remains unclear how sensory input provides a

complementary spatial or cognitive map while navigating in a naturalistic environment. Recently, strong spatial tuned neurons have been found in the retrospelinal cortex (RSC) (Alexander and Nitz, 2017; van Wijngaarden et al., 2020), posterior parietal cortex (PPC) (Whitlock et al., 2012; Wilber et al., 2014), and primary somatosensory cortex (Long and Zhang, 2021). Vision supports spatial navigation by providing distal visual cues and identifying visual landmarks (Flossmann and Rochefort, 2020; Nau et al., 2018; Saleem, 2020). It has been shown that visual thalamic and cortical neurons are modulated by spatial signals in both virtual and naturalistic environments (Diamanti et al., 2021; Fiser et al., 2016; Fournier et al., 2020; Hok et al., 2018; Jankowski and O'Mara, 2015; Leinweber et al., 2017; Pakan et al., 2018; Saleem et al., 2013; Saleem et al., 2018; Taube, 1995; Vantomme et al., 2020). Spatial representations discovered in multiple visual areas is not surprising since the visual system is responsible for transforming sensory information from eye-centered to world-centered coordinates and estimating self-location (Fournier et al., 2020). Visual cues may provide a bias for position estimate based on non-visual cues (such as distance or speed) in the context of predictive coding(Acharya et al., 2016; Rao and Ballard, 1999; Stachenfeld et al., 2017). Although many studies focused on how visual information influences spatial tunings of the hippocampal-entorhinal network or whether responses of visual neurons are transformed from the hippocampal-entorhinal network, the neural basis of the spatial navigation system in visual cortex remains unclear. Our study provides the first identification and systematic characterization of four functionally distinct spatial cell types in V2, which may form the basis of a compact visual spatial navigation system. These diverse spatial tunings resemble those reported in the classical hippocampal-entorhinal network (Buzsaki and Moser, 2013) and identified recently in the rat primary somatosensory cortex (Long and Zhang, 2021).These recent and current findings challenge the traditional view, and suggests the cognitive maps are more widely represented in the brain than traditionally thought (O'Mara and Aggleton, 2019); Supplementary **Fig. S28**).

The dLGN, being the one synapse upstream structure of the V1, displays place cells (Hok et al., 2018). Multiple lines of evidence have shown that V1 neurons are also modulated by animal's spatial position (Diamanti et al., 2021; Fiser et al., 2016; Flossmann and Rochefort, 2020; Fournier et al., 2020; Haggerty and Ji, 2015; Ji and Wilson, 2007). Calcium imaging in head-fixed mice in a virtual reality environment demonstrated that spatial modulation in V1 strengthens with experience as well as with active behavior (Diamanti et al., 2021). The V2, being the downstream structure of V1, have been studied in spatial navigation tasks with reported 5% egocentric boundary cells (Gofman et al., 2019). However, their implanted electrode location was closer to the postrhinal cortex (POR) than V2, which may explain the difference between their findings and ours. Additionally, the medial and lateral PPC

display spatial coding (Nitz, 2006; Save and Poucet, 2009; Whitlock et al., 2012; Wilber et al., 2014). As the rat PPC is located rostral to the primary and secondary visual cortical areas, and caudal to the somatosensory cortex (~3.5-5 mm posterior of bregma), the exact location of the implanted electrodes may explain the difference in experimental findings (Gofman et al., 2019; Whitlock et al., 2012).

An important question remains: where do the V2 spatial and directional signals come from? In the visual hierarchy, the V2 receives strong feedforward connections from V1, and sends strong connections to higher visual cortical areas as well as feedback connections to V1. The role of V2 in visual cortex has been widely investigated, splitting the dorsal and ventral streams. The ventral visual-to-hippocampal stream is known to play an important role in visual memory or object-recognition memory (Bussey and Saksida, 2007; Lopez-Aranda et al., 2009). Feedback signals from the classical hippocampal-entorhinal GPS network might contribute to the source of non-visual navigational signals in V2. There are reciprocal projections between V2 and several parahippocampal areas including the perirhinal cortex (PER), POR, RSC, MEC, lateral entorhinal cortex (LEC), presubiculum (PrS) and parasubiculum (PaS) (Olsen et al., 2017), which have been reported to encode both egocentric and allocentric spatial and directional information (Alexander et al., 2020). Although there is a lack of direct intrinsic projections between V2 and hippocampus, spatial and directional representations of V2 might be influenced by the hippocampal spatial information through indirect cortico-cortical connections such as the RSC, which is known to encode cortical spatial and directional signals (Mao et al., 2017; Mao et al., 2018; van Strien et al., 2009). Development of large-scale multi-site *in vivo* electrophysiological recording techniques may prove crucial to provide a complete picture of sensory coding of visual systems (Buzsaki et al., 2015; Koay et al., 2020; Siegle et al., 2021). Converging evidence has shown that higher-order visual areas such as V2 may encode additional non-visual cognitive cues including the location, direction and motion. This is also consistent with spatial modulation signals being observed only in higher visual cortices but not in lower visual cortices along the visual hierarchy (Diamanti et al., 2021). We envision that the visual cortex encodes a compact spatial map in parallel to the hippocampal-entorhinal network, and provides a complementary multimodal cognitive mapping of the external world. Just like the hippocampal neurons can jointly encode space and time (Buzsaki and Moser, 2013; Eichenbaum, 2014), many sensory cortical neurons may have mixed selectivity in complex tasks (Siegle et al., 2021; Steinmetz et al., 2019). It is very likely that the spatial modulation is an omnipresent property of pyramidal neurons across many sensory cortices (Hawkins et al., 2018).

It remains to be determined whether these high-order visual areas form the unique neural basis of spatio-visual map. A causal circuit dissection based on optogenetic inactivation of individual visual areas along the visual thalamocortical pathway may help answer this question in the future (Buzsaki et al., 2015; Zhang et al., 2013). It is important to distinguish the visuospatial or spatio-visual map in the visual system between active sensing (e.g., active vision and active navigation) and passive sensing (e.g., purely visual exploration), or between naturalistic and virtual reality environments. Proprioceptive feedback and sensorimotor integration may play a vital role in reshaping spatial selectivity of hippocampal and cortical neurons (Acharya et al., 2016; Aghajan et al., 2015; Ravassard et al., 2013). It may not come as a surprise that the spatio-visual map in visual cortex encoded both egocentric and allocentric spatial cues in parallel (Bicanski and Burgess, 2020; LaChance et al., 2019; Wang et al., 2020). How and whether hippocampal-entorhinal spatial signals interact with non-visual navigational signals in the visual cortex awaits for further investigation.

References

Acharya, L., Aghajan, Z.M., Vuong, C., Moore, J.J., and Mehta, M.R. (2016). Causal Influence of Visual Cues on Hippocampal Directional Selectivity. Cell *164*, 197-207.

Aghajan, Z.M., Acharya, L., Moore, J.J., Cushman, J.D., Vuong, C., and Mehta, M.R. (2015). Impaired spatial selectivity and intact phase precession in two-dimensional virtual reality. Nature neuroscience *18*, 121-128.

Alexander, A.S., Carstensen, L.C., Hinman, J.R., Raudies, F., Chapman, G.W., and Hasselmo, M.E. (2020). Egocentric boundary vector tuning of the retrosplenial cortex. Science advances *6*, eaaz2322.

Alexander, A.S., and Nitz, D.A. (2017). Spatially Periodic Activation Patterns of Retrosplenial Cortex Encode Route Sub-spaces and Distance Traveled. Current biology : CB *27*, 1551-1560 e1554.

Bicanski, A., and Burgess, N. (2020). Neuronal vector coding in spatial cognition. Nature reviews Neuroscience *21*, 453-470.

Bouvier, G., Senzai, Y., and Scanziani, M. (2020). Head Movements Control the Activity of Primary Visual Cortex in a Luminance-Dependent Manner. Neuron *108*, 500-511 e505.

Burgess, N., Cacucci, F., Lever, C., and O'Keefe, J. (2005). Characterizing multiple independent behavioral correlates of cell firing in freely moving animals. Hippocampus *15*, 149-153.

Bussey, T.J., and Saksida, L.M. (2007). Memory, perception, and the ventral visual-perirhinal-hippocampal stream: thinking outside of the boxes. Hippocampus *17*, 898-908.

Buzsaki, G., and Moser, E.I. (2013). Memory, navigation and theta rhythm in the hippocampal-entorhinal system. Nature neuroscience *16*, 130-138.

Buzsaki, G., Stark, E., Berenyi, A., Khodagholy, D., Kipke, D.R., Yoon, E., and Wise, K.D. (2015). Tools for probing local circuits: high-density silicon probes combined with optogenetics. Neuron *86*, 92-105.

Chen, G., King, J.A., Burgess, N., and O'Keefe, J. (2013). How vision and movement combine in the hippocampal place code. Proceedings of the National Academy of Sciences of the United States of America *110*, 378-383.

Chen, G., Lu, Y., King, J.A., Cacucci, F., and Burgess, N. (2019). Differential influences of environment and self-motion on place and grid cell firing. Nature communications *10*, 630.

Diamanti, E.M., Reddy, C.B., Schroder, S., Muzzu, T., Harris, K.D., Saleem, A.B., and Carandini, M. (2021). Spatial modulation of visual responses arises in cortex with active navigation. eLife *10*.

Doeller, C.F., Barry, C., and Burgess, N. (2010). Evidence for grid cells in a human memory network. Nature *463*, 657-661.

Eichenbaum, H. (2014). Time cells in the hippocampus: a new dimension for mapping memories. Nature reviews Neuroscience *15*, 732-744.

Fiser, A., Mahringer, D., Oyibo, H.K., Petersen, A.V., Leinweber, M., and Keller, G.B. (2016). Experience-dependent spatial expectations in mouse visual cortex. Nature neuroscience *19*, 1658-1664.

Flossmann, T., and Rochefort, N.L. (2020). Spatial navigation signals in rodent visual cortex. Current opinion in neurobiology *67*, 163-173.

Fournier, J., Saleem, A.B., Diamanti, E.M., Wells, M.J., Harris, K.D., and Carandini, M. (2020). Mouse Visual Cortex Is Modulated by Distance Traveled and by Theta Oscillations. Current biology : CB *30*, 3811-3817 e3816.

Gofman, X., Tocker, G., Weiss, S., Boccara, C.N., Lu, L., Moser, M.B., Moser, E.I., Morris, G., and Derdikman, D. (2019). Dissociation between Postrhinal Cortex and Downstream Parahippocampal Regions in the Representation of Egocentric Boundaries. Current biology : CB *29*, 2751-2757 e2754.

Guitchounts, G., Lotter, W., Dapello, J., and Cox, D. (2020a). Stable 3D Head Direction Signals in the Primary Visual Cortex. bioRxiv.

Guitchounts, G., Masis, J., Wolff, S.B.E., and Cox, D. (2020b). Encoding of 3D Head Orienting Movements in the Primary Visual Cortex. Neuron *108*, 512-525 e514.

494 Hafting, T., Fyhn, M., Molden, S., Moser, M.B., and Moser, E.I. (2005). Microstructure of a spatial map in the entorhinal
495 cortex. Nature *436*, 801-806.
496 Haggerty, D.C., and Ji, D. (2015). Activities of visual cortical and hippocampal neurons co-fluctuate in freely moving rats
497 during spatial behavior. eLife *4*.
498 Hawkins, J., Lewis, M., Klukas, M., Purdy, S., and Ahmad, S. (2018). A Framework for Intelligence and Cortical Function
499 Based on Grid Cells in the Neocortex. Frontiers in neural circuits *12*, 121.
500 Hok, V., Jacob, P.-Y., Bordiga, P., Truchet, B., Poucet, B., and Save, E. (2018). A spatial code in the dorsal lateral geniculate
501 nucleus. bioRxiv, 473520.
502 Jankowski, M.M., and O'Mara, S.M. (2015). Dynamics of place, boundary and object encoding in rat anterior claustrum.
503 Front Behav Neurosci *9*, 250.
504 Jeffery, K.J., and O'Keefe, J.M. (1999). Learned interaction of visual and idiothetic cues in the control of place field
505 orientation. Experimental brain research *127*, 151-161.
506 Ji, D., and Wilson, M.A. (2007). Coordinated memory replay in the visual cortex and hippocampus during sleep. Nature
507 neuroscience *10*, 100-107.
508 Julian, J.B., Keinath, A.T., Frazzetta, G., and Epstein, R.A. (2018). Human entorhinal cortex represents visual space using a
509 boundary-anchored grid. Nature neuroscience *21*, 191-194.
510 Killian, N.J., Jutras, M.J., and Buffalo, E.A. (2012). A map of visual space in the primate entorhinal cortex. Nature *491*, 761-
511 764.
512 Killian, N.J., Potter, S.M., and Buffalo, E.A. (2015). Saccade direction encoding in the primate entorhinal cortex during
513 visual exploration. Proceedings of the National Academy of Sciences of the United States of America *112*, 15743-15748.
514 Koay, S.A., Thiberge, S., Brody, C.D., and Tank, D.W. (2020). Amplitude modulations of cortical sensory responses in
515 pulsatile evidence accumulation. eLife *9*.
516 LaChance, P.A., Todd, T.P., and Taube, J.S. (2019). A sense of space in postrhinal cortex. Science *365*.
517 Leinweber, M., Ward, D.R., Sobczak, J.M., Attinger, A., and Keller, G.B. (2017). A Sensorimotor Circuit in Mouse Cortex for
518 Visual Flow Predictions. Neuron *95*, 1420-1432 e1425.
519 Lever, C., Burton, S., Jeewajee, A., O'Keefe, J., and Burgess, N. (2009). Boundary vector cells in the subiculum of the
520 hippocampal formation. The Journal of neuroscience : the official journal of the Society for Neuroscience *29*, 9771-9777.
521 Long, X., and Zhang, S.J. (2021). A novel somatosensory spatial navigation system outside the hippocampal formation.
522 Cell research.
523 Lopez-Aranda, M.F., Lopez-Tellez, J.F., Navarro-Lobato, I., Masmudi-Martin, M., Gutierrez, A., and Khan, Z.U. (2009). Role
524 of layer 6 of V2 visual cortex in object-recognition memory. Science *325*, 87-89.
525 Mao, D., Kandler, S., McNaughton, B.L., and Bonin, V. (2017). Sparse orthogonal population representation of spatial
526 context in the retrosplenial cortex. Nature communications *8*, 243.
527 Mao, D., Neumann, A.R., Sun, J., Bonin, V., Mohajerani, M.H., and McNaughton, B.L. (2018). Hippocampus-dependent
528 emergence of spatial sequence coding in retrosplenial cortex. Proceedings of the National Academy of Sciences of the
529 United States of America *115*, 8015-8018.
530 Meyer, A.F., Poort, J., O'Keefe, J., Sahani, M., and Linden, J.F. (2018). A Head-Mounted Camera System Integrates Detailed
531 Behavioral Monitoring with Multichannel Electrophysiology in Freely Moving Mice. Neuron *100*, 46-60 e47.
532 Morris, R.G.M. (1981). Spatial localization does not require the presence of local cues. Learning and Motivation.
533 Muller, R.U., and Kubie, J.L. (1987). The effects of changes in the environment on the spatial firing of hippocampal
534 complex-spike cells. The Journal of neuroscience : the official journal of the Society for Neuroscience *7*, 1951-1968.
535 Nau, M., Navarro Schroder, T., Bellmund, J.L.S., and Doeller, C.F. (2018). Hexadirectional coding of visual space in human
536 entorhinal cortex. Nature neuroscience *21*, 188-190.
537 Nitz, D.A. (2006). Tracking route progression in the posterior parietal cortex. Neuron *49*, 747-756.

O'Keefe, J., and Dostrovsky, J. (1971). The hippocampus as a spatial map. Preliminary evidence from unit activity in the freely-moving rat. Brain research *34*, 171-175.

O'Mara, S.M., and Aggleton, J.P. (2019). Space and Memory (Far) Beyond the Hippocampus: Many Subcortical Structures Also Support Cognitive Mapping and Mnemonic Processing. Frontiers in neural circuits *13*, 52.

Olsen, G.M., Ohara, S., Iijima, T., and Witter, M.P. (2017). Parahippocampal and retrosplenial connections of rat posterior parietal cortex. Hippocampus *27*, 335-358.

Pakan, J.M., Francioni, V., and Rochefort, N.L. (2018). Action and learning shape the activity of neuronal circuits in the visual cortex. Current opinion in neurobiology *52*, 88-97.

Rao, R.P., and Ballard, D.H. (1999). Predictive coding in the visual cortex: a functional interpretation of some extra-classical receptive-field effects. Nature neuroscience *2*, 79-87.

Ravassard, P., Kees, A., Willers, B., Ho, D., Aharoni, D.A., Cushman, J., Aghajan, Z.M., and Mehta, M.R. (2013). Multisensory control of hippocampal spatiotemporal selectivity. Science *340*, 1342-1346.

Rolls, E.T., and O'Mara, S.M. (1995). View-responsive neurons in the primate hippocampal complex. Hippocampus *5*, 409-424.

Saleem, A.B. (2020). Two stream hypothesis of visual processing for navigation in mouse. Current opinion in neurobiology *64*, 70-78.

Saleem, A.B., Ayaz, A., Jeffery, K.J., Harris, K.D., and Carandini, M. (2013). Integration of visual motion and locomotion in mouse visual cortex. Nature neuroscience *16*, 1864-1869.

Saleem, A.B., Diamanti, E.M., Fournier, J., Harris, K.D., and Carandini, M. (2018). Coherent encoding of subjective spatial position in visual cortex and hippocampus. Nature *562*, 124-127.

Sargolini, F., Fyhn, M., Hafting, T., McNaughton, B.L., Witter, M.P., Moser, M.B., and Moser, E.I. (2006). Conjunctive representation of position, direction, and velocity in entorhinal cortex. Science *312*, 758-762.

Save, E., and Poucet, B. (2009). Role of the parietal cortex in long-term representation of spatial information in the rat. Neurobiology of learning and memory *91*, 172-178.

Siegle, J.H., Jia, X., Durand, S., Gale, S., Bennett, C., Graddis, N., Heller, G., Ramirez, T.K., Choi, H., Luviano, J.A., *et al.* (2021). Survey of spiking in the mouse visual system reveals functional hierarchy. Nature.

Smith, S.P., and Jain, A.K. (1984). Testing for uniformity in multidimensional data. IEEE transactions on pattern analysis and machine intelligence *6*, 73-81.

Solstad, T., Boccara, C.N., Kropff, E., Moser, M.B., and Moser, E.I. (2008). Representation of geometric borders in the entorhinal cortex. Science *322*, 1865-1868.

Stachenfeld, K.L., Botvinick, M.M., and Gershman, S.J. (2017). The hippocampus as a predictive map. Nature neuroscience *20*, 1643-1653.

Steinmetz, N.A., Zatka-Haas, P., Carandini, M., and Harris, K.D. (2019). Distributed coding of choice, action and engagement across the mouse brain. Nature *576*, 266-273.

Stensola, T., Stensola, H., Moser, M.B., and Moser, E.I. (2015). Shearing-induced asymmetry in entorhinal grid cells. Nature *518*, 207-212.

Taube, J.S. (1995). Head direction cells recorded in the anterior thalamic nuclei of freely moving rats. The Journal of neuroscience : the official journal of the Society for Neuroscience *15*, 70-86.

Taube, J.S. (2007). The head direction signal: origins and sensory-motor integration. Annual review of neuroscience *30*, 181-207.

Taube, J.S., Muller, R.U., and Ranck, J.B., Jr. (1990). Head-direction cells recorded from the postsubiculum in freely moving rats. I. Description and quantitative analysis. The Journal of neuroscience : the official journal of the Society for Neuroscience *10*, 420-435.

van Strien, N.M., Cappaert, N.L., and Witter, M.P. (2009). The anatomy of memory: an interactive overview of the

582 parahippocampal-hippocampal network. Nature reviews Neuroscience *10*, 272-282.
583 van Wijngaarden, J.B., Babl, S.S., and Ito, H.T. (2020). Entorhinal-retrosplenial circuits for allocentric-egocentric
584 transformation of boundary coding. eLife *9*.
585 Vantomme, G., Rovo, Z., Cardis, R., Beard, E., Katsioudi, G., Guadagno, A., Perrenoud, V., Fernandez, L.M.J., and Luthi, A.
586 (2020). A Thalamic Reticular Circuit for Head Direction Cell Tuning and Spatial Navigation. Cell reports *31*, 107747.
587 Velez-Fort, M., Bracey, E.F., Keshavarzi, S., Rousseau, C.V., Cossell, L., Lenzi, S.C., Strom, M., and Margrie, T.W. (2018). A
588 Circuit for Integration of Head- and Visual-Motion Signals in Layer 6 of Mouse Primary Visual Cortex. Neuron *98*, 179-191
589 e176.
590 Wang, C., Chen, X., and Knierim, J.J. (2020). Egocentric and allocentric representations of space in the rodent brain.
591 Current opinion in neurobiology *60*, 12-20.
592 Whitlock, J.R., Pfuhl, G., Dagslott, N., Moser, M.B., and Moser, E.I. (2012). Functional split between parietal and entorhinal
593 cortices in the rat. Neuron *73*, 789-802.
594 Wilber, A.A., Clark, B.J., Forster, T.C., Tatsuno, M., and McNaughton, B.L. (2014). Interaction of egocentric and world-
595 centered reference frames in the rat posterior parietal cortex. The Journal of neuroscience : the official journal of the
596 Society for Neuroscience *34*, 5431-5446.
597 Zhang, S.J., Ye, J., Miao, C., Tsao, A., Cerniauskas, I., Ledergerber, D., Moser, M.B., and Moser, E.I. (2013). Optogenetic
598 dissection of entorhinal-hippocampal functional connectivity. Science *340*, 1232627.

Materials and Methods

Long-Evans Rats

The recording experiments were performed on six male Long-Evans adult rats (2-4 months) weighting 250-450 grams on the day for chronic surgery. Rats were individually housed in transparent plastic cages (W × L × H: 35 cm × 45 cm × 45 cm) and kept on a 12-hour reversed light/dark schedule (lights on from 21:00 p.m. to 09:00 hours). All behavioral trials were performed during the dark phase. Rats were maintained in a temperature-controlled (19-23°C) and humidity-adjusted (55-70%) vivarium. Rats were partially food-deprived to about 85-90% of free-feeding body weight. Food restriction was imposed 8-24 hours before each training and recording trial. Water was supplied *ad libitum*. All animal experiments were performed in accordance with the National Animal Welfare Act under a protocol with the permission license number #SYXK-2017002 approved by the Animal Care and Use Committee from both the Army Medical University and Xinqiao Hospital.

Surgical procedures and tetrode placement

The rats were anesthetized with isoflurane mixed with oxygen (1.5-3.0% in O_2), immobilized in a stereotaxic frame (David Kopf Instruments, Tujunga, California, USA) and kept on feedback-adjusted temperature control pad at 37ºC. A self-assembled microdrive loaded with four tetrodes were implanted to target the mediolateral (V2ML) and mediomedial (V2MM) regions of the second primary cortex with the stereotaxic coordinate centered at ~2.6 mm lateral to the midline (ML), ~−4.7 mm anterior-posterior (AP) from bregma, 0.4-1.1 mm dorsal-ventral (DV) below the dura and at an angle of 10° from the medial-to-lateral direction in the coronal plane, secured with dental cement with 8-10 anchor screws. A screw served as the ground electrode. Tetrodes were assembled with four 17 μm polyimide-coated platinum-iridium (90-10%) wires (#100167, California Fine Wire Company). Tetrodes were plated with a 1.5% platinum solution to reduce their impedances between 150 and 300 kΩ at 1 kHz through electroplating prior to surgery (nanoZ; White Matter LLC, Seattle, Washington, USA). 8-10 jeweler screws were threaded into the rat skull, and individual microdrives were anchored to screws with several rounds of application of the dental cement.

Behavioral protocol and data collection

The chronically implanted rats were allowed at least one week of recovery before behavioral training, tetrode turning and data recording were initiated. Rats were trained to forage around in a 1 × 1 m^2 square box with a white cue card (297 × 210 mm^2) mounted on one side of the interior wall. Food pellets were randomly dispersed into the enclosure intermittently to encourage free exploration.

Each recording trial lasted typically between 20 and 40 min to facilitate full coverage of the testing enclosure. Tetrodes were lowered very slowly in steps of 25 or 50 μm daily until well-separated single units can be identified. Data were acquired by an Axona system (Axona Ltd., St. Albans, U.K.) at 48 kHz, band-passed between 0.8-6.7 kHz and a gain of x5-18k. Spikes were digitized with 50 8-bit sample windows. Local field potentials were recorded from one of the electrodes with a low-pass filter (cut-off: 500 Hz).

Spike sorting, cell-type identification and locational firing rate map

To identify well-isolated units, spike sorting was manually performed offline with graphical cluster-cutting software (TINT, version 4.4.16, Axona Ltd, St. Albans, U.K.), and the clustering was primarily based on features of the spike waveform (peak-to-trough amplitude and spike width), together with additional autocorrelations and cross-correlations separation tools. During the manual cluster cutting, we strictly counted units with similar or identical waveform shapes only once whenever similar or identical individual units were recorded and tracked across two consecutive recording sessions. Only recording sessions in which rats covered more than 80% of the running environment were taken for further analysis. To assess the quality of cluster separation, we calculated the well-established metric (L_{ratio}) that measures the isolation distance between clusters (Schmitzer-Torbert et al., 2005).

Two small light-emitting diodes (LEDs) were mounted to the headstage to track the rats' speed, position and orientation via an overhead video camera. Only spikes recorded during animal's instantaneous running speeds > 2.5 cm/s were chosen for further analysis in order to exclude confounding behaviors such as immobility, grooming and rearing.

To classify firing fields and firing rate distributions, the position data were divided into 2.5 × 2.5 cm^2 bins, and the path was smoothed with a 21-sample boxcar window filter (400 ms; 10 samples on each side). Units with > 100 spikes per session and with a coverage of >80% were included for further analyses. Maps for spike numbers and spike times were smoothed with a quasi-Gaussian kernel over the neighboring 5 × 5 bins. Spatial firing rates were calculated by dividing the smoothed map of spike numbers with spike times. The peak firing rate was defined as the highest rate in the corresponding bin within the spatial firing rate map. Mean firing rates were averaged from the whole session data. The criterion for classifying a V2 unit as a spatially tuned cell (e.g., place cell, head-direction cell, border cell or grid cell) was determined by measuring whether the corresponding score was greater than the 99^{th} percentile value of the shuffled data.

Identification of place cells

Spatial information (SI) is a quantification of the extent to which a unit's firing pattern can predict the position of freely moving animals and is expressed in the unit of bits per spike:

$$\mathrm{SI} = \sum_i p_i \frac{\lambda_i}{\lambda} \log_2 \frac{\lambda_i}{\lambda}$$

where λ_i is the mean firing rate of the unit in the *i*-th bin, λ is the overall mean firing rate of the unit in the trial, and p_i is the probability for the animal being at the location of the *i*-th bin. Adaptive smoothing was applied to optimize the trade-off between spatial resolution and sampling error before the SI calculation. The data were first divided into 2.5 × 2.5-cm^2 bins, and then the firing rate within each bin was calculated by expanding a circle centered on the bin until

$$\gamma \geq \frac{\alpha}{n\sqrt{s}}$$

where γ is the circle's radius in bins, *n* is the number of occupancy of samples within the circle, *s* is the total number of spikes fired within the circle, and α =10000 is a constant. With a position sampling frequency at 50 Hz, the firing rate assigned to that bin was then set to $50 \cdot s/n$.

673 A V2 unit was classified as a place cell if its SI was above the chance level, which was computed by a
674 random permutation process using all recorded cells. For each round of the shuffling process, the entire
675 sequence of spike trains from each unit was time-shifted along the animal's trajectory by a random
676 period between 20 s after the trial onset and the trial duration minus 20 s, with the end wrapped to the
677 beginning of the trial. A spatial firing rate map was then constructed, and spatial information was
678 calculated. This shuffling process was repeated 100 times for each unit, generating a total of 136,400
679 permutations for the 1364 V2 units. This shuffling procedure was aimed to preserve the temporal firing
680 characteristics in the unshuffled data while disrupting the spatial structure at the same time. The SI
681 score was then measured for each shuffled rate map. The distribution of SI scores across all 100
682 permutations of all units was computed, from which the 99th percentile of the significant level was
683 determined. To determine the threshold for categorizing a V2 unit as a place cell, we chose the SI score
684 above the 99th percentile of the distribution from shuffled populations. In addition to population
685 shuffling, within-unit shuffling was performed within the entire sequence of spike trains from each
686 individual unit, and the shuffling process was repeated 100 times for each single unit.

687 Spatial sparsity was used to measure how compact and selective the place field is relative to the
688 recording enclosure. The spatial sparsity was calculated using the formula as follows:

689 $$\text{Sparsity} = \frac{(\sum p_i \lambda_i)^2}{\sum p_i {\lambda_i}^2}$$

690 where p_i is the occupancy probability for the animal being at the location of the i-th bin in the map
691 and λ_i is the mean firing rate of the cell in bin i.

692 Spatial coherence was estimated by calculating the mean correlation between the firing rate of each
693 bin in the map and the aggregate firing rate of the eight nearest bins. We used the unsmoothed firing
694 rate maps for computing the spatial coherence.

695 The spatial correlation across trials from the same recording arena was computed for each cell by
696 correlating the firing rates in corresponding paired bins of two smoothed rate maps. The spatial stability
697 within trials was estimated by calculating spatial correlations between firing rate maps generated from

the first and second halves of the same trial. Place cells with spatial stability lower than 0.3 were excluded for further analysis.

Identification of grid cells

Gridness score (GS) was previously established to quantify the grid cell (Boccara et al., 2010; Hafting et al., 2005; Zhang et al., 2013). We calculated the spatial autocorrelation with smoothed rate maps. The unbiased autocorrelograms were derived from Pearson's product-moment correlation coefficient correcting for edge effects and unvisited locations.

Let $\lambda(x,y)$ denote the unit's mean firing rate at a two-dimensional Cartesian coordinate (x,y), the autocorrelation of the spatial firing field was calculated as:

$$r(\tau_x,\tau_y)=\frac{\mathrm{n}\sum\lambda(x,y)\,\lambda\left(x-\tau_x,y-\tau_y\right)-\sum\lambda(x,y)\sum\lambda\left(x-\tau_x,y-\tau_y\right)}{\sqrt{n\sum\lambda(x,y)^2-[\sum\lambda(x,y)]^2}\sqrt{n\sum\lambda\left(x-\tau_x,y-\tau_y\right)^2-[\sum\lambda\left(x-\tau_x,y-\tau_y\right)]^2}}$$

where the summation was over *n* pixels for both $\lambda(x,y)$ and $\lambda\left(x-\tau_x,y-\tau_y\right)$ (τ_x and τ_y denote the spatial lags). Autocorrelations were not calculated for spatial lags of $\tau_x,\ \tau_y$ where $n < 20$.

The degree of spatial regularity ("gridness" or GS) was calculated for each unit by using a circular sample centered on the central peak of the autocorrelogram but excluding the central peak itself, and by comparing rotated versions of this circular sample. Pearson's correlations between this circular sample and its rotated versions were calculated, with the angles of rotation of 60° and 120° in the first group, and 30°, 90° and 150° in the second group. A unit's GS was defined as the minimal difference between any of the coefficients in the first group and any of the coefficients in the second group. Shuffling was performed in the same procedure used for defining place cells. Grid cells were defined if their rotational symmetry-based GSs exceeded the 99th percentile of the distribution of GS derived from the shuffled data.

Grid spacing was computed as the median distance from the grid center to the closest peak among six neighboring firing fields in the autocorrelogram of spatial firing map. Since this analysis might be

721 sensitive to noise in the grid autocorrelogram, grid spacing was computed only when the median
722 distance to the six neighboring peaks for the analyzed unit was comparable to the radius of the circle
723 centered on the gird autocorrelogram with the highest GS. The radius of this circle around the center
724 of autocorrelogram was also referred to as the grid field size.

725 Grid orientation was calculated by first computing vectors from the center of the autocorrelogram
726 to each of the three adjacent peaks among six neighboring firing fields in the autocorrelogram of
727 spatial firing map in the counterclockwise direction, beginning with a camera-based reference line
728 of zero degree. The angle between the minimal orientation of those three vectors and the camera-
729 based reference line was defined as the grid orientation.

730 Identification of head-direction cells

731 The calculation of mean vector length (MVL) was followed by previous publication (Boccara et al.,
732 2010; Sargolini et al., 2006; Zhang et al., 2013). The rat's head-direction was computed by the relative
733 position of two LEDs differentiated through their sizes. The directional tuning curve for each recorded
734 unit was drawn by plotting the firing rate as a function of the rat's head angle, which is divided into
735 bins of 3° and then smoothed with a 14.5° mean window filter (2 bins on each side). To avoid potential
736 biases, data were only used if all head angle bins contained nonzero values.

737 The strength of directionality was measured by computing the MVL from circular distributed firing
738 rates. The chance value was determined by a shuffling process simulated in the same way as for place
739 cells, with the entire sequence of spike trains time-shifted between 20 s and the whole trail length
740 minus 20 s along the animal's trajectory. A V2 unit was defined as a head direction cell if its mean
741 vector length was larger than the 99^{th} percentile of MVLs in the shuffled distribution. Angular stability
742 was computed by calculating the correlation of firing rates across directional bins generated from the
743 first and second halves of the same trial. Head direction cells with angular stability lower than 0.3 were
744 excluded for further analysis.

745 Identification of border cells

746 The calculation of the border score (BS) was followed by previously literature (Boccara et al., 2010;

Solstad et al., 2008; Zhang et al., 2013). Border or boundary vector cells were identified by calculating the border score, or the difference between the maximal length of any of the four walls touching on any single spatial firing field of the cell and the average distance of the firing field to the nearest wall, divided by the sum of those two values. The BS ranged from −1 for cells with perfect central firing fields to +1 for cells with firing fields that exactly line up with at least one entire wall. Firing fields were defined as summation of neighboring pixels with total firing rates higher than 0.3 times the unit's maximum firing rate that covered a total area of at least 200 cm^2.

Border cell classification was verified in the same way as for place cells, grid cells, and head direction cells. For each permutation trial, the whole sequence of spike trains was time-shifted along the animal's trajectory by a random period between 20 s and 20 s less than the length of the entire trial, with the end wrapped to the start of the trial. A spatial firing rate map was then obtained, followed by BS estimation.

The distribution of BS was calculated for the entire set of permutation trials from all recorded units, from which the threshold with the 99^{th} percentile was determined. A V2 unit was defined as a border cell if its BS was higher than the 99^{th} percentile threshold derived from the shuffled data.

Correction procedure for inhomogeneous sampling

To assess the inhomogeneous sampling bias on the spatial firing properties of V2 place cells and head-direction cells, we applied a maximum-likelihood correction procedure (originally proposed by Burgess and colleagues, and codes generously shared by the authors) (Burgess et al., 2005). Briefly, the position data were sorted into 2.5×2.5 cm^2 bins and directional date into 120 bins of 3^o each before applying the correction algorithm. The field plot was applied with 5 boxcar × 5 boxcar smoothing, and polar plot was applied with 5 boxcar smoothing for the purpose of visualization.

Environmental manipulations

For visual landmark rotation, we first recorded V2 unit activity in the standard recording session followed by a 90° cue-card rotation in the clockwise or counterclockwise orientation. Next, another standard session was performed with the cue-card rotated back to the original position. For recording

in the elevated platform without walls, we first recorded V2 units in the square box, followed by the recording in the elevated platform without walls. Finally, the animal returned to the original square box for another recording session. For the recording of border cells in the presence of inserted wall, we first identified V2 border cells in the square box. Then the recording session was followed by the insertion of a wall along the center of the external wall. Another recording session was performed after removing the inserted wall. For food/no food comparisons, we recorded V2 units in two consecutive recording sessions without and with throwing food pellets into the running enclosure.

Histology and electrode track location

After completion of the final recording sessions, implanted rats were deeply anaesthetized with sodium pentobarbital (0.01ml/g) and perfused transcardially with ice-cold 1 x phosphate-buffered saline (PBS) followed by 4% ice-cold paraformaldehyde (PFA) in 1 x PBS. Brains were removed and post-fixed in 4% PFA in 1 x PBS at 4^{o}C overnight. The brain was then transferred into 10, 20 and 30% sucrose/PFA solution sequentially across 72 hours before sectioning by using a cyrostat. Thirty-micron-thick coronal sections were serially cut and obtained through the implanted brain area. Sections were mounted on glass slides and stained with Cresyl Violet (Sigma-Aldrich). The final recording positions were imaged and determined from digitized images of the Nissl-stained sections scanned on the Olympus Slideview VS200 Digital Slide Scanner. Positions of each individual recordings were estimated from the deepest tetrode track according to the daily notebook on tetrode advancement. The tissue shrinkage correction was calculated by dividing the distance between the brain surface and electrode tips by the final advanced depth of the recording electrodes. Electrode traces were confirmed to be located between the mediolateral part of the secondary visual cortex (V2ML) and mediomedial part of the secondary visual cortex (V2MM) from five implanted rats based on the reference figures (from Figure 68 to 73) published in the sixth edition of *The Rat Brain in Stereotaxic Coordinates* (Paxinos and Watson, 2007).

Data availability: Recording dataset will become available in a forthcoming public domain, and reasonable request into acquiring the raw data beforehand should be directed to the corresponding author.

Code availability: The source codes used in this study are available from the corresponding author upon reasonable request.

Acknowledgments: We thank Hao Wu, Wan-Neng Tang, Jia-Shun Ren, Cai-Ping Song, De-Guang Qi, Tong-Quan Liao, Hao Chen, Qian Chen, Yang Yang, Hui Yang and Sheng-Qing Lv for their encouragement and support. We thank Edvard Moser, May-Britt Moser, Neil Burgess and Caswell Barry for sharing their analytical codes with us. Special thanks to Ting-Ting Huang, Mi Zhang and A-Xiang Zhou for their technical assistance. S.-J.Z. was supported by the National Natural Science Foundation of China (Grant# 31872775). X.L. is supported by the Chongqing Municipality postdoctoral fellowship (Grant# cstc2019jcyj-bshX0035). Z.S.C. is partly supported by the US National Institutes of Health (R01-MH118928).

Author contributions: S.-J.Z. conceived the project. X.L. and S.-J.Z. designed the study, performed the surgery and analyzed the data. J.C., B.D. and X.L. conducted the experiments and acquired the recordings. Z.S.C. and B.D. provided the feedback. X.L. developed the codes and made the figures. Z.S.C., X.L. and S.-J.Z. wrote the manuscript.

Additional information

Supplementary information (Supplementary **Figs. S1-S28**) accompanies this paper.

Competing interests: The authors declare no competing interests.

Supplementary references

Boccara, C.N., Sargolini, F., Thoresen, V.H., Solstad, T., Witter, M.P., Moser, E.I., and Moser, M.B. (2010). Grid cells in pre- and parasubiculum. Nature neuroscience *13*, 987-994.

Burgess, N., Cacucci, F., Lever, C., and O'Keefe, J. (2005). Characterizing multiple independent behavioral correlates of cell firing in freely moving animals. Hippocampus *15*, 149-153.

Hafting, T., Fyhn, M., Molden, S., Moser, M.B., and Moser, E.I. (2005). Microstructure of a spatial map in the entorhinal cortex. Nature *436*, 801-806.

Paxinos, G., and Watson, C. (2007). The rat brain in stereotaxic coordinates, Vol 552 (Amsterdam: Elsevier).

Sargolini, F., Fyhn, M., Hafting, T., McNaughton, B.L., Witter, M.P., Moser, M.B., and Moser, E.I. (2006). Conjunctive representation of position, direction, and velocity in entorhinal cortex. Science *312*, 758-762.

Schmitzer-Torbert, N., Jackson, J., Henze, D., Harris, K., and Redish, A.D. (2005). Quantitative measures of cluster quality for use in extracellular recordings. Neuroscience *131*, 1-11.

Solstad, T., Boccara, C.N., Kropff, E., Moser, M.B., and Moser, E.I. (2008). Representation of geometric borders in the

entorhinal cortex. Science *322*, 1865-1868.

Zhang, S.J., Ye, J., Miao, C., Tsao, A., Cerniauskas, I., Ledergerber, D., Moser, M.B., and Moser, E.I. (2013). Optogenetic dissection of entorhinal-hippocampal functional connectivity. Science *340*, 1232627.

Supplementary Materials

A compact spatial map in V2 visual cortex

Xiaoyang Long[1*], Bin Deng[1*], Jing Cai[1], Zhe Sage Chen[2] & Sheng-Jia Zhang[1#]

1. Department of Neurosurgery, Xinqiao Hospital, Army Medical University, Chongqing 400037, China

2. Department of Psychiatry, Department of Neuroscience & Physiology, Neuroscience Institute, New York University School of Medicine, New York, NY 10016, USA

*These authors contributed equally to this work.

#To whom correspondence should be addressed.

Supplementary Fig. S1-S28

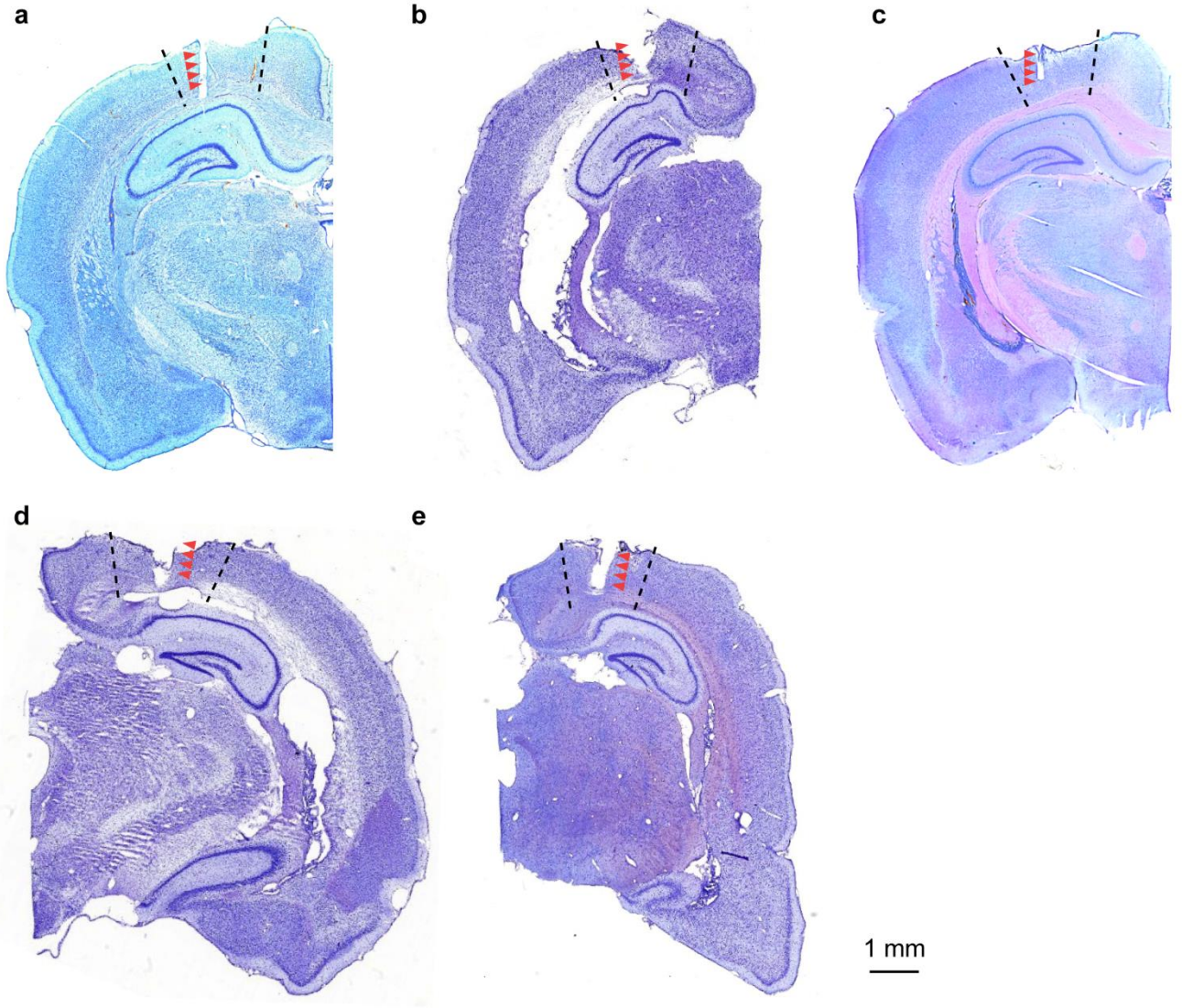

Fig. S1. Tetrode recording sites in the rat secondary visual cortex (V2). a-e, Cresyl violet-stained coronal brain sections showing the electrode track and recording locations (red arrows) in V2 from five rats. Dashed lines indicate the boundaries of V2.

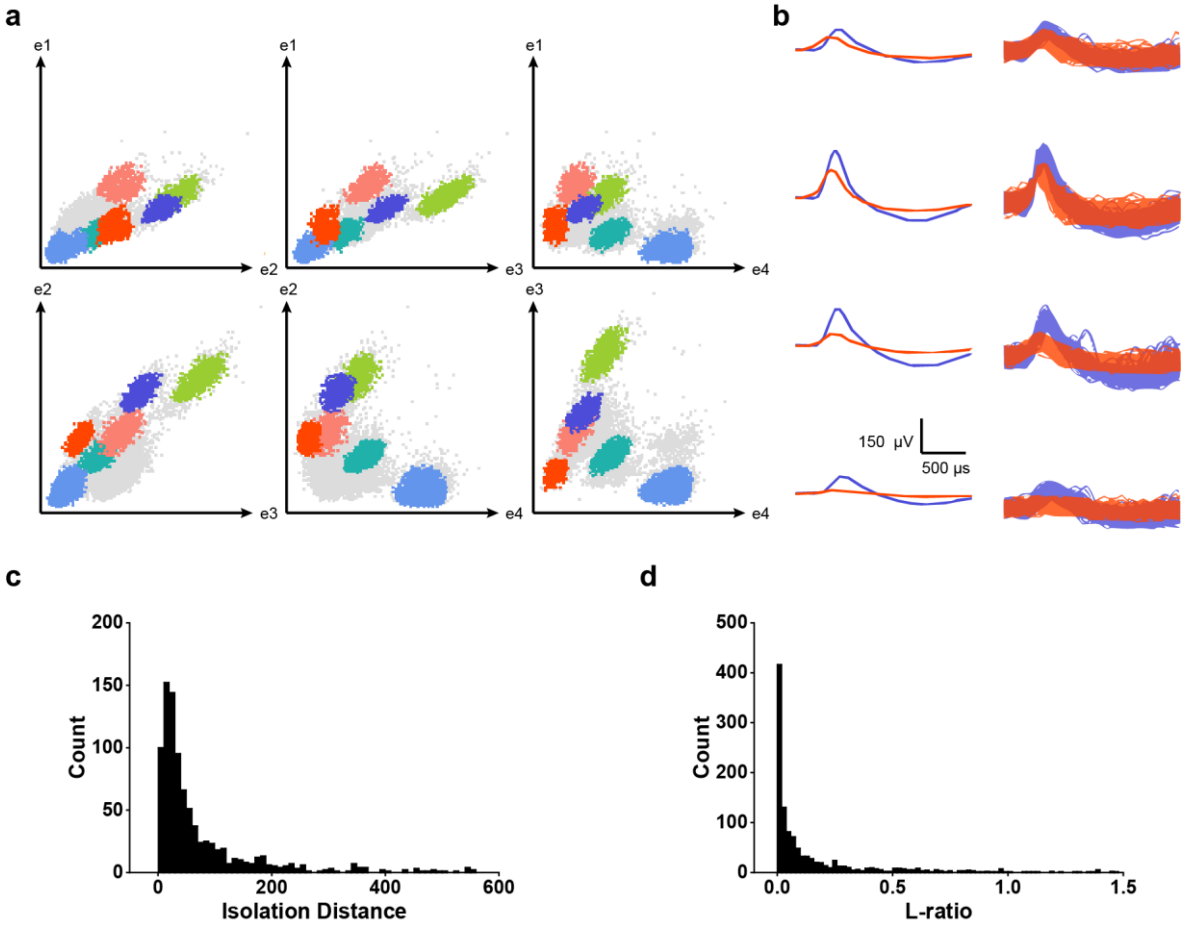

Fig. S2. Cluster diagrams and isolation quality of spikes recorded from V2. a, Scatterplots showing the distribution of the peak-to-trough amplitudes for all spikes recorded in four electrodes of the same tetrode. **b**, Overlaid waveforms from two well-separated red and cyan-blue clusters in the corresponding scatterplot. **c-d**, Isolation Distance and L-ratio for recorded V2 units, respectively.

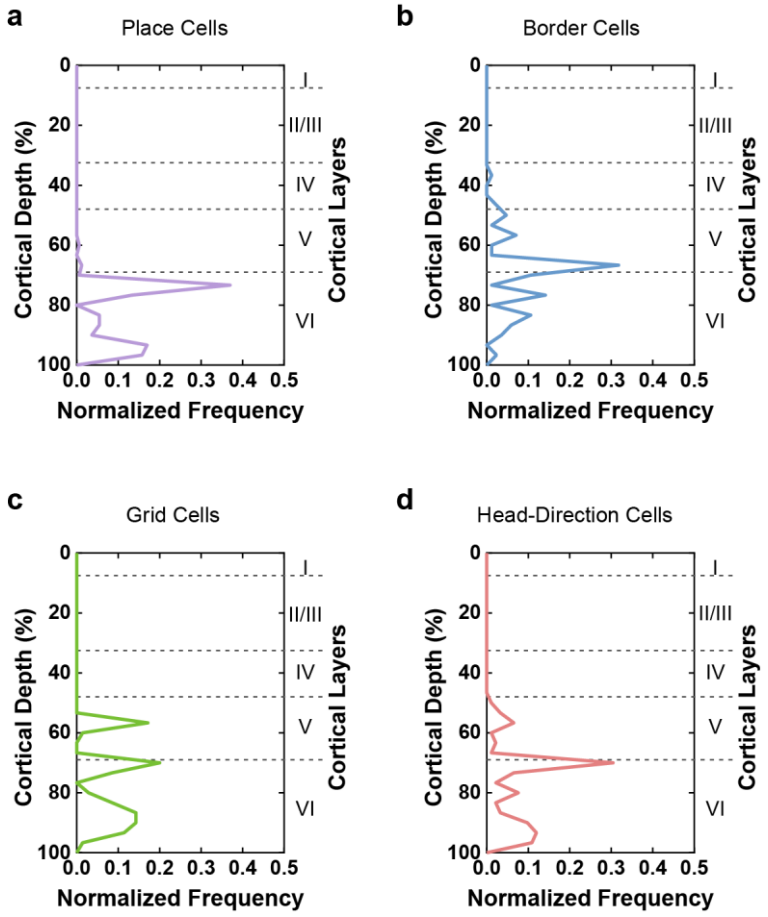

Fig. S3. Layer distribution of four distinct V2 spatially tuned cell types. a-d, Normalized layer distributions of place cells, border cells, grid cells and head-direction cells in the rat V2, respectively. Note the near absence of recording in the superficial layer I-III.

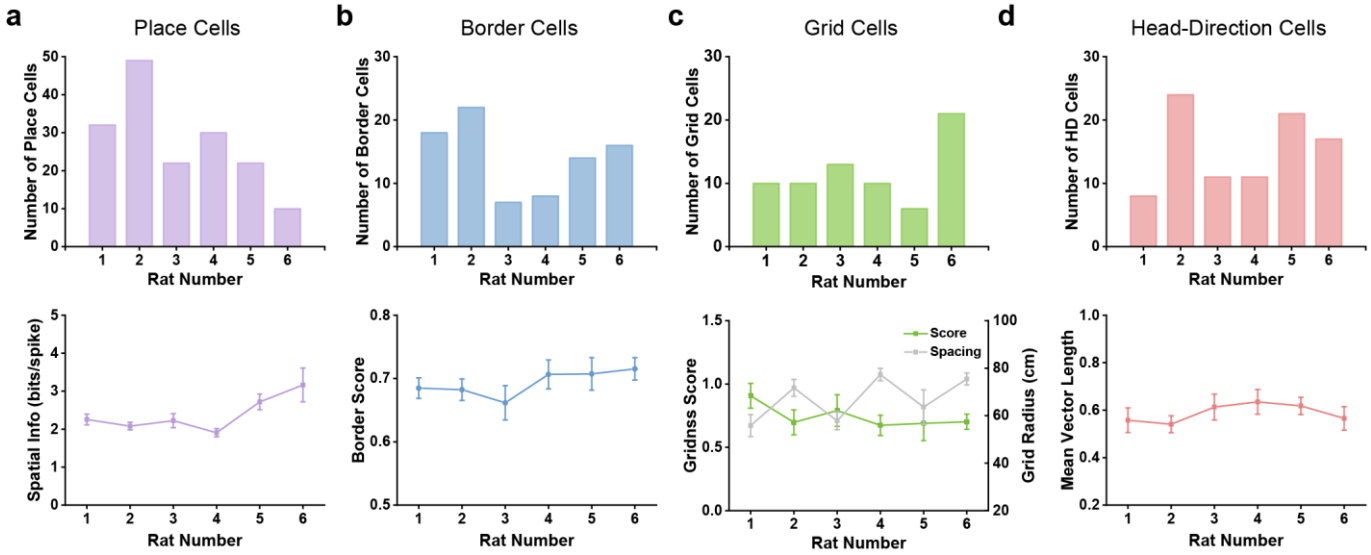

855

856 **Fig. S4. Spatial characterizations of recorded spatially tuned V2 units across six rats. a-d**, Number of
857 four different spatial cell types recorded in each rat (upper panels) and five spatial properties (spatial
858 information, border score, gridness score, grid radius, and mean vector length) across different rats (bottom
859 panels).

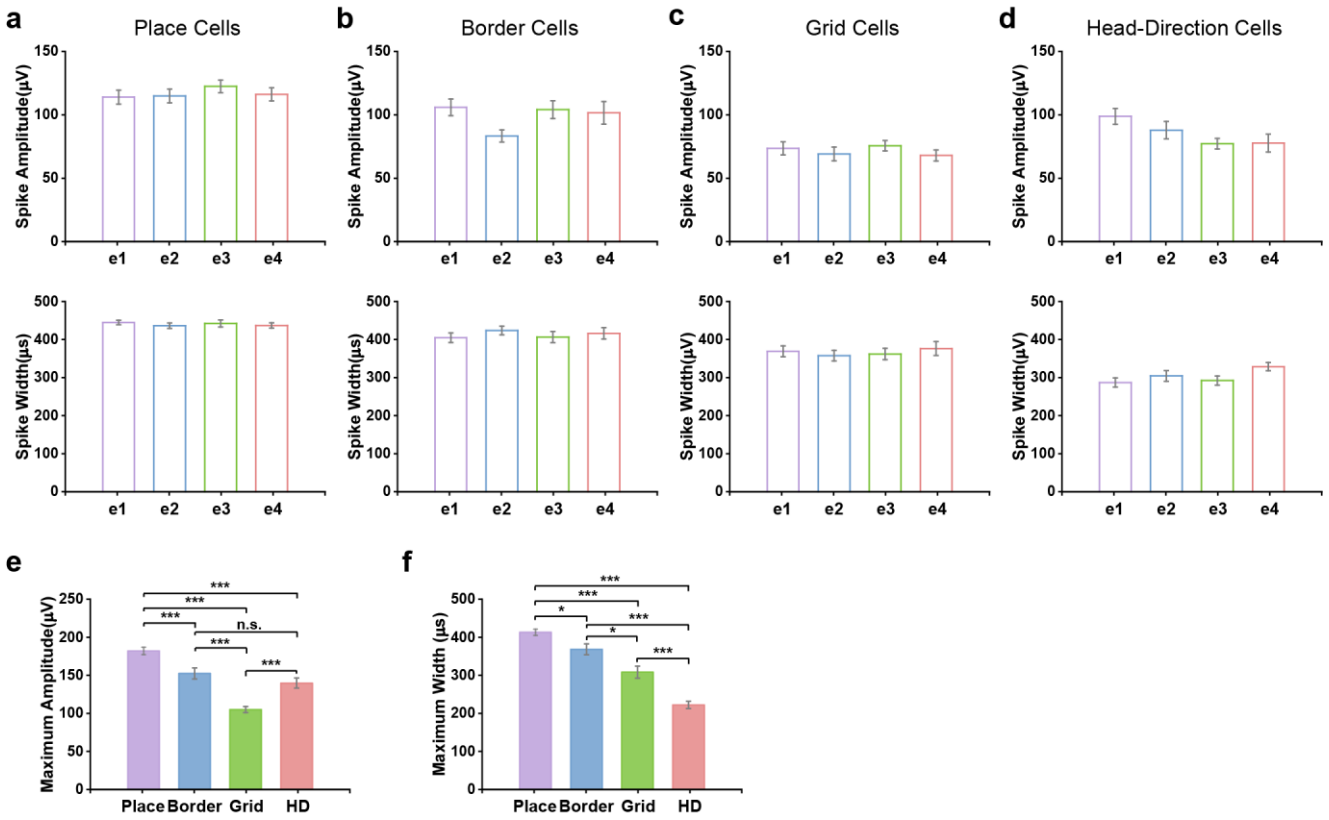

Fig. S5. Distribution of spike amplitudes and spike widths for four types of V2 spatially tuned units. a-d, Peak-to-peak amplitudes (upper panels) and peak-to-trough widths (bottom panels) of spike waveforms on four electrodes (e1-e4) of the same tetrode for identified V2 place cells, border cells, grid cells and head-direction cells, respectively. **e-f,** Comparison of the highest amplitude on four electrodes and corresponding spike width for four distinct V2 spatially tuned cell types (n = 165, 85, 70 and 92, respectively, unpaired t-test, n.s., P>0.05; *, P<0.05; **, P<0.01; ***, P<0.001).

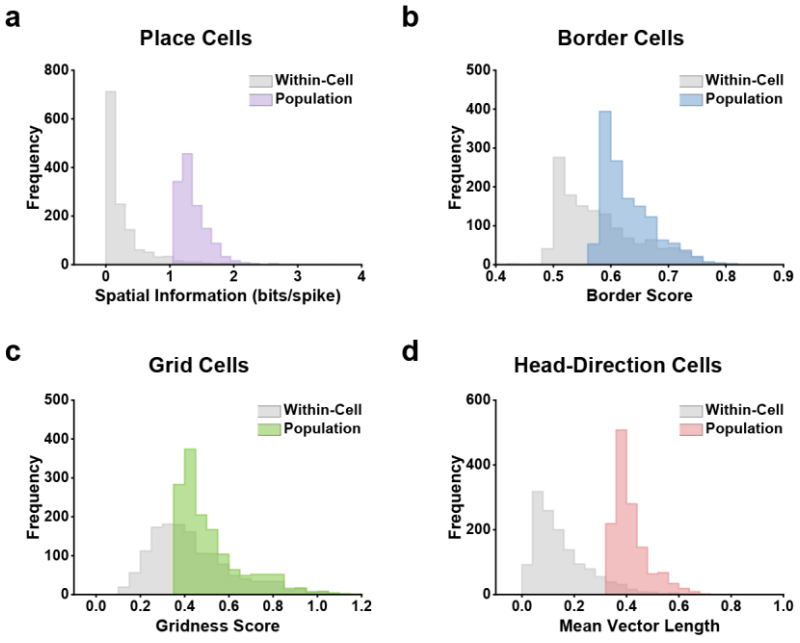

Fig. S6. Comparison of threshold statistics determined by population shuffling and within-cell shuffling. **a-d,** Histograms showing the 99th significance level of each randomly shuffled distribution by population shuffling and within-cell shuffling to calculate the spatial information, border score, gridness score and mean vector length for all identified V2 units, respectively.

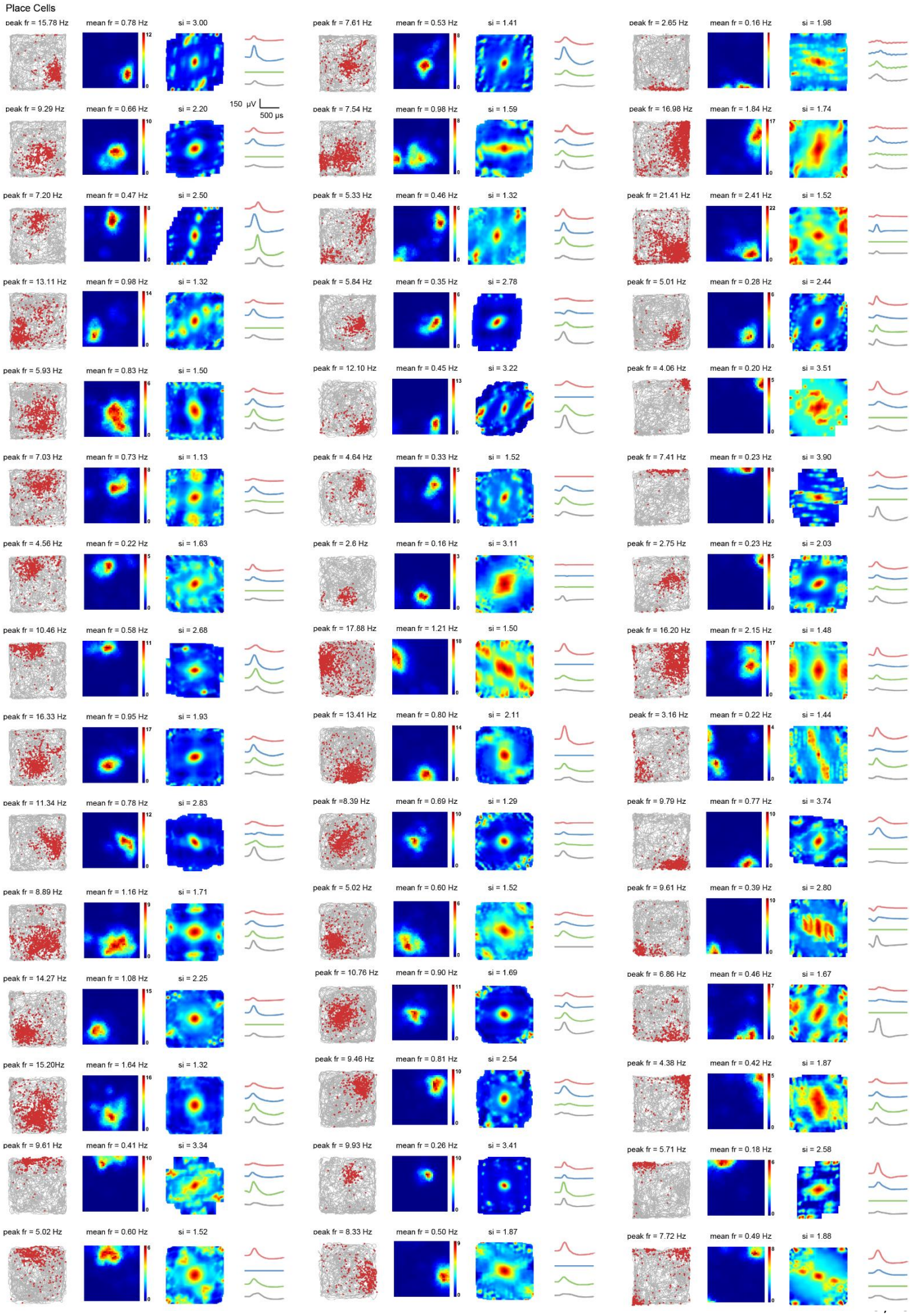

873

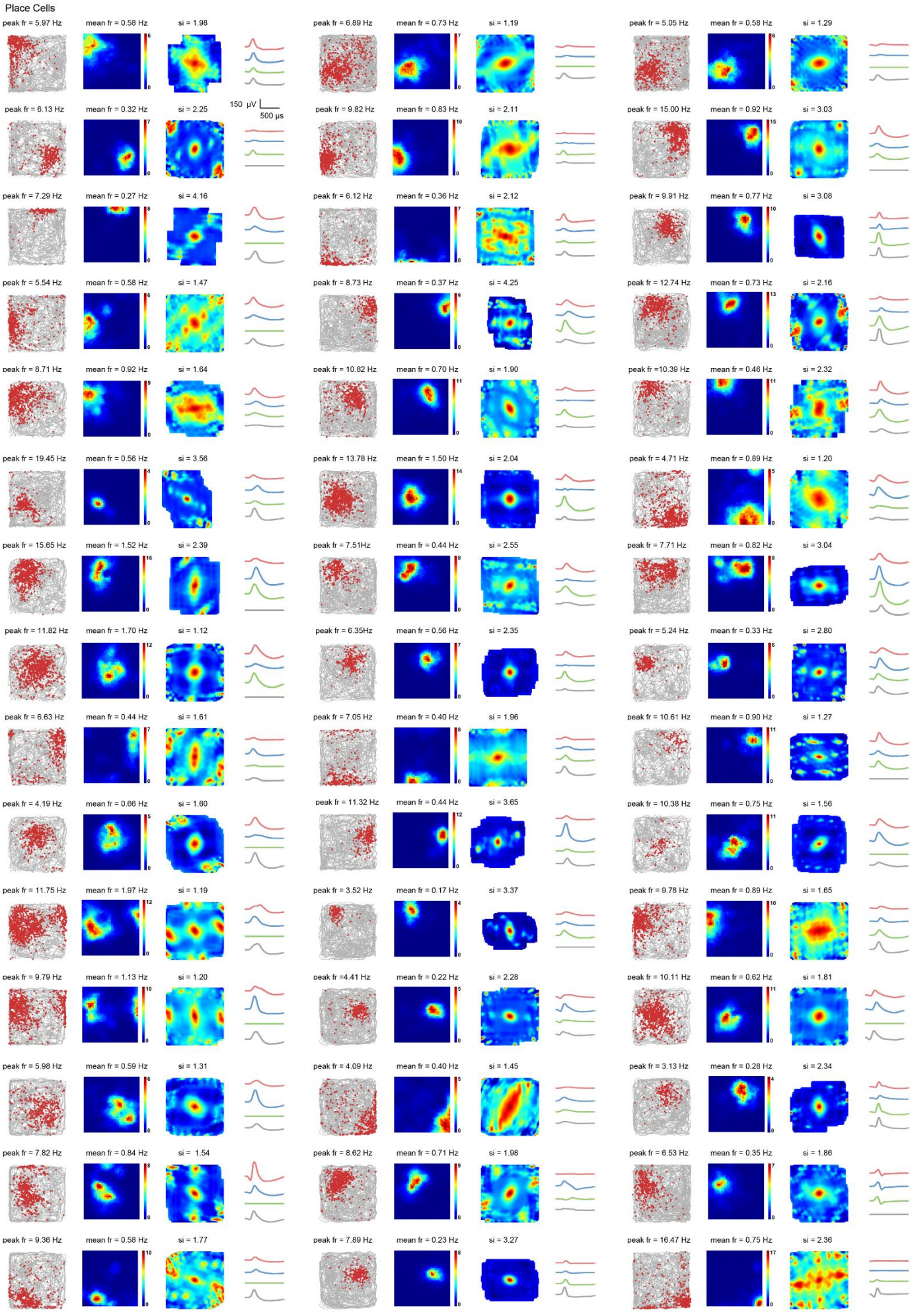

874

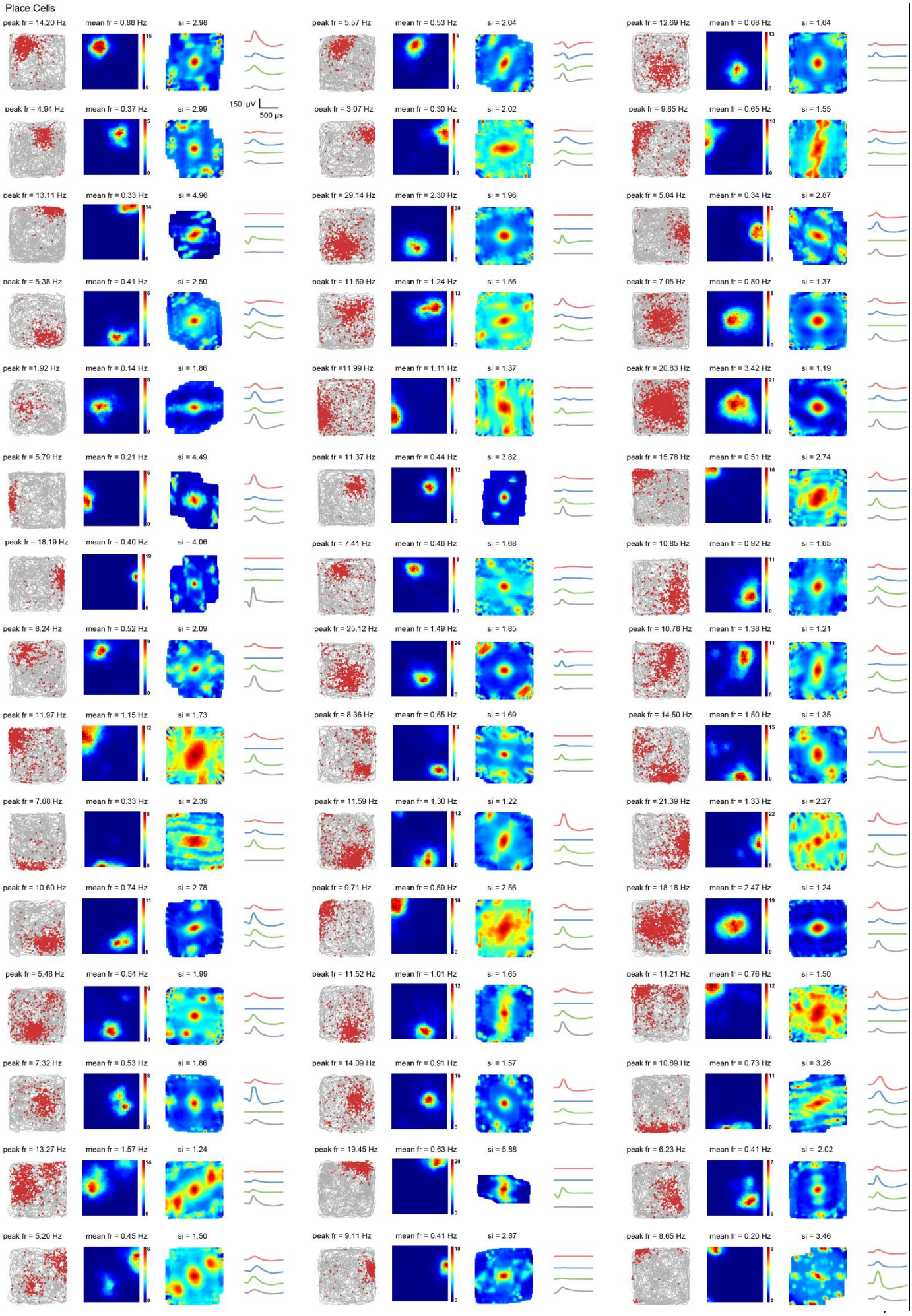

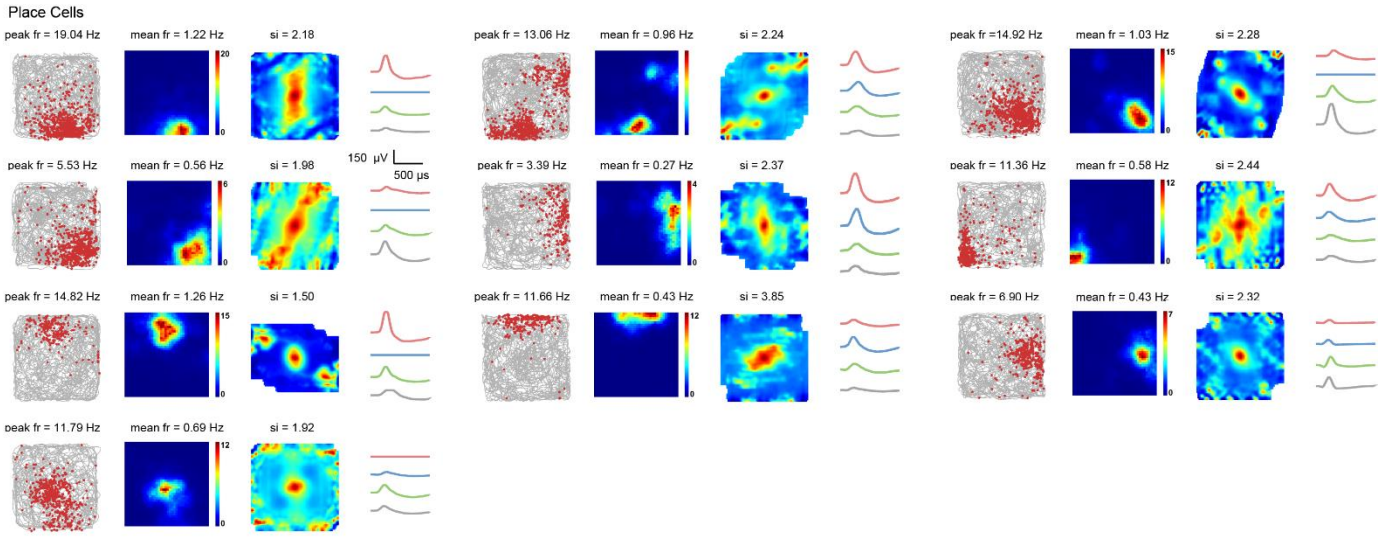

Fig. S7. Entire samples of V2 place cells. Trajectory (grey line) with superimposed spike locations (red dots) (first column); spatial firing rate maps (second column) and autocorrelation diagrams (third column). Firing rate was color-coded with dark blue (red) indicating minimal (maximal) firing rate. The scale of the autocorrelation maps was twice that of spatial firing rate maps. Peak firing rate, mean firing rate, and spatial information (SI) for each representative V2 place cell are labelled at the top of panels. Fourth column: Average spike waveforms on four electrodes of the same tetrode. Scale bar, 150 µV and 500 µs.

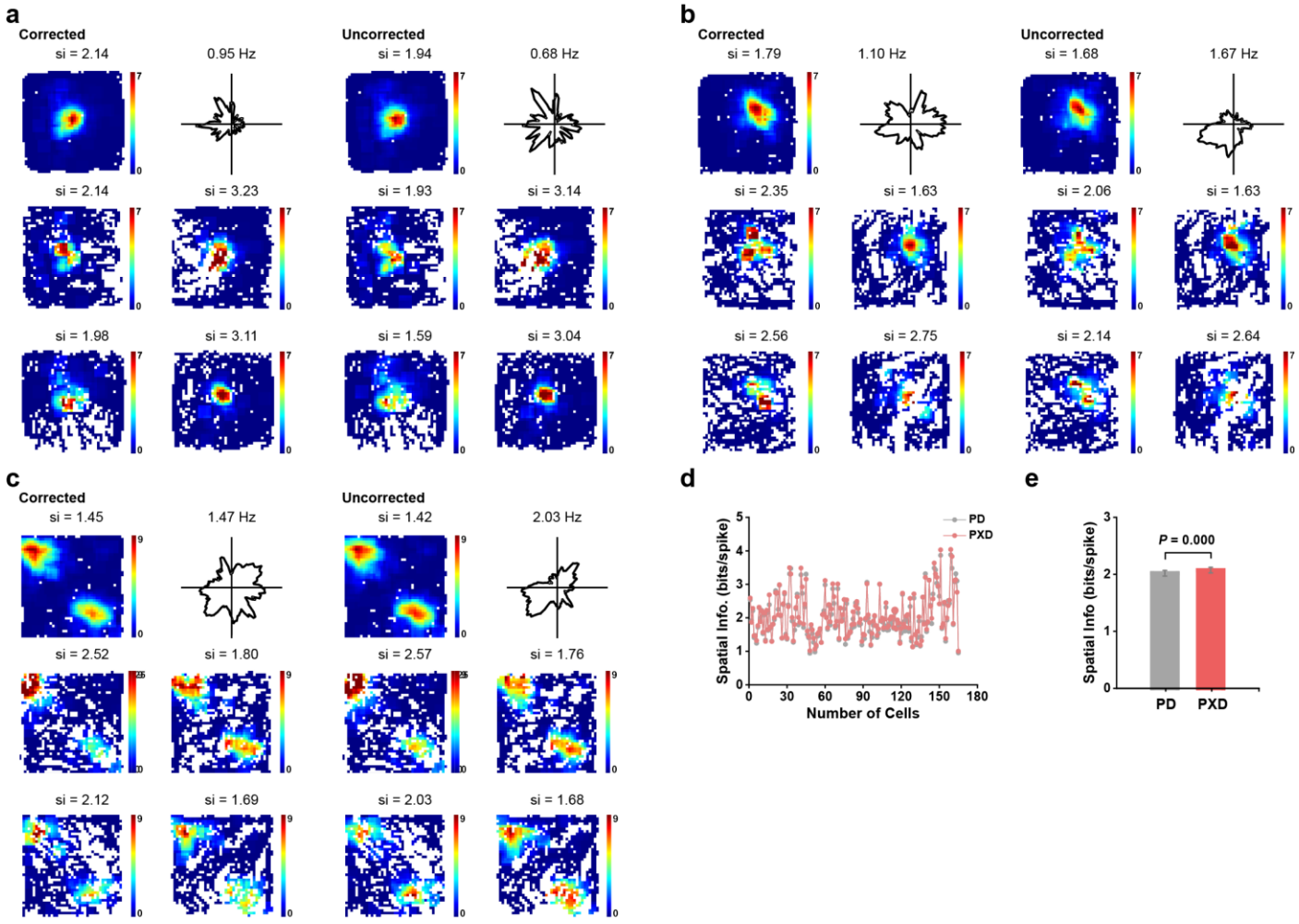

Fig. S8. Maximum likelihood estimation of the tuning property of V2 place cells. a-c, Tuning properties of representative V2 place cells in **Fig.1b** using maximum likelihood estimation. First two columns, corrected responses with maximum likelihood model; Last two columns, uncorrected responses. Top two panels show rate map and head direction tuning. Data from four head direction ranges (0°-90°, 90°-180°, 180°-270°, 270°-360°) are shown in the middle and bottom four panels. Note the similar spatial rate maps in four head direction ranges. **d**, Distribution of spatial information for all recorded V2 place cells (PD, uncorrected; PXD corrected). **e**, The increase in spatial information after using maximum likelihood estimation algorithm compared to the uncorrected spatial information (n = 165, two-tailed paired t-test, P = 0.000).

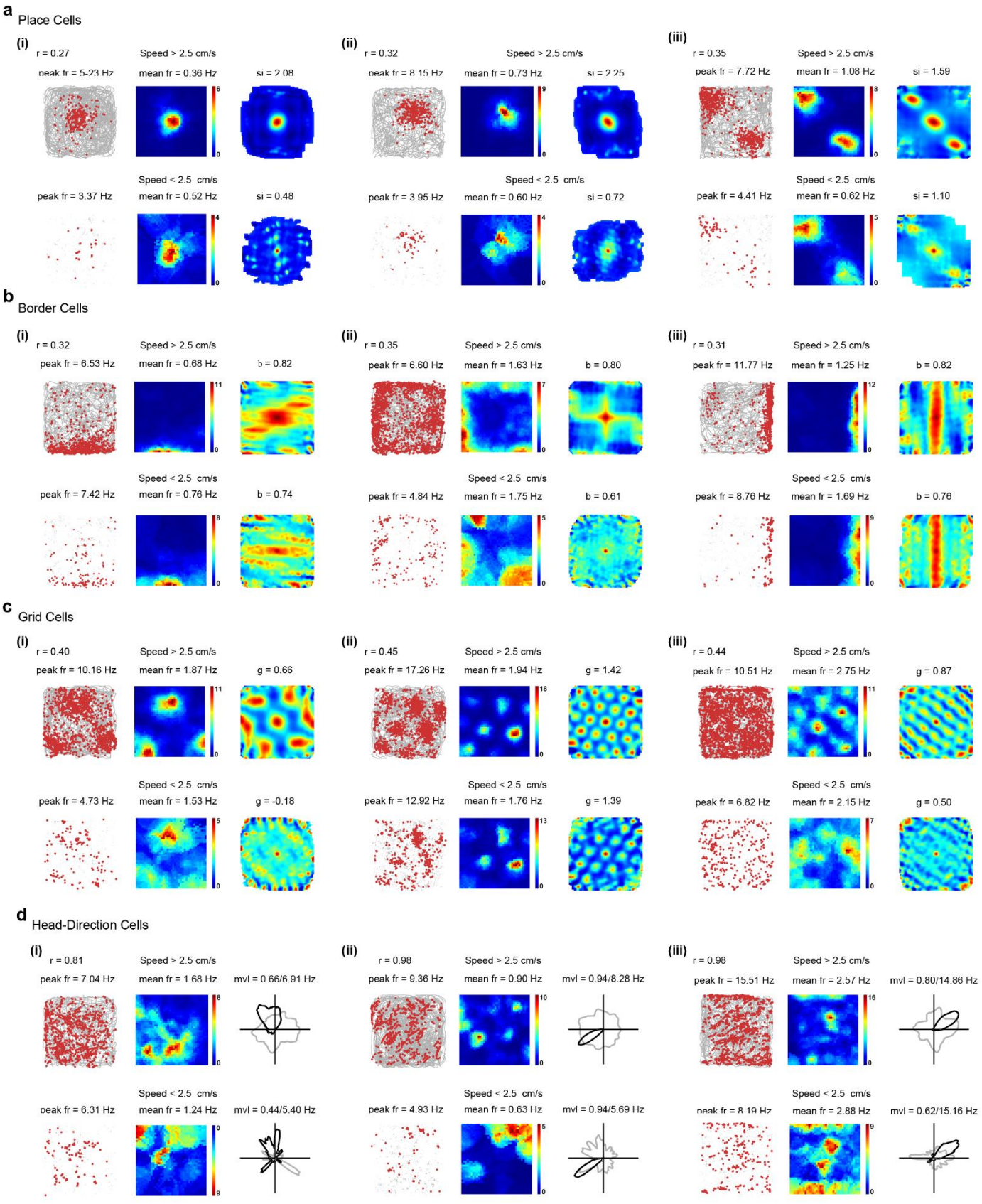

Fig. S9. Comparison of spatial responses of V2 spatially tuned cells between running and slow movement. a-d, Tuning properties of representative V2 place cells in **Fig. 1b**, V2 border cells in **Fig. 2a**, V2 grid cells in **Fig.3a** , and V2 head-direction cells in **Fig. 4a** during running (running speed > 2.5 cm/s) and slow running or immobility (running speed < 2.5 cm/s). Trajectory (grey line) with superimposed spike

locations (red dots) (left column); spatial firing rate maps (middle column) and autocorrelation diagrams (right column). Firing rate was color-coded with dark blue (red) indicating minimal (maximum) firing. The scale of the autocorrelation maps was twice that of spatial firing rate maps. Peak firing rate, mean firing rate, spatial information, border score or gridness score are shown. Third column: For head-direction cells, head direction tuning curves (black) plotted against dwell-time polar plot (grey), and the numbers represent the angular peak rates and mean vector length; for other cell types, autocorrelation maps were plot.

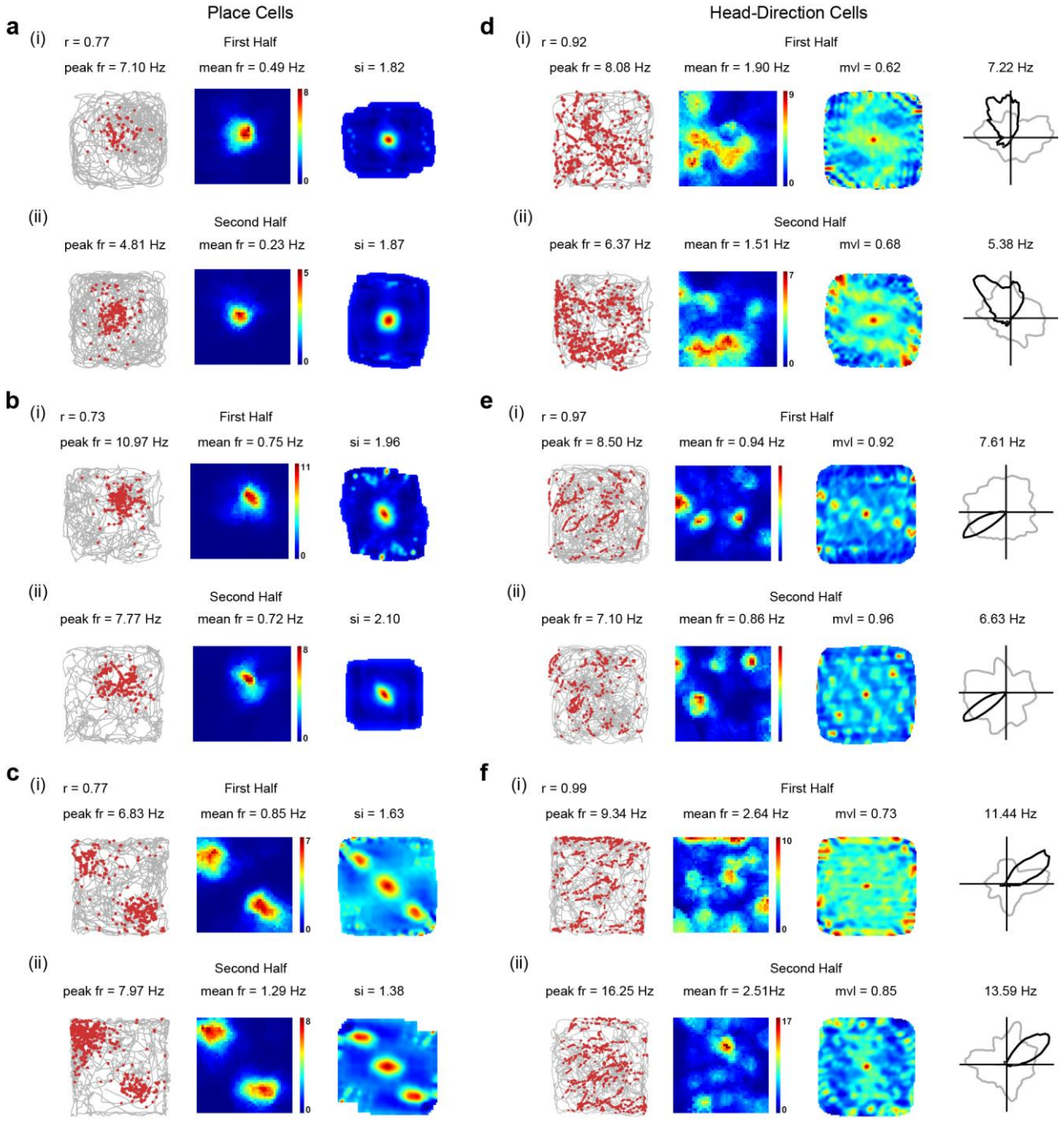

Fig. S10. Stable tuning of V2 place cells and V2 head-direction cells. a-c, Spatial responses of the three representative V2 place cells in **Fig. 1b** for the first half and second half of recording sessions. V2 place cells exhibit stable spatial firing patterns. Correlation coefficient (r) of spatial maps between the first half and second half of the recording session are shown for three V2 place cells. **d-f**, Spatial responses of the three representative V2 head-direction cells in **Fig. 4a** for the first half and second half of recording sessions. V2 head-direction cells exhibit stable preferred firing directions. Correlation coefficient of the angular map between the first half and second half of recording sessions are shown for three V2 head-direction cells.

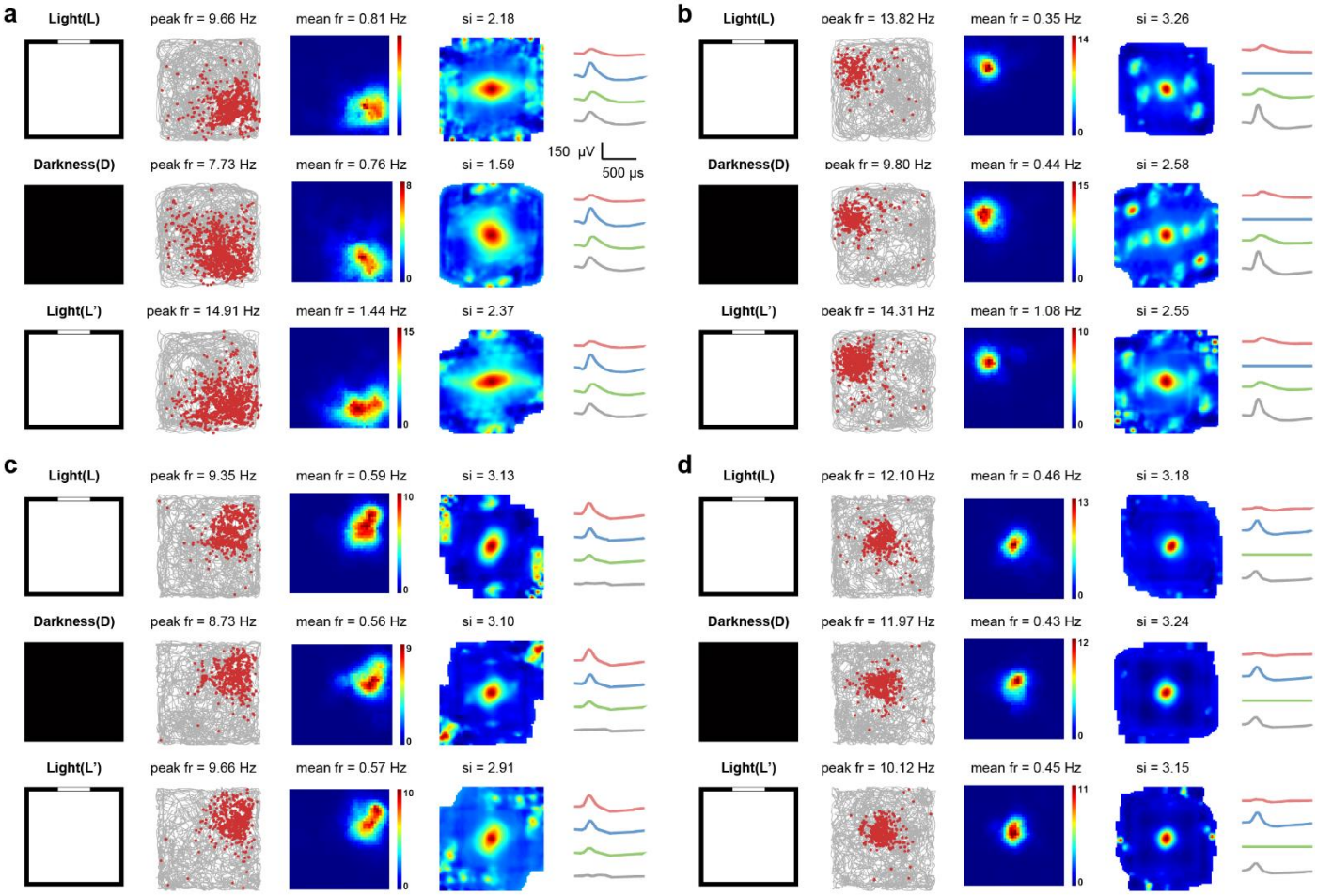

Supplementary Fig. S11. Preserved spatial selectivity of V2 place cells in the darkness. a-d, Responses of four representative V2 place cells in the darkness. Responses of V2 place cells in the L-D-L' conditions. Symbols and notations are similar as before.

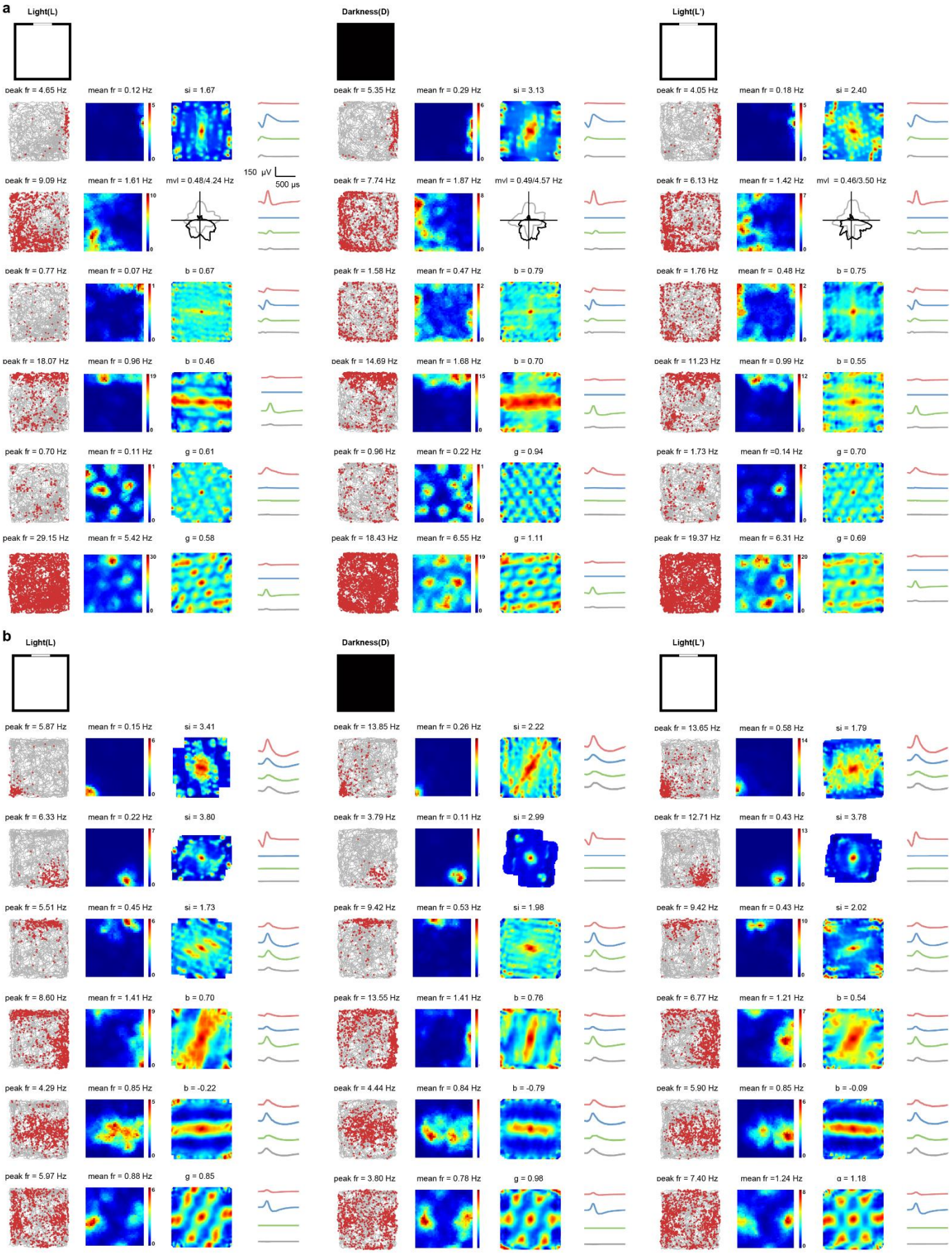

915

916 **Fig. S12. Persistence of spatial responses of simultaneously recorded multiple types of V2 spatially tuned**

cells in darkness. a, Spatial firing of six simultaneously recorded V2 units (from top to bottom: place cell, head-direction cell, border cell, border cell, grid cell and grid cell) in the L-D-L' conditions. Symbols and notations are similar as before. **b**, Same as **a** but for a different set of six simultaneously recorded V2 units (from top to bottom: place cell, place cell, place cell, border cell, band cell and grid cell).

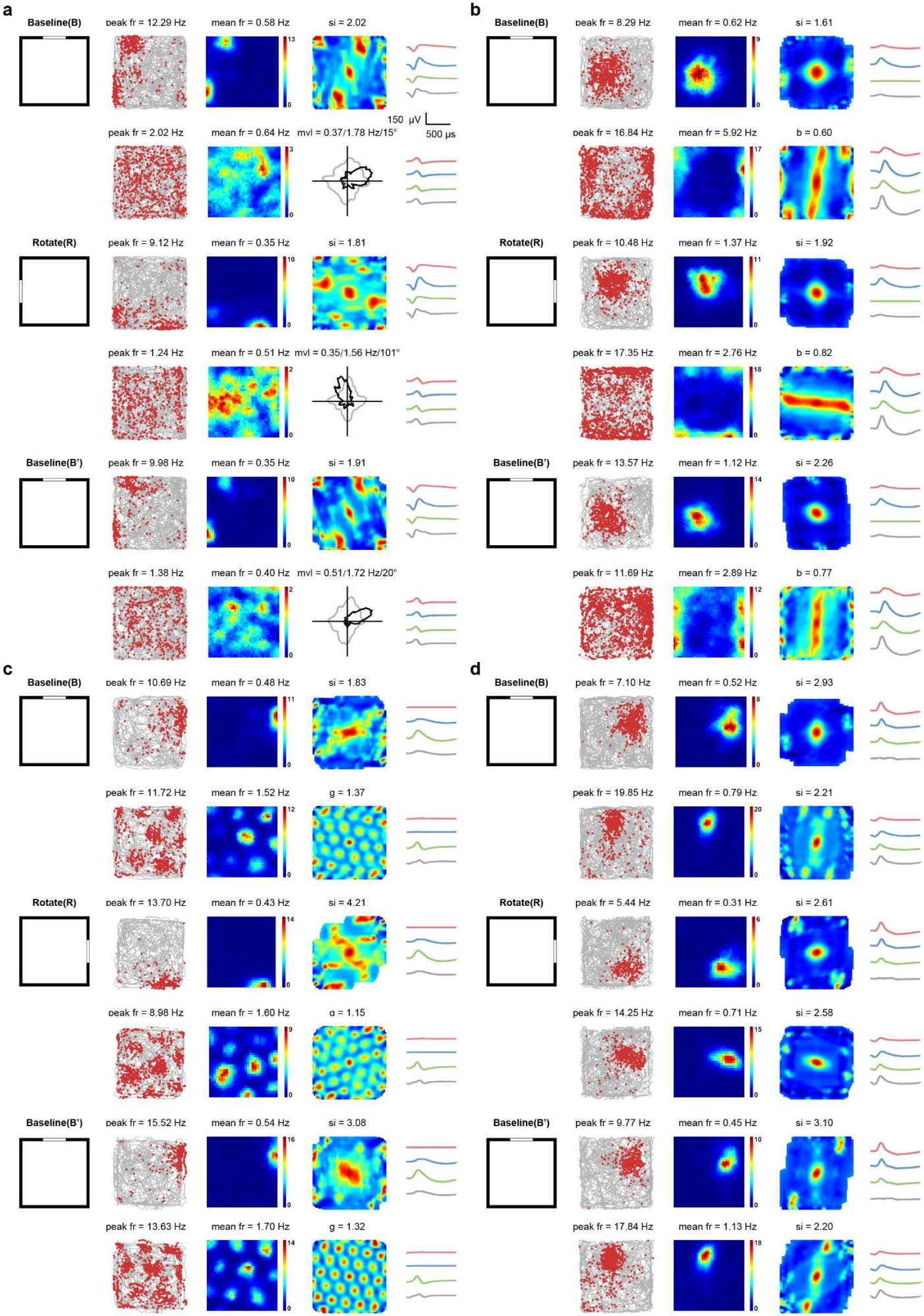

921

Fig. S13. Visual landmark control of V2 place cells and simultaneously recorded other spatially tuned cells. a, One V2 place cell with one simultaneously recorded V2 head-direction cell in response to visual landmark manipulation. **b**, One V2 place cell with one simultaneously recorded V2 border cell in response to visual landmark rotation. **c**, One V2 place cell with one simultaneously recorded V2 grid cell in response to visual cue manipulation. **d**, Two simultaneously recorded V2 place cells in response to visual landmark manipulation. Top to bottom panels: responses of V2 place cells and simultaneously recorded other V2 spatially tuned cells in baseline, clockwise or counterclockwise 90° degree rotation of visual cue and back to baseline. Symbols and notations are similar as before.

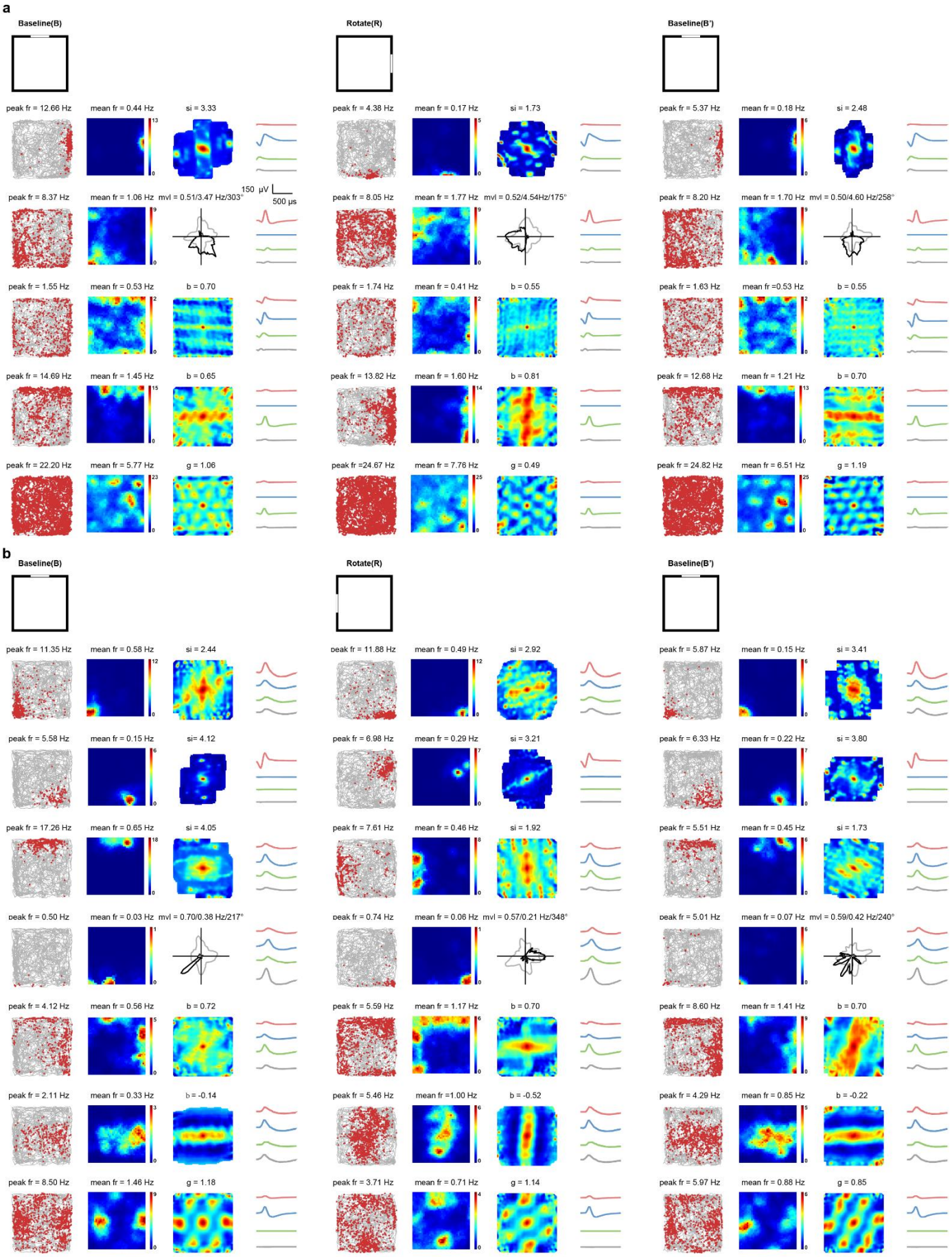

Fig. S14. Visual landmark control of simultaneously recorded multiple types of V2 spatially tuned cells. **a**, Spatial firing of five simultaneously recorded V2 units (from top to bottom: place cell, head-direction cell, border cell, border cell and grid cell) in response to clockwise 90° visual cue rotation. Symbols and notations are similar as before. **b**, Spatial firing of seven simultaneously recorded V2 units in another independent recording session (from top to bottom: place cell, place cell, place cell, head-direction cell, border cell, band cell and grid cell) in response to counterclockwise 90° visual cue rotation.

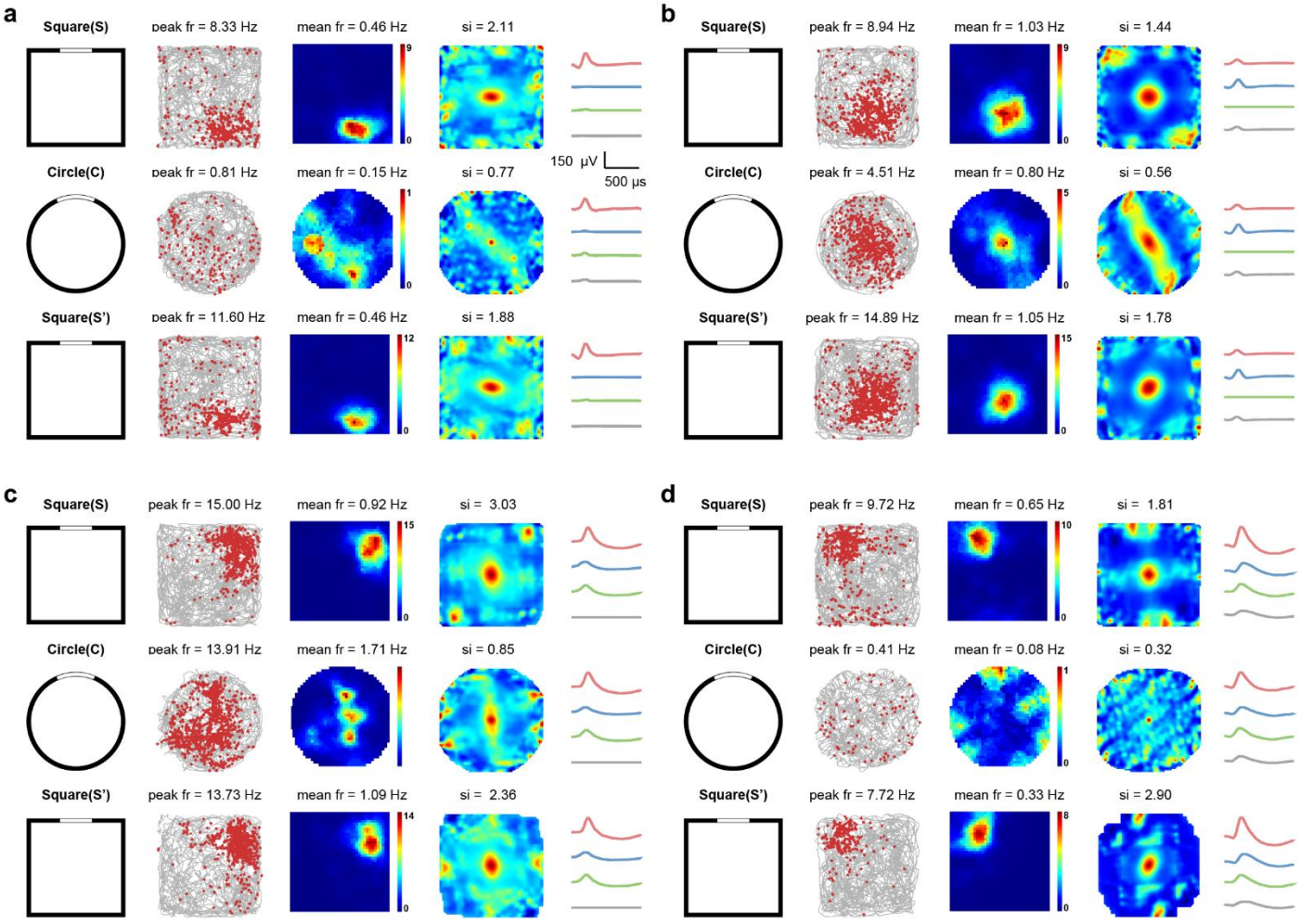

Supplementary Fig. S15. Remapping of V2 place cells in different geometric environments. a-d, Spatial responses of four representative V2 place cells showed remapping in response to different environmental shapes. Upper to bottom panels, responses of the place cells in the square enclosure (upper panel), circle (middle panel) and back to the square enclosure (lower panel). Symbols and notations are similar as before.

Border Cells

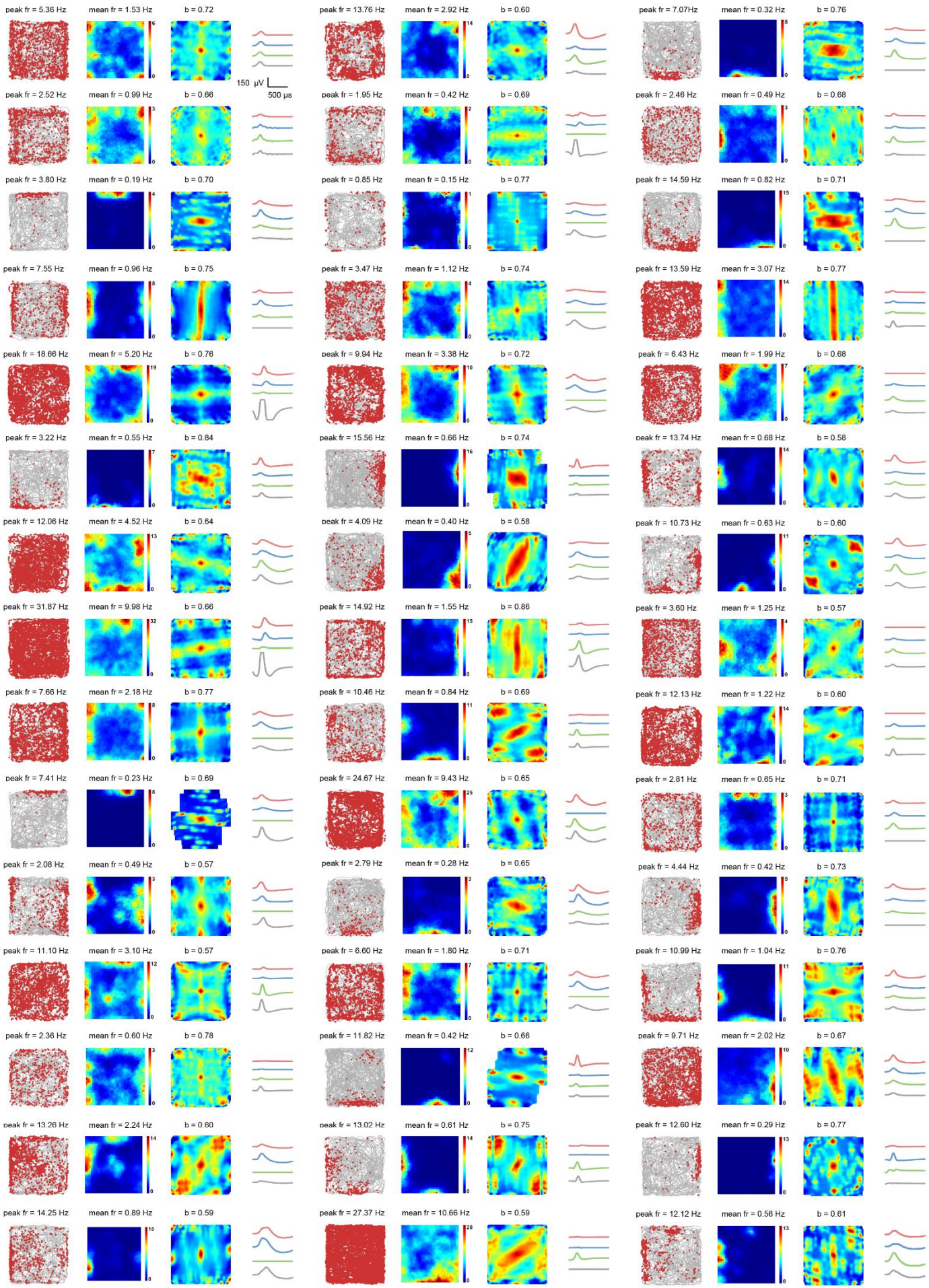

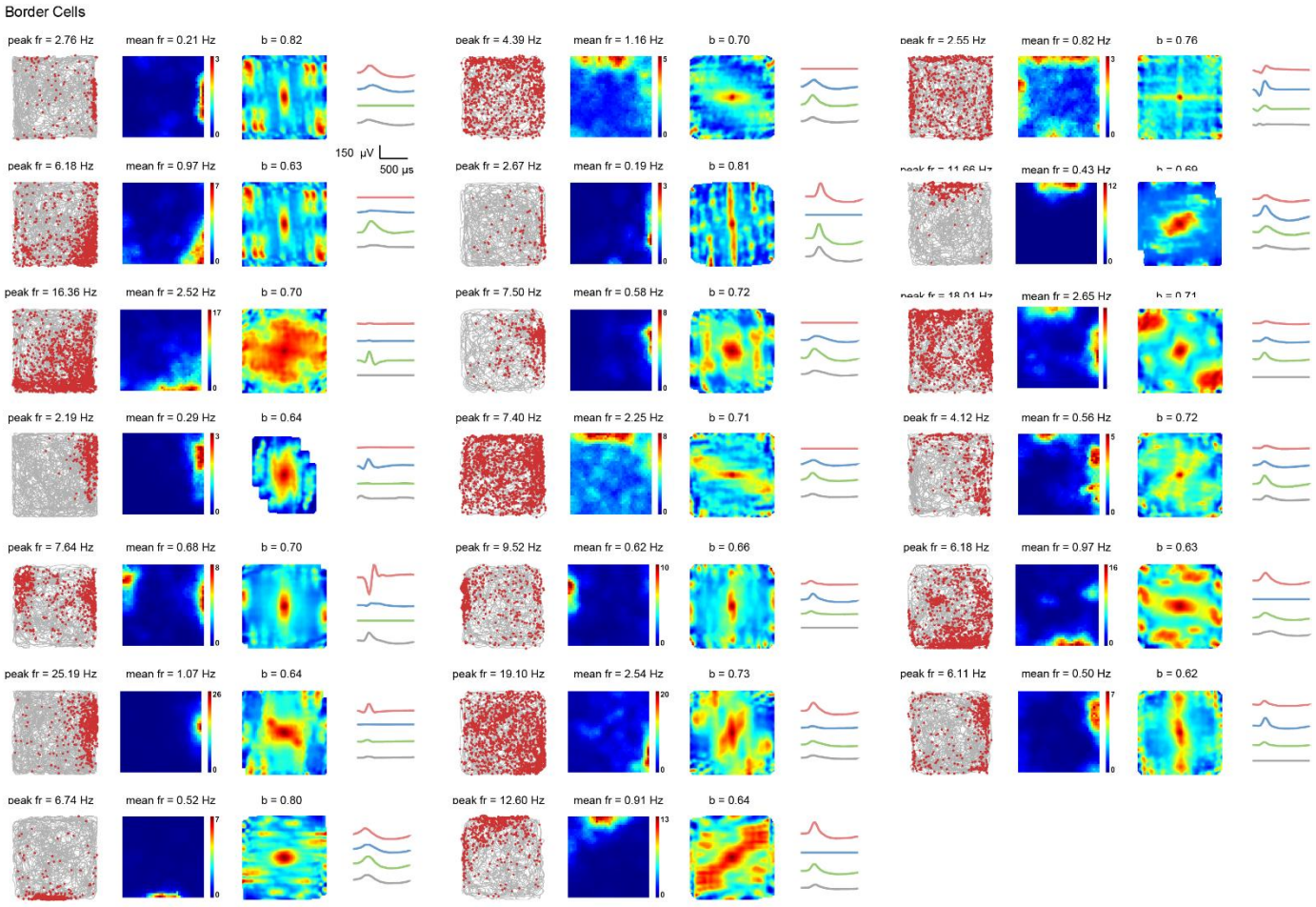

943

944 **Fig. S16. Entire samples of V2 border cells.** Trajectory (grey line) with superimposed spike locations (red
945 dots) (first column); spatial firing rate maps (second column) and autocorrelation diagrams (third column).
946 Firing rate was color-coded with dark blue (red) indicating minimal (maximum) firing rate. The scale of the
947 autocorrelation maps was twice that of the spatial firing rate maps. Symbols and notations are similar as before.

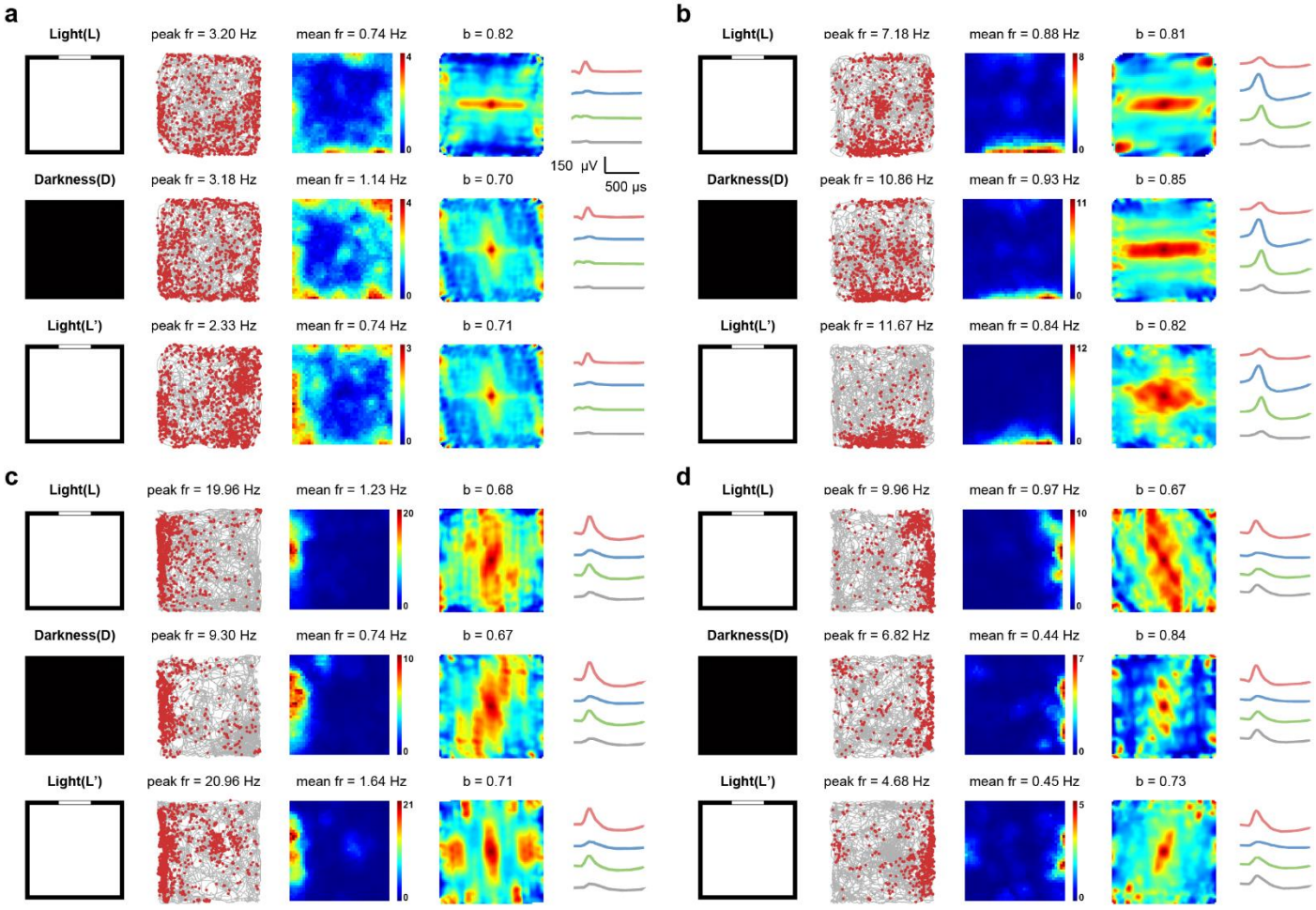

Fig. S17. V2 border cells preserved spatial firing patterns in the darkness. a-d, Responses of representative V2 border cells in the darkness. Symbols and notations are similar as before.

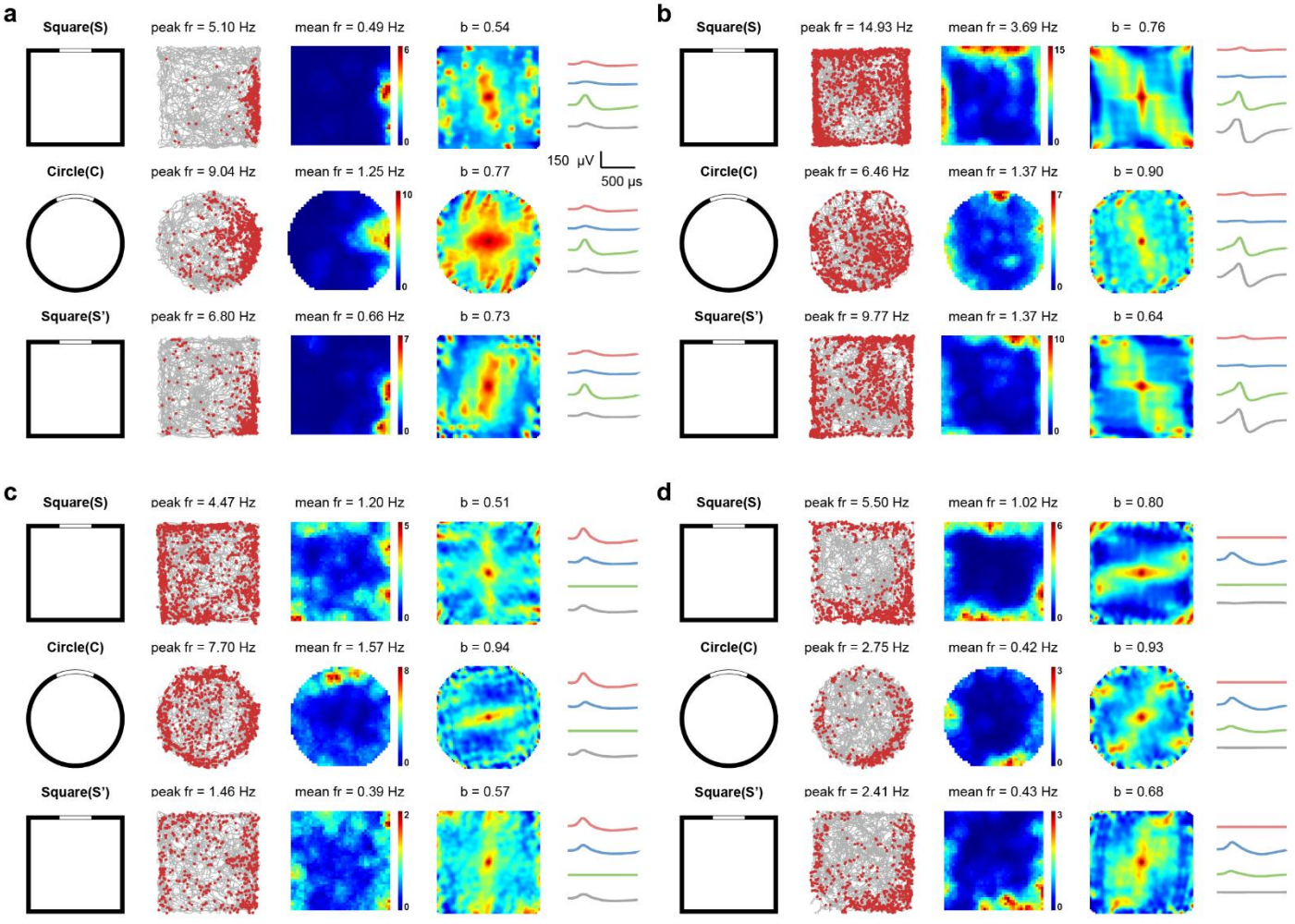

Fig. S18. Preserved spatial selectivity of V2 border cells in different shapes of environments. a-d, Responses of four representative V2 border cells in navigation environments with different shapes. Symbols and notations are similar as before.

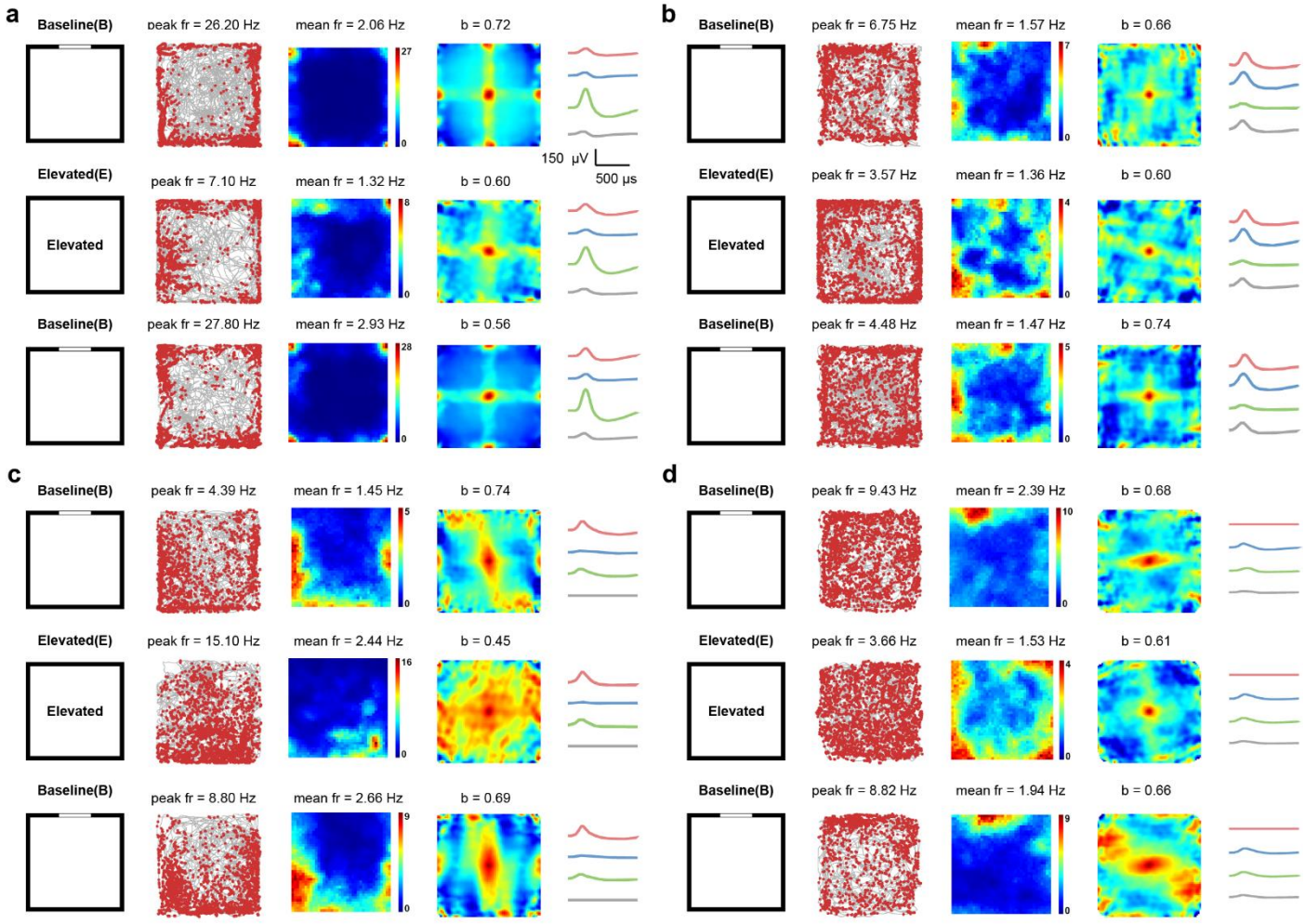

Fig. S19. Spatial responses of V2 border cells in the elevated platform without walls. a-d, Responses of representative V2 border cells in the elevated platform without walls. First column: schematic of experimental paradigms. Symbols and notations are similar as before.

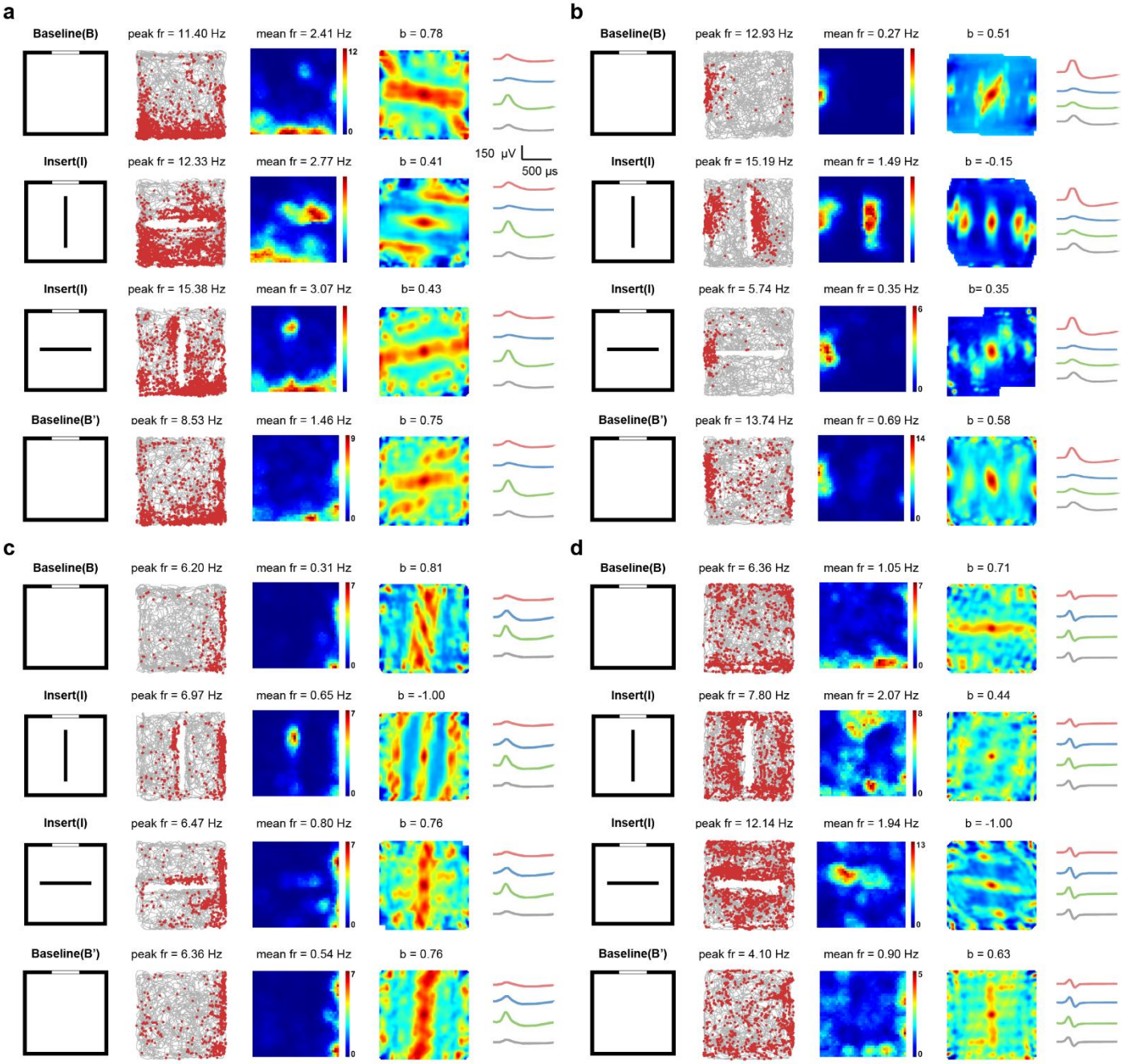

Fig. S20. Spatial responses of V2 border cells to newly inserted walls. a-d, Responses of four representative V2 border cells to the external insert. Left column: Schematic of experimental paradigms. Symbols and notations are similar as before.

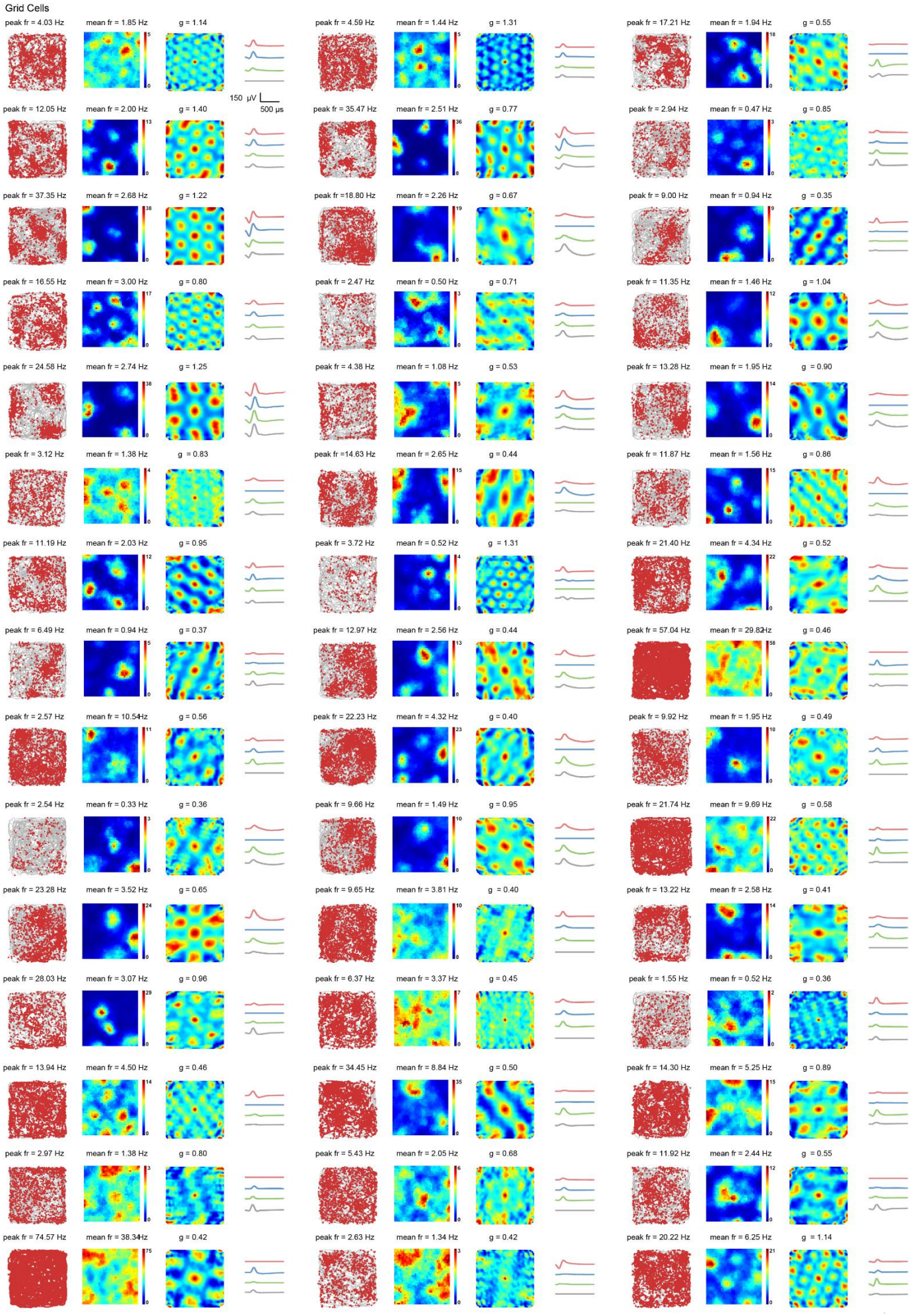

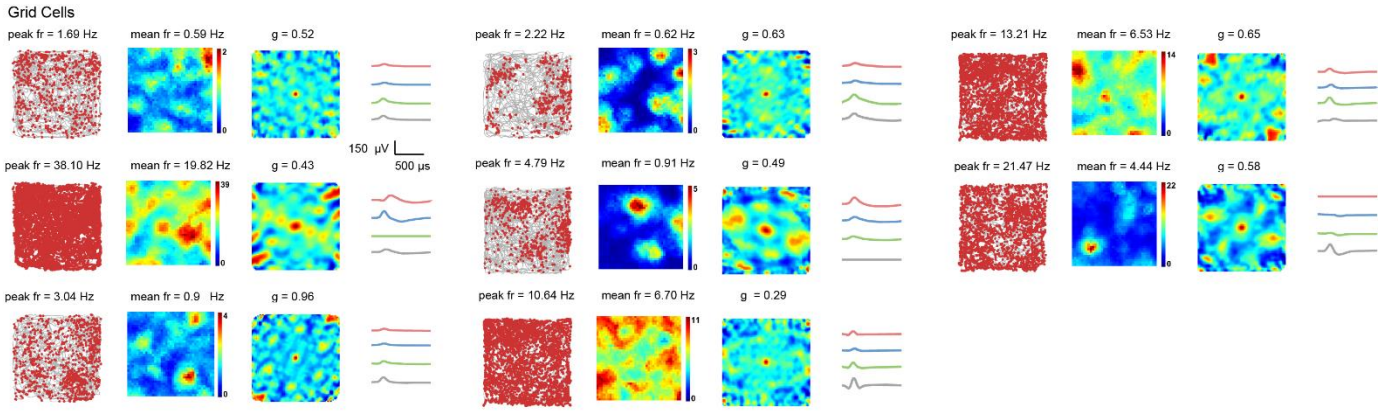

964

965 **Fig. S21. All identified samples of V2 grid cells.** Symbols and notations are similar as before.

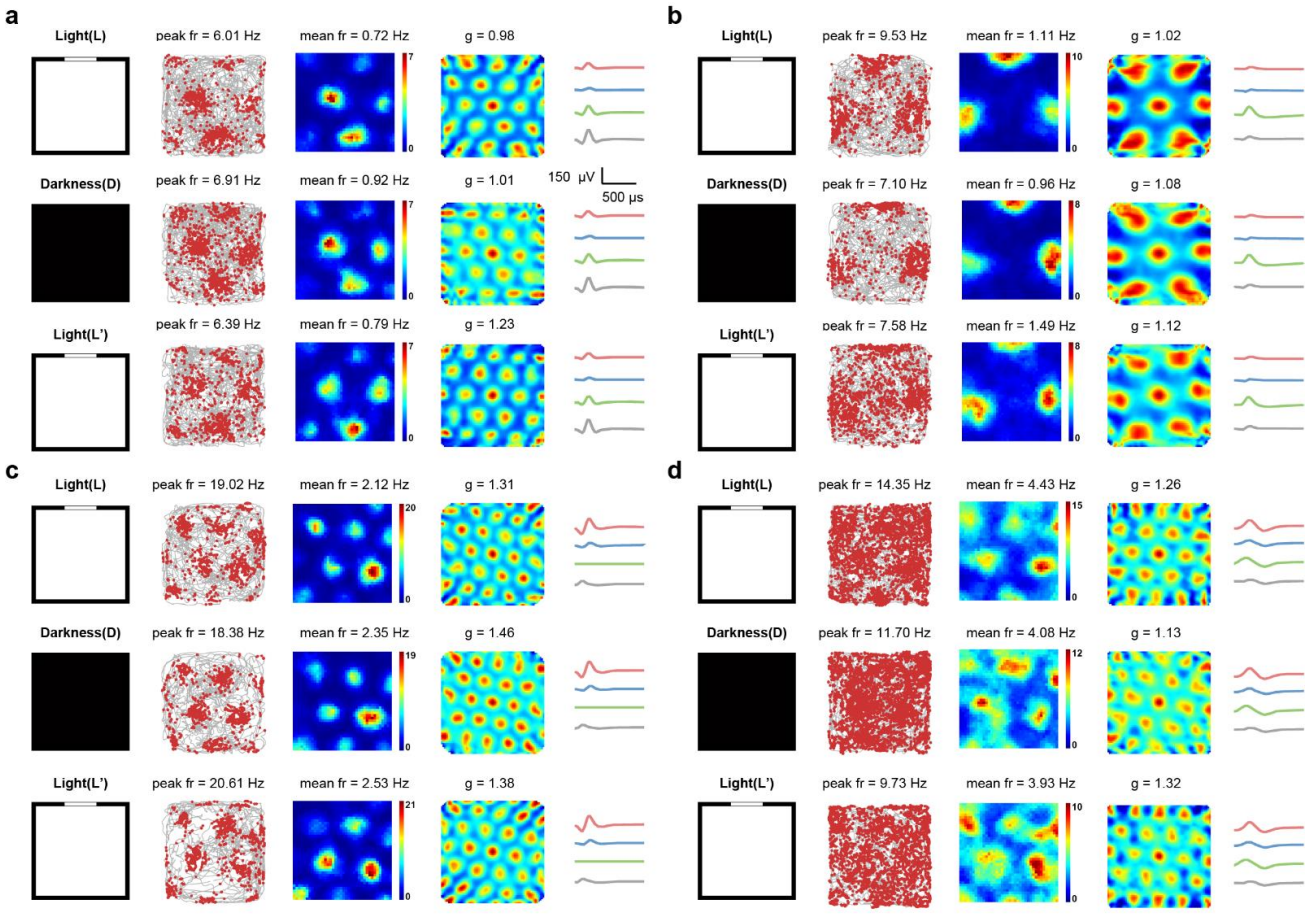

Fig. S22. Stable hexagonal spatial firing patterns of V2 grid cells in the darkness. a-d, Responses of four representative V2 grid cells in the darkness. Schematic of the L-D-L' experimental paradigm. Symbols and notations are similar as before.

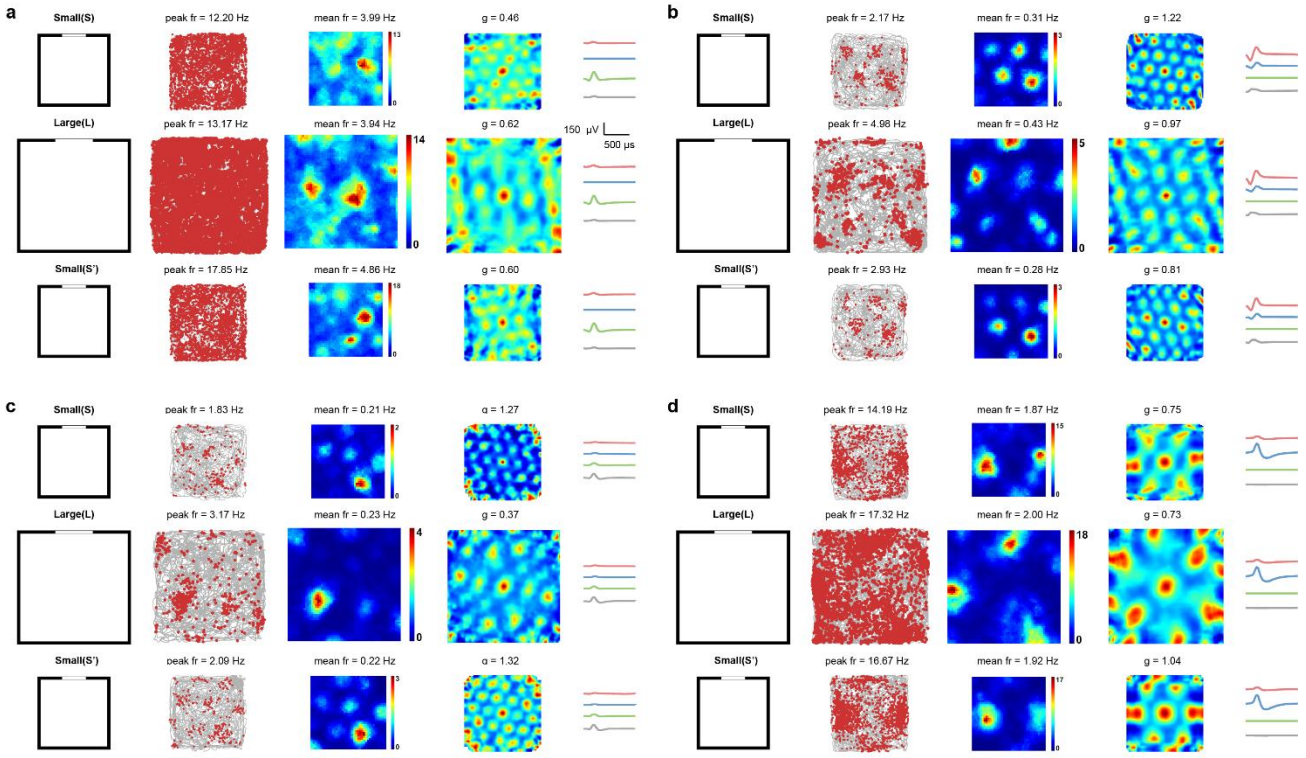

Fig. S23. Persistence of grid firing patterns of V2 gird cells in larger environments. a-d, Responses of representative V2 grid cells in running environments with different sizes. Left column: schematic of experimental paradigms during switch of environment: 1×1 m^2 (S), 1.5×1.5 m^2 (L) and 1×1 m^2 (S'). Symbols and notations are similar as before.

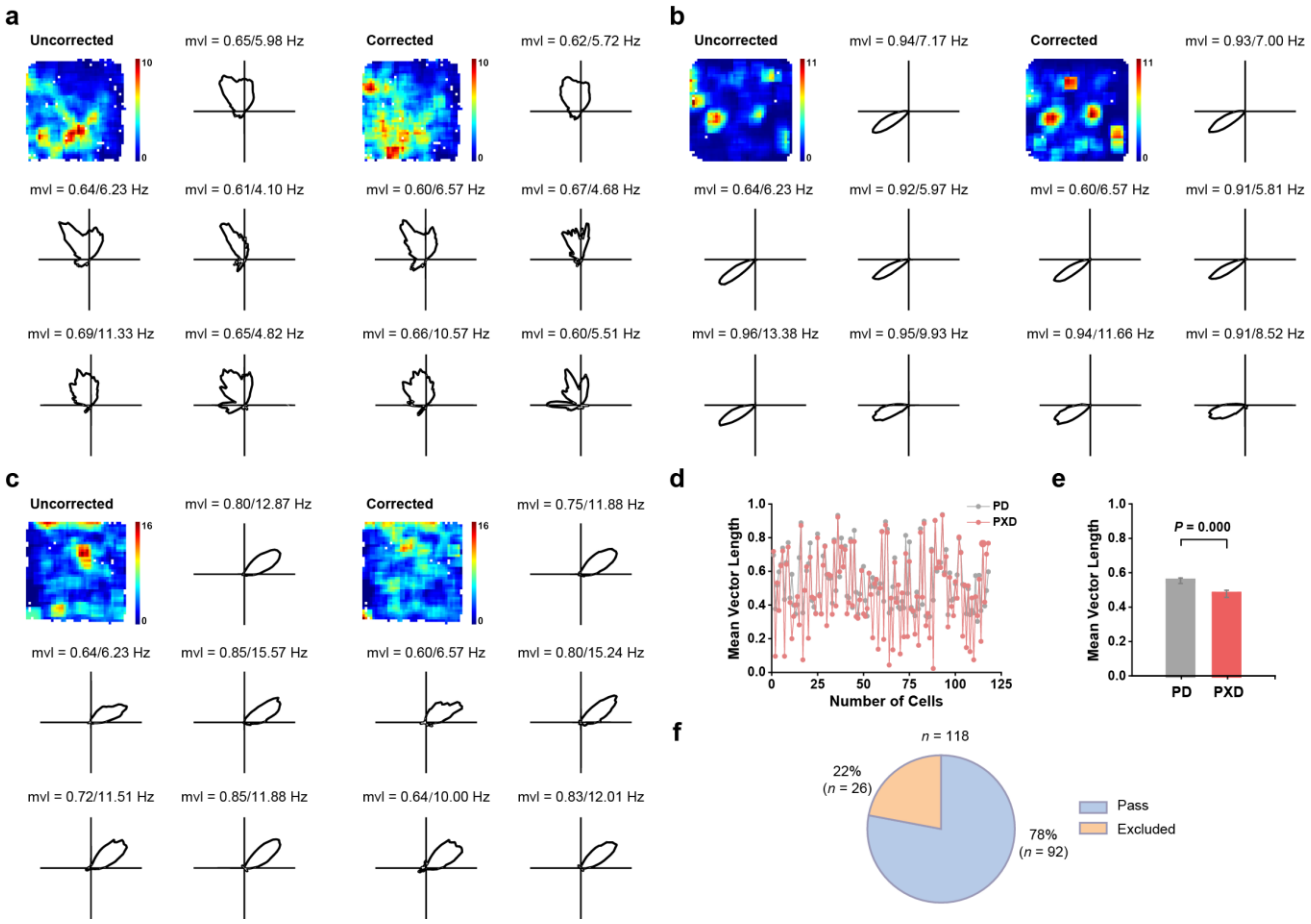

Fig. S24. Maximum likelihood estimation of the tuning property of V2 head-direction cells. a-c, Tuning properties of representative V2 head-direction cells in **Fig. 4a** using maximum likelihood correction. First two columns: corrected responses; last two columns: uncorrected responses. Top row shows the rate map and head direction tuning. Bottom two rows show the data from the four quadrant. Note that the preferred directions were similar in the four quadrants of the environment. **d**, Distribution of mean vector length for all identified V2 head-direction cells that passed the threshold criterion (PD, uncorrected; PXD corrected). **e**, Mean vector length after maximum likelihood estimation was significantly reduced compared to the uncorrected mean vector length (n = 116, two-tailed paired t-test, P = 0.000). **f**, Venn diagram showing the proportion of V2 head-direction cells passing (92 out of 118, 78%) or excluded (26 out of 118, 22%) by the maximum likelihood estimation algorithm.

a

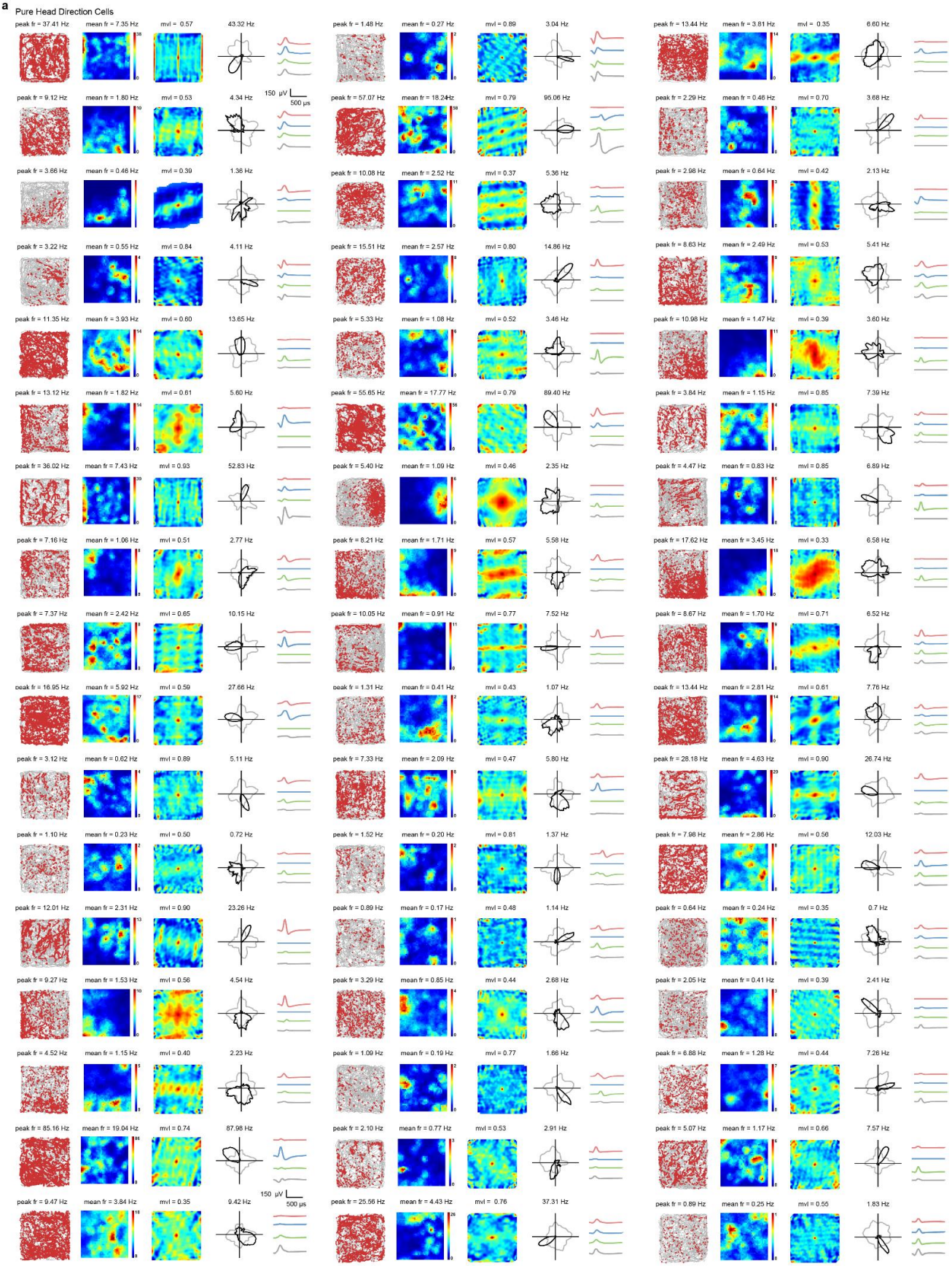

986

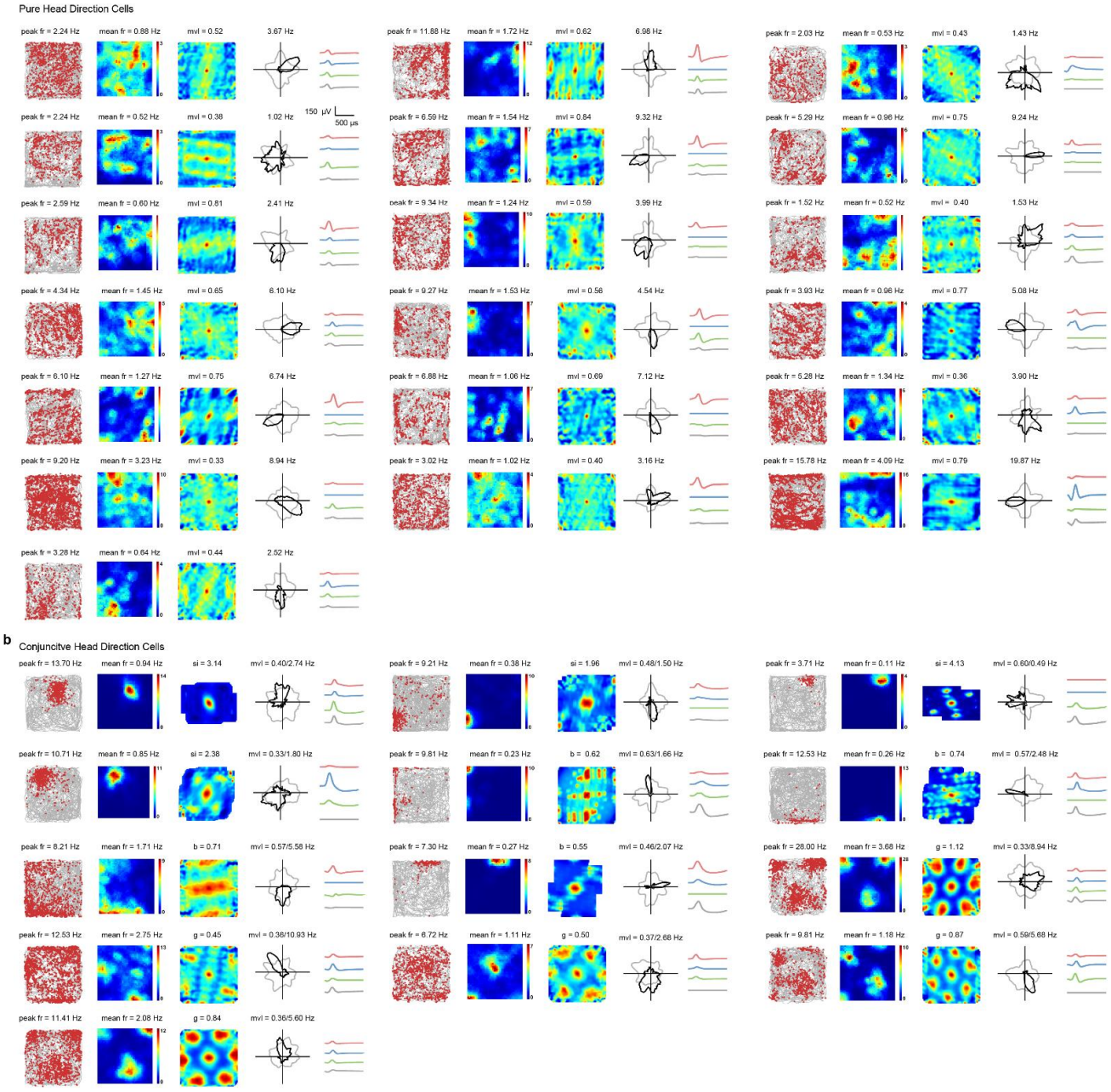

Fig. S25. All identified pure V2 head-direction cells and conjunctive V2 head-direction cells. a, Pure V2 head-directions cells. **b**, Conjunctive V2 head-direction cells. Symbols and notations are similar as before.

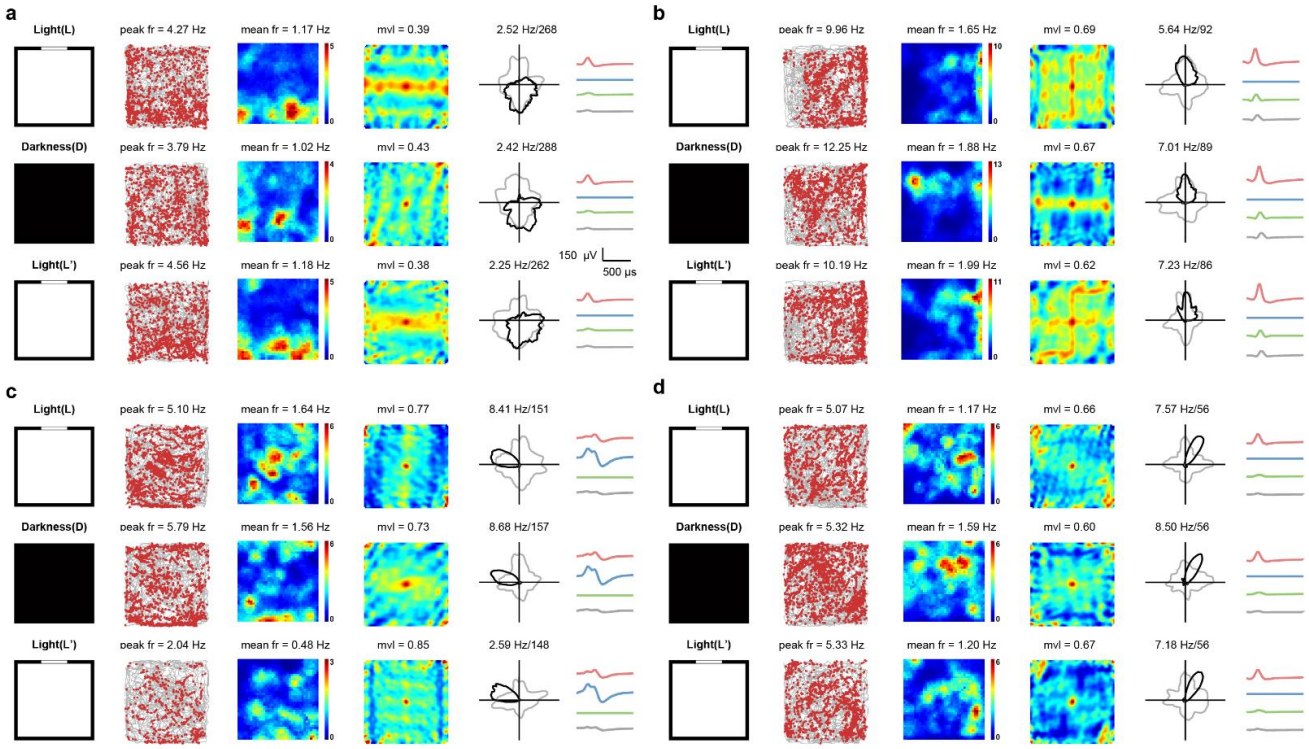

991

992 **Fig. S26. Stable spatial tuning properties of V2 head-direction cells in the darkness. a-d**,
993 Responses of four representative V2 head-direction cells in the L-D-L' conditions. Symbols and
994 notations are similar as before.

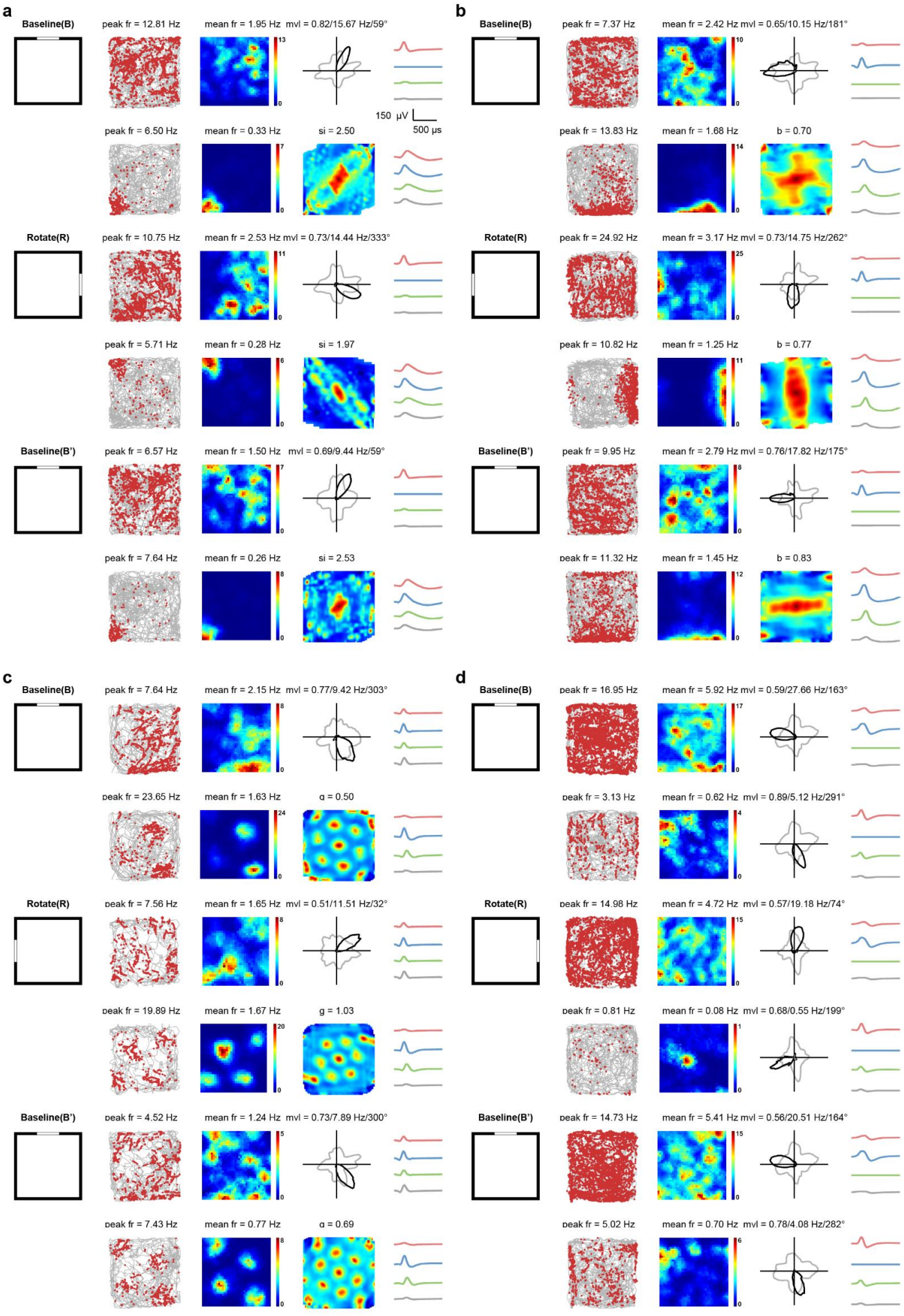

Fig. S27. Visual cue control of V2 head-direction cells together with simultaneously recorded other spatial cells. a, One V2 head-direction cell with one simultaneously recorded V2 place cell in response to visual landmark manipulation. **b**, One V2 head-direction cell with one simultaneously V2 border cell in response to visual cue rotation. **c**, One V2 head-direction cell with one simultaneously recorded V2 grid cell in response to visual landmark manipulation. **d**, Two simultaneously recorded V2 head-direction cells in response to visual landmark rotation. Symbols and notations are similar as before.

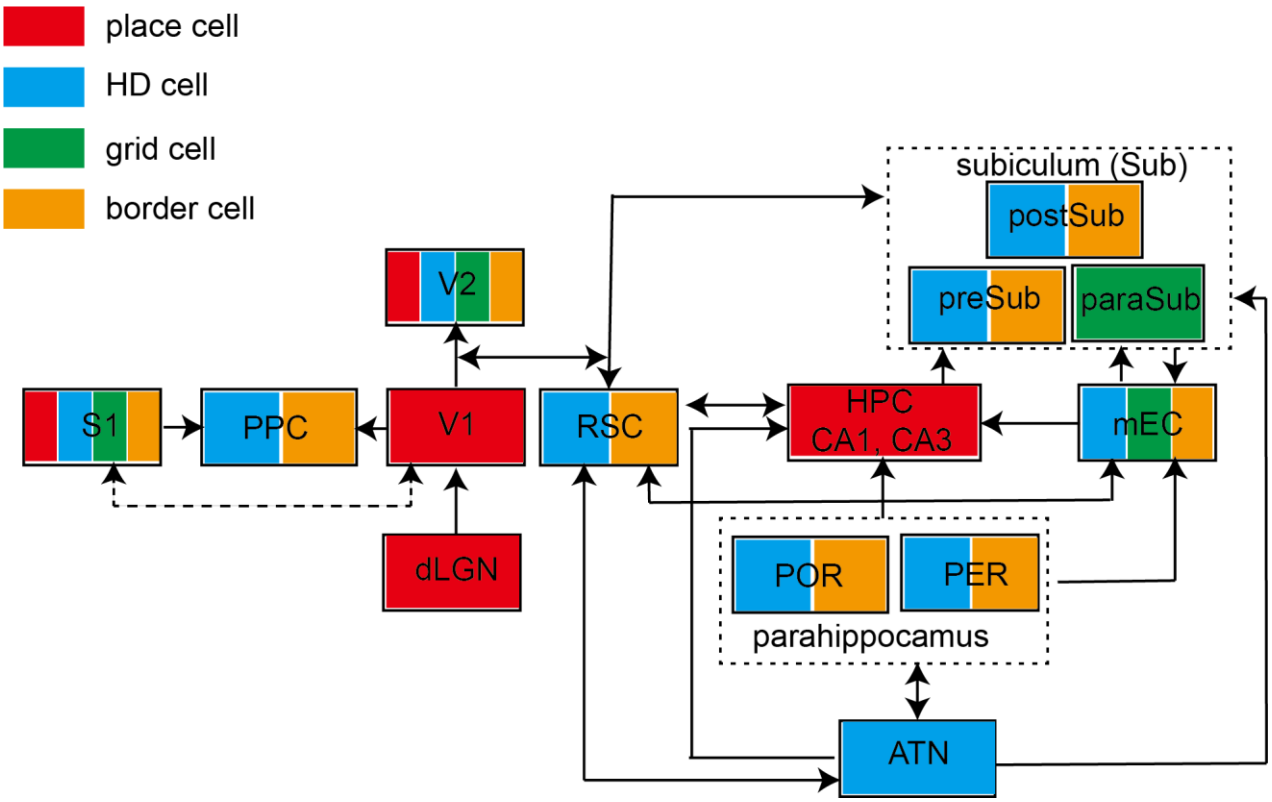

Fig. S28. Schematic of identified brain structures with four major types of spatial tunings. Abbreviations: ATN (anterior thalamic nuclei), S1 (primary somatosensory cortex), PPC (posterior parietal cortex), V1 (primary visual cortex), V2 (secondary visual cortex), RSC (retrosplenial cortex), HPC (hippocampus), mEC (medial entorhinal cortex), POR (postrhinal cortex), PER (perirhinal cortex), preSub (presubciculum), paraSub (parasubiculum), postSub (postsubiculum). Arrow indicates the connectivity.